QUANTUM CONTROL OF DONOR SPINS IN SILICON AND THEIR ENVIRONMENT



Gary Wolfowicz

ST EDMUND HALL

A THESIS SUBMITTED FOR THE DEGREE OF DOCTOR OF PHILOSOPHY

AT THE UNIVERSITY OF OXFORD

TRINITY TERM 2015

QUANTUM CONTROL OF DONOR SPINS IN SILICON AND THEIR ENVIRONMENT

Gary Wolfowicz

St Edmund Hall

Trinity Term 2015

AN ABSTRACT SUBMITTED FOR THE DEGREE OF DOCTOR OF PHILOSOPHY

Donors in silicon, which combine an electron and nuclear spin, are some of the most promising candidates for quantum information. The electron spin has been proposed as a register with fast manipulation and the nuclear spin as a memory with long coherence times. However, this division reduces the complexity of the donor system, in particular behaviors emerging from their interaction. In natural silicon, there is also the presence of ^{29}Si nuclear spins in the donor environment; though they are generally seen as a source of decoherence, they are quantum systems that can be investigated too. The main subject of this thesis is the study of the interactions between these various spins, using different methods to probe and control them.

I first concentrate on the coupling between the donor and the ^{29}Si spins. This coupling can be perturbed by the application of dynamical decoupling on the donor electron spin, whose evolution can be made sensitive to the number of ^{29}Si spins interacting together. I then propose an error correction scheme using the donor and ^{29}Si spins, showing key requirements such as coherence times and methods for manipulation and initialization. Secondly, I focus on the donor itself, in a regime where the hyperfine and Zeeman couplings compete with each other. Here, the spin transitions can have different sensitivities to the magnetic environment, and can even be suppressed to first order, resulting in coherence times up to seconds with electron spin-like manipulation times. Controlling this sensitivity was also used to probe the effect of the donor on the ^{29}Si spin bath evolution. Finally, I use electric fields to modulate the hyperfine coupling within the donor. I first characterize the spins' sensitivity to the electric field, and then demonstrate electrical switching of the nuclear spin response to an external magnetic excitation.

Acknowledgments

Before starting this PhD, I was quite worried by how long three and a half years was going to be, but such time seems ridiculously short right now. Yet, these years were certainly filled with their ups and downs, life changes and an overall gain of maturity with respect to the science and the research environment. Without a doubt, to reach this point today, to have been able to complete these past years and the many works presented here, none of it would have been possible without all the people that taught and supported me, and generally with whom ideas -some crazy (or "brave" as the British would say), some boring but some good too- were exchanged.

Obviously, this starts with my supervisors, John Morton and Simon Benjamin, without whom none of it would have been possible. Especially John, sincerely thanks for everything; from the very first few weeks learning ESR in CAESR to all the many discussions we had. I don't think I could have had as much freedom to do what I wanted in many other groups, to be able to travel so often to conferences and meet people, and finally to have realized so many projects. I'd like to thanks Roberto Lo Nardo too with whom we shared this three past years as PhD students, especially for making this PhD not just about work but about having some fun too. I am also very grateful to Stephanie Simmons, my "sempai" in Japanese, for showing me the ropes, and for all our world domination discussions (as well as board game nights!). And thanks to all the other people in the group, from the old Oxford crowd (Vasileia Filidou, Richard George and Hannes Maier-Flag) and to the UCL people (Cheuk Chi Lo -our device Guru-, Matias Urdampilleta -without whom I'd probably have forgotten French already-, Jarryd Pla, Naitik Panjwani, Salahuddin Nur, Anasua Chatterjee, Philipp Ross, John Mansir (there's no particular order here!)). I have to thank all my collaborators too, in particular Seto Balian, my theoretical counterpart, and his supervisor Tania Monteiro (even considering our very heated discussions), as well as Steve Lyon and Alexei Tyryshkin at Princeton who were so kind to host me few times this past years and without whom a lot of this work wouldn't have been possible. Thanks also to Philippe Goldner, Renbao Liu and Wenlong Ma for our work together. I'm also

very very grateful to Mike Thewalt and all the ^{28}Si people (Helge Riemann, Nikolai Abrosimov, Peter Becker, Hans-Joachim Pohl) who made all the samples in this work.

Contents

1 Introduction **11**

1.1 Quantum information processing 11

1.2 Control of quantum systems 12

1.3 Challenges for donor spins in silicon 14

1.3.1 The Kane architecture 14

1.3.2 Donor interaction with the spin environment 16

1.3.3 Donor interaction with the electric environment 18

2 Quantum information and spin resonance **21**

2.1 Quantum information 21

2.1.1 Quantum states and their evolution 21

2.1.2 Relaxation, polarization and decoherence 27

2.2 Magnetic resonance 29

2.2.1 Theory of magnetic resonance 30

2.2.2 ESR measurements and experimental apparatus 32

2.2.3 Typical ESR experiments 35

2.2.4 Typical ENDOR experiments 38

3 Donors in silicon **43**

3.1 Donor spin system 43

3.1.1 Donor spin Hamiltonian 43

3.1.2 Transition properties 46

3.2 Spin relaxation and decoherence 49

3.2.1 Electron spin relaxation times T_{1e} 51

3.2.2 Electron spin coherence times T_{2e} 54

3.2.3 Nuclear spin coherence times T_{2n} 59

3.2.4 Outlook 60

4 Central spin - bath dynamics **61**

4.1 ^{29}Si bath dynamics 62

4.1.1 ^{29}Si ENDOR spectrum for ^{31}P-donors 62

4.1.2 Bath modeling: pseudo-spin picture 64

4.1.3 Bath modeling: Cluster Correlation Expansion (CCE) 69

4.2 Electron spin decoherence in ^{nat}Si:^{31}P 70

4.2.1 Dynamical decoupling (DD) 70

4.2.2 Time symmetry in DD and many-body correlations 74

4.3 Nuclear spin registers in ^{nat}Si 79

4.3.1 Proposal for quantum error correction (QEC) 80

4.3.2 ^{31}P and ^{29}Si nuclear spin coherence 86

4.4 Conclusion 90

5 Magnetic sensitivity of donor spins **93**

5.1 Electron - electron spin interactions at the CTs 95

5.1.1 ^{209}Bi donor electron spin coherence at X-band: the low spin-mixing regime 95

5.1.2 ^{209}Bi donor electron spin coherence at the clock transitions 98
5.2 Donor electron - ^{29}Si bath interactions near CTs 106
5.2.1 Mixing effect on bath dynamics 106
5.2.2 Experiments: model test 110
5.3 Conclusion 112

6 Manipulating the hyperfine interaction via the Stark shift 115
6.1 Background 116
6.1.1 A scalable architecture for donors in silicon 116
6.1.2 Stark shift theory 118
6.2 Electrically-induced hyperfine control and conditional gates 121
6.2.1 Stark shift characterization 121
6.2.2 Conditional spin control using electric fields 131
6.3 Toward coherent electrical control 144
6.4 Conclusion 147

7 Conclusion 149

A Phase cycling and unwanted echoes 153

B Interactions and df/dB_0 157

C ^{29}Si spin decoherence models 161

CHAPTER 1

Introduction

1.1 Quantum information processing

Today's classical computers are reaching their limits. In order to increase their computing power and memory capacity, it is necessary to decrease the size of the transistors, the fundamental units of computers, as much as possible. However, today's state-of-the-art devices are crossing into the realm of quantum physics, where electrons, the propagator of information in circuits, are not bound anymore by physical barriers. This leads to both high level of noise in the computation, and therefore possible failure, as well as large power dissipation. There are many alternative solutions being researched — graphene and other two dimensional layers, molecular systems, ... — that may solve these issues, but in truth there is already little space "at the bottom". The current CMOS minimum feature (oxide barrier in a transistor) for example is but a few atomic layers, and even if we were to reduce all dimensions to a few atoms, computational power per unit area would reach it's maximum limit within decades according to Moore's law.

Quantum computing offers in principle a fundamentally different architecture than classical

computing [CN00]. Information in general is encoded into physical systems which have well defined states, usually two for binary. Where a classical system (a bit) can only be set in one of these states at a given time, a quantum system (a quantum bit or "qubit") can be in any complex linear combination, or superposition, of these states *at the same time*. This offers both a continuous set of allowed states and a phase relation between them that enrich the amount of information supported by the system. When the number of qubits is increased, the number of states exponentially increases and so does the possible size of the superposition, enabling a natural parallelization of the computation as all input states can be simultaneously tested. Though there are some fundamental limitations (related to the measurement of the system), it is expected that some computationally "hard" problems could be solved much faster using quantum computers. In particular, searching, decryption, optimization and simulation algorithms should all be greatly enhanced.

1.2 Control of quantum systems

Computing and other applications are not the only goals of quantum information; more fundamentally, it is a playground for testing our understanding of quantum mechanics and our capability for controlling these systems. As the concepts of quantum physics remain quite strange and out of our every-day life, realizations of complex manipulation of qubits becomes even more appreciable and exciting. However, such experiments are ultimately limited by our knowledge of the quantum system and its surrounding. At the typical small scales (nm) of quantum systems, objects and particles neighboring the qubit under consideration will have their own quantum properties, interacting with the qubit and creating a setting too complex to control. It is therefore necessary to decide how far to extend our knowledge of the environment and what to neglect. As increasingly better control is achieved, it becomes possible to enlarge the system and test more and more intricate models of the interactions involved, in turn further improving the control.

Obviously, such studies depend on the system being measured, and for quantum information, they are required to fulfill the criteria given by D. DiVincenzo [DiV96], which involve in particular two important but often conflicting properties:

1. **Robustness:** Any quantum system is subject to its environment. Because their interaction is generally uncontrolled, this results in an undesired evolution of the quantum system whose state becomes unknown after a given amount of time. A qubit should be robust enough that such an error occurs on a timescale much longer than the required computational time. There are two types of errors: relaxation ("flip" error) and decoherence ("phase" error).

2. **Manipulation:** To have a universal quantum computer, any desired output state must be achievable from any input state. This means being able to perform both single- and two-qubit operations. They must also be fast (compared to the error rate from relaxation or dephasing) and efficient (no control error).

The sensitivity of a qubit to its environment depends strongly on the type of system used, and this directly impacts these two properties. In both cases, the qubit responds to some perturbation, controlled or not, that modifies the qubit state. Weak relaxation and decoherence processes usually requires the qubit to be either strongly isolated or insensitive to the environment, whereas fast manipulation (and good fidelity) requires the opposite. While many quantum systems fulfill all the DiVincenzo criteria in principle, such as solid state electron and nuclear spins [Kan98, VYW$^+$00, SDK03, CKHD06], ion traps [SHO$^+$06, LOJ$^+$05], superconducting circuits [Vio02, DWM04, YN11] and more [LJL$^+$10], not so many of them have the right combination of both properties.

Spins in solid state systems such as donors in silicon offer a natural solution to this issue: they often combine two interacting qubits, an electron spin and a nuclear spin, the former being easy to manipulate and the latter having long coherence times, while relaxation is mostly suppressed for both at low temperatures. By playing on their respective strengths, it is possible to

obtain some of the most promising candidates for quantum information. The coupling between the two spins is also another parameter that can be tuned which in turn provides more control. Solid state materials hosting the qubits have furthermore complex spin environments, and while usually undesirable as it results in decoherence, it also provides more physics to play with and potentially new beneficial properties. This will be a major part of the study presented here.

1.3 Challenges for donor spins in silicon

Silicon is the most commonly used material for classical micro- and nano-fabrication; it is the textbook semiconductor and most likely one of the most studied material ever. Fabrication techniques have evolved so much that crystals ingots and wafers are extremely pure (low oxygen concentration, defect density, etc.), doping and thus resistivity are very well controlled, atomic layers of near-defect free silicon oxide can be created, and most of all, silicon is a cheap and abundant element. There are other alternatives to silicon of course, such as carbon in particular (similarly abundant, with attractive structures like graphene or nanotubes), but they are still very far from catching up. It is thus interesting that silicon offers also very promising qubits, which can only benefit from the existing semiconductor industry, and vice-versa as the technology matures. There are two types of qubits in silicon: quantum dots or similar nanostructures can be designed (such as those also studied in GaAs or SiGe), or more elementary, the dopant atoms commonly used for classical processes are natural traps at cryogenic temperatures (< 30 K) for the additional dopant electrons. The latter provide a system of coupled qubits: the spin of the trapped (or "bound") electron as well as the spin of the nucleus of the dopant atom.

1.3.1 The Kane architecture

In 1998, B. Kane presented his famous architecture [Kan98] for a scalable quantum computer using donors in silicon, more specifically ^{31}P. In the Kane model Figure 1.1, the donor nuclear spin was chosen as the qubit due to its long (population) relaxation time, already measured to

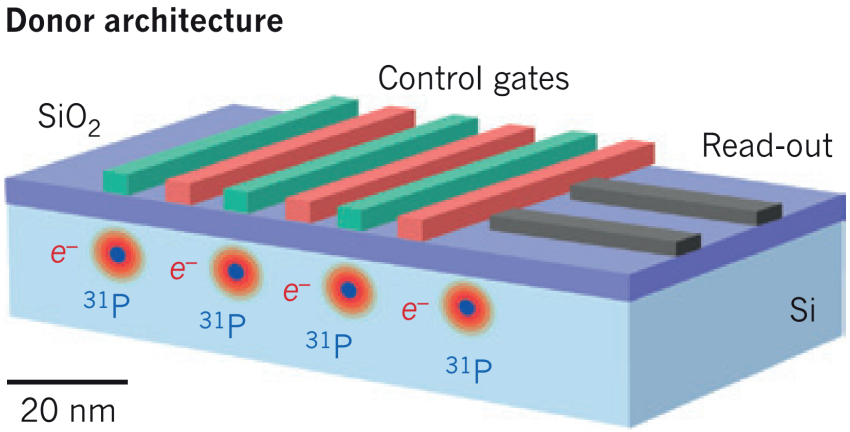


Figure 1.1: **Kane quantum computer.** Kane architecture [Kan98] for a scalable quantum computer using donors in silicon. Electrostatic tuning gates (green lines) are used to control the spins' transition frequency while hyperfine gates (red lines) enable interaction between the dopants. Image taken from [MMEL11].

be above 10 hours at 1.5 K, while the nuclear spin coherence time was generally expected to be long from NMR. In fact, from studies going back to the 1960's [GB58], a lower bound could be set by the coherence times of the electron spin which was measured to be 0.5 ms, quite impressive even today compared to some other quantum systems.

Spin manipulation in silicon can only be realized efficiently via magnetic resonance; this is quite problematic for a scalable quantum architecture as magnetic fields are difficult to confine in space and hence, so would be the local control of single qubits. To solve this issue, Kane proposed to manipulate the donor nuclear spins using a combination of global magnetic fields and local electric fields (using gates). The latter tunes the desired spins on resonance with the external magnetic field via the so-called Stark effect, which modulates the hyperfine interaction between the nuclear and electron spin of the donor. Interaction between neighboring donors would be realized by making the wavefunctions of the electrons overlap on-demand, which would affect both the electron and nuclear spin states. This would also enable initialization and measurement using spin-dependent electron tunneling between donors and looking at changes in the local charge.

From then, there have been many studies considering the feasibility of the proposal as well

as large technological improvements. Single-spin initialization, measurement and control have been realized very recently [MPZ+10, PTD+12, PTD+13], though in a different configuration (using single-electron transistors) than Kane's. Complex manipulations such as entanglement between the electron and nuclear spins were demonstrated using magnetic resonance [SBR+11]. Alternative architectures have also been proposed, in particular with spin ensembles instead of single spins, for example using holographic techniques [WGW+10] or hybrid systems with superconducting qubits [WAB+09, ML11]. Overall, donors in silicon offer a compelling system to study on the way to the goal of quantum computation.

1.3.2 Donor interaction with the spin environment

Being able to use all the classical micro-fabrication techniques is certainly a major advantage of donors in silicon, however other solid state systems such as GaAs or SiGe would then be similarly competitive. Where donors in silicon really shine as quantum systems is in the extremely long coherence times of either their electron or nuclear spin.

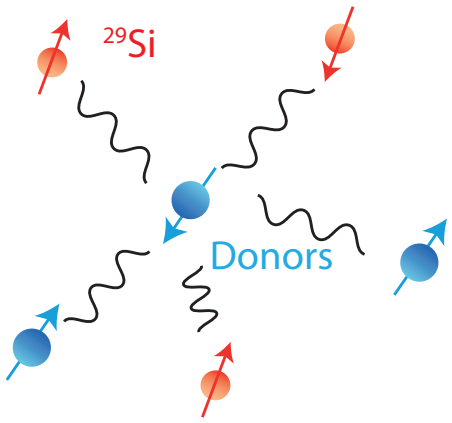


Figure 1.2: **Illustration of the spin environment around a donor in silicon.**

These coherence times have been successively characterized and improved over the past 10 years, at least in spin ensembles of ^{31}P donors. At low temperatures ($5-10$ K) and in a standard silicon wafer, the electron coherence time is about 0.3–0.5 ms [GB58], and limited by the local spin environment in the silicon lattice. These spins are either from the ^{29}Si isotope

in natural silicon ($\approx$ 5 % abundance) which has a nuclear spin, or simply from the donors themselves depending on the doping concentration (usually about $10^{14} - 10^{16}$ cm^{-3}). This is illustrated in Figure 1.2. By removing the ^{29}Si spins with isotopic purification and using silicon samples with low dopant concentrations, the electron spin coherence time was lengthened to about 0.5 s [TTM$^+$11], while the nuclear spin coherence was measured to last up to 3 minutes [MTB$^+$08, SST$^+$12]. Finally, by ionizing the donor, the nuclear spin becomes completely isolated and its coherence times can reach up to hours [SSS$^+$13].

Despite such long coherence times, there are still many questions and challenges to answer:

1. *Beyond ^{31}P? :* There are few studies on other Group V donors in silicon beside ^{31}P. While they are expected to be very similar, there are some subtle differences, such as the nuclear spin number being larger ($> 1/2$), which can have some consequences on the spin coherence times for example. ^{209}Bi in particular has the largest nuclear spin (9/2) and has been the subject of some recent investigations [GWR$^+$10, MWS$^+$10], which I also pursue throughout this work.

2. *The end of natural silicon? :* Natural silicon ($^{\text{nat}}$Si) which gives short coherence times is still the most common material, as it is used in industry, whereas isotopically purified samples remains quite rare. If the spin coherence times in $^{\text{nat}}$Si could be improved by other means, it would therefore be beneficial. In addition, the presence of the ^{29}Si spins can perturb interactions between donors, and can actually dampen corresponding decoherence processes in silicon samples with high doping concentration. Two solutions are investigated here: "dynamical decoupling" in Chapter 4 and "clock transitions" in Chapter 5. Dynamical decoupling, which is a technique used in magnetic resonance, can be used to effectively remove the interaction of a qubit to the environment during its evolution. First developed in the context of liquid state NMR [Hah50, HW68], it has been adapted and increasingly used in many qubit systems over the past years [BUV$^+$09, dLWR$^+$10, BGPJ$^+$13]. Clock transitions are special regimes of a qubit where it can become insensitive to some interactions, e.g. to the magnetic or ^{29}Si spin environ-

ment in the case of donors in silicon. They have been used with great success in the past in superconducting qubits [KYG+07].

3. *Understanding the environment:* Beyond obtaining the longest coherence times, understanding the interaction between the various quantum systems involved in decoherence processes is a fundamental question in quantum mechanics. The many interactions between the donors, between the ^{29}Si nuclear spins, and between the donors and the ^{29}Si nuclear spins create a complex system to simulate. Therefore, experimental validations are required to confirm theoretical models: this is realized in two instances in Chapter 4 and Chapter 5 where the ^{29}Si bath is probed. In addition, the donor can be strongly coupled to some of the ^{29}Si nuclear spins in the environment, leading to possible use of these spins as ancillary qubits, as was realized in other solid-state systems such as Nitrogen-Vacancy centers in diamond [TCvdS+14, WWZ+14].

1.3.3 Donor interaction with the electric environment

In the Kane model, local electric manipulation of the nuclear spins is a key component for large scalability. Yet, there has been remarkably few experimental works measuring the donor spins sensitivity to an applied electric field, as well as no demonstration of actual electrical qubit control to modify the response to a global magnetic field. The main reason for this lack of experiment is the weak influence of electric fields due to the Stark effect. In particular, large electric fields are difficult to obtain in bulk silicon crystals, and single spin devices, where this would be more easily achievable, have been successfully fabricated only very recently. Measurements of the electric sensitivity was first realized in ^{121}Sb [BTS+06] and later in ^{75}As [LSL+14], both on the donor electron spin only (though the Stark effect, being mainly a shift in the hyperfine coupling strength, affects similarly the donor nuclear spin). In Chapter 6, I therefore show full characterization of the Stark shift on all Group V donors in silicon. Depending on the donor, the electric field effect can differ by more than an order of magnitude, therefore such measurements are important in choosing the right donor for a silicon quantum architecture. Finally, this

is followed by the first demonstration of electric tuning of the nuclear spin transition frequency, enabling switching on-demand the nuclear spin response to an applied RF magnetic field, as was initially proposed by Kane.

CHAPTER 2

Quantum information and spin resonance

In this Chapter, I present both the theoretical and experimental basics required to understand this thesis. This is but a brief summary designed to define properly the various terms and equations used. A more proper development, in particular for the purpose of magnetic resonance, can be found in [CN00, Lev09, SJ01].

2.1 Quantum information

2.1.1 Quantum states and their evolution

Quantum state representation

For information to physically be stored and manipulated, it is desirable for a system to have a set of well-defined states in which it can be encoded. Generally, they are arbitrarily defined values (or set of values) of a free parameter of the system. For example, a bit, that is a system for binary encoding, can be made from two specific voltage amplitudes in a circuit, while any other value

of voltage would be forbidden by design. Quantum systems used for information processing are at first similar, however such free parameter must be a quantum property such as position, momentum, polarization, etc ... The states associated to each value of that parameter belong to a Hilbert space that allows for any linear combination, or superposition, of these states to exist simultaneously, with therefore an infinite number of acceptable states. The system can still be simply defined by a set of d orthogonal states that spans the Hilbert space (with dimension d), which are usually stationary solutions called eigenstates. Those are denoted by a wavevector with the Dirac notation $|i\rangle$, where i represents the value of the free parameter. Any other states can therefore be written as $|\psi\rangle$:

$$|\psi\rangle = \sum_{i=1}^{d} \alpha_i |i\rangle \tag{2.1}$$

where α_i are complex amplitudes and may be time dependent. When measuring (or "observing") any quantum system, it cannot remain in a superposition and will collapse to one of the eigenstates with probability given by the square of the corresponding α_i. The norm $|\langle\psi|\psi\rangle| = \sum_{i=1}^{d} |\alpha_i|^2$ or total probability is then equal to 1. An alternative representation to the wavevector is the density matrix, which can further describe statistical mixtures of many states from ensembles of systems or systems having undergone random processes. It is defined by a Hermitian matrix with dimension $d \times d$ such that:

$$\rho = \sum_{k} p_k |\psi_k\rangle \langle\psi_k| \tag{2.2}$$

where $\langle\psi_k|$ is the Hermitian transpose of the vector $|\psi_k\rangle$, and $|\psi_k\rangle$ are pure states with probability distribution p_k. The norm is now defined by the trace $\mathrm{Tr}(\rho)$ which is the sum of its diagonal elements, and must be equal to 1. Because the diagonal terms are equal to $|\alpha_i|^2$, this also results in $\sum_k p_k = 1$. If a density matrix can be expressed in terms of a single wavevector $\rho = |\psi\rangle\langle\psi|$, the state $|\psi\rangle$ is called pure, otherwise it is mixed. They can be distinguished by looking at the Hilbert-Schmidt norm $\|\rho\|^2 = \mathrm{Tr}\left(\rho^2\right)$ of the matrix: it is equal to 1 for pure states and below 1 for mixed ones. The diagonal elements of the density matrix represents the **population** of the

system for each eigenstate, that is the "classical" information. The off-diagonal elements on the other hand are purely quantum as they result from a superposition, and describe the correlations —or **coherences**— between the various eigenstates.

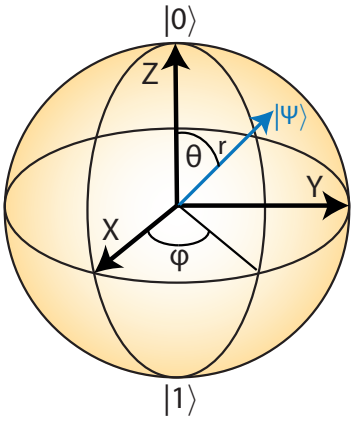


Figure 2.1: **Bloch sphere representation.** Any pure state can be defined as a point on the surface of the Bloch sphere using the angles θ and ϕ. For a mixed state, the norm r of the arrow can be smaller.

A d-dimensional Hilbert space with $d > 2$ is difficult to grasp intuitively and to perform calculations on; it is therefore usual to try to reduce it as much as possible to simple two-level systems. They are also the quantum equivalent of classical binary systems and hence called quantum bits or "qubits". Experimentally, control of the system is also limited in most cases to transfer or creation of superposition between two specific eigenstates, hence this restriction presents an adequate model. A two-level system with two eigenstates written $|0\rangle$ and $|1\rangle$ (similar to the classical 0 and 1) can be pictured with a Bloch sphere as shown in Figure 2.1. An arbitrary pure state is described by two complex numbers (a_0 and a_1 as defined in Eq. 2.1), however because it has a norm of 1 and any global phase can generally be neglected ($e^{i\Phi}|\psi\rangle \equiv |\psi\rangle$), it has only two real degrees of freedom and therefore will be a point on the surface of the sphere. $|\psi\rangle$ is then:

$$|\psi\rangle = \cos(\theta/2)|0\rangle + \sin(\theta/2)e^{+i\phi}|1\rangle \tag{2.3}$$

where θ and ϕ are the altitude and azimuth angles, respectively. For a mixed state, the Hilbert-Schmidt norm is less than 1 and so may span the full interior of the sphere.

In this thesis, we will be solely interested in spins, the intrinsic angular momentum of particles. Because spins are typically pictured as a sort of quantum magnet, they are represented by an arrow originating from the center of the Bloch sphere with length its norm. This arrow is expressed as a vector decomposed along a Cartesian basis made by three orthogonal axis X, Y and Z, which can themselves be described by a set of matrices (or "operators") $\{\mathbb{1}, S_x, S_y, S_z\}$ called the normalized Pauli basis. For $d = 2$, they are defined as:

$$\mathbb{1} = \begin{pmatrix} 1 & 0 \\ 0 & 1 \end{pmatrix}, \; S_x = \frac{1}{2}\begin{pmatrix} 0 & 1 \\ 1 & 0 \end{pmatrix}, \; S_y = \frac{1}{2}\begin{pmatrix} 0 & -i \\ i & 0 \end{pmatrix}, \; S_z = \frac{1}{2}\begin{pmatrix} 1 & 0 \\ 0 & -1 \end{pmatrix} \tag{2.4}$$

Any density matrix can then be defined with these four operators such that:

$$\rho = \frac{\mathbb{1}}{2} + r_x S_x + r_y S_y + r_z S_z \tag{2.5}$$

where $r_{x,y,z}$ are complex coefficients satisfying $\|\rho\|^2 \leq 1$ and $\frac{\mathbb{1}}{2}$ is required for normalization as the other matrices are traceless ($\mathrm{Tr}(S_{x,y,z}) = 0$). The arrow in the Bloch sphere illustration of Figure 2.1 is hence a vector $[r_x \; r_y \; r_z]^T$ in the Cartesian representation defined by $\mathbf{S} = [S_x \; S_y \; S_z]^T$. For spin systems with higher dimension (e.g. ^{121}Sb or ^{209}Bi donors in silicon), the Pauli matrices can still be defined:

$$\begin{gathered} (\mathbb{1})_{n,n} = 1 \\ (S_x)_{n,n\pm1} = \sqrt{S(S+1) - m_S(n)(m_S(n)\pm 1)} \\ (S_y)_{n,n\pm1} = \mp i\sqrt{S(S+1) - m_S(n)(m_S(n)\pm 1)} \\ (S_z)_{n,n} = m_S(n) \\ \text{with } m_S(n) = S - n - 1 \end{gathered} \tag{2.6}$$

where $()_{m,n}$ is the matrix element at the row m and column n for $m,n = 1..(2S+1)$, and all other

elements are 0. For example, a spin with $S = 5/2$ has the following Pauli matrices:

$$\mathbb{1} = \frac{1}{2}\begin{pmatrix} 1 & 0 & 0 & 0 & 0 & 0 \\ 0 & 1 & 0 & 0 & 0 & 0 \\ 0 & 0 & 1 & 0 & 0 & 0 \\ 0 & 0 & 0 & 1 & 0 & 0 \\ 0 & 0 & 0 & 0 & 1 & 0 \\ 0 & 0 & 0 & 0 & 0 & 1 \end{pmatrix}, \; S_x = \frac{1}{2}\begin{pmatrix} 0 & \sqrt{5} & 0 & 0 & 0 & 0 \\ \sqrt{5} & 0 & 2\sqrt{2} & 0 & 0 & 0 \\ 0 & 2\sqrt{2} & 0 & 3 & 0 & 0 \\ 0 & 0 & 3 & 0 & 2\sqrt{2} & 0 \\ 0 & 0 & 0 & 2\sqrt{2} & 0 & \sqrt{5} \\ 0 & 0 & 0 & 0 & \sqrt{5} & 0 \end{pmatrix} \tag{2.7}$$

$$S_y = \frac{i}{2}\begin{pmatrix} 0 & -\sqrt{5} & 0 & 0 & 0 & 0 \\ \sqrt{5} & 0 & -2\sqrt{2} & 0 & 0 & 0 \\ 0 & 2\sqrt{2} & 0 & -3 & 0 & 0 \\ 0 & 0 & 3 & 0 & -2\sqrt{2} & 0 \\ 0 & 0 & 0 & 2\sqrt{2} & 0 & -\sqrt{5} \\ 0 & 0 & 0 & 0 & \sqrt{5} & 0 \end{pmatrix}, \; S_z = \frac{1}{2}\begin{pmatrix} 5 & 0 & 0 & 0 & 0 & 0 \\ 0 & 3 & 0 & 0 & 0 & 0 \\ 0 & 0 & 1 & 0 & 0 & 0 \\ 0 & 0 & 0 & -1 & 0 & 0 \\ 0 & 0 & 0 & 0 & -3 & 0 \\ 0 & 0 & 0 & 0 & 0 & -5 \end{pmatrix} \tag{2.8}$$

Spin evolution and rotations

The evolution in time of a quantum system is described by the Schrödinger equation:

$$\frac{d\,|\phi(t)\rangle}{dt} = -iH(t)\,|\phi(t)\rangle \tag{2.9}$$

where $H(t)$ is the Hamiltonian of the system. In this entire work, it is easier to work in the frequency domain for comparison with experiments and therefore the Planck constant $\hbar$ is not used. For a time-independent Hamiltonian H, the eigenstates $|i\rangle$ are stationary solutions of this evolution, that is their probability density (a_i) is constant, such that $H\,|i(t)\rangle = E_i\,|i(t)\rangle$ where E_i is the eigenenergy (or eigenfrequency in the linear frequency domain). Solving the Schrödinger

equation hence gives $|i(t)\rangle = e^{-iE_i t}|i(t=0)\rangle$; the eigenstate only acquires a global phase factor. For density matrices the Schrödinger equation is:

$$\frac{d\rho(t)}{dt} = -i[H(t), \rho(t)] \tag{2.10}$$

where $[H(t), \rho(t)] = H(t)\rho(t) - \rho(t)H(t)$ is the matrix commutator. Solving the equation for a time-dependent Hamiltonian can be quite hard, and often impossible or computationally intensive; thankfully for the majority of the experiments the Hamiltonian is time-independent, either entirely or by parts in time. In this case, the evolution for a spin is equivalent to a rotation around an arbitrary axis of the Bloch sphere. This rotation is a unitary operator U, called a "propagator", and the solution of Eq. 2.10 becomes:

$$\rho(t) = U\rho(0)U^{\dagger} \text{ with } U = e^{-iHt} \tag{2.11}$$

where $\rho(0)$ is the density matrix before evolution. If many operations $U_{n=1..N}$ are applied sequentially, they can be combined together in a single unitary operator $U = U_N \times .. \times U_1$. Because the propagator U is unitary, the Hilbert-Schmidt norm of the density matrix before and after the operation are equal. This means that a mixed state, for example from a population of spins, can never become pure without using non-unitary operations such as measurement, relaxation (see below), or more generally involving interaction with other quantum systems.

Similar to ρ, H can also be decomposed in the Pauli terms $S_{x,y,z}$, corresponding to rotations around X, Y and Z. In general, the identity term is always neglected, both for H and ρ, because it commutes with all the other operators and therefore does not contribute in any way to the evolved quantum state. For a given rotation axis $L = l_x S_x + l_y S_y + l_z S_z$ with $\sqrt{l_x^2 + l_y^2 + l_z^2} = 1$ and angular frequency ω, the propagator is $U = e^{-i\omega L t}$ and Eq. 2.11 becomes directly equal to:

$$\rho(t) = \cos(\omega t)\rho(0) - \mathrm{i} \times \sin(\omega t)[L, \rho(0)] \tag{2.12}$$

assuming $[L, \rho(0)] \neq 0$ and $[L, [L, \rho(0)]] = \rho(0)$, which holds if L and $\rho(0)$ are Pauli matrices

for example. For $[L,\rho(0)]=0$, there is no evolution and $\rho(t)=\rho(0)$. Eq. 2.12 above is very handy for solving the evolution of a qubit.

A qubit is rarely isolated; it will interact, more or less strongly, with other quantum systems nearby. For example, for two spins S_1 and S_2, interactions have the form $S_{1x,y,z}\otimes S_{2x,y,z}$ where $\otimes$ is the Kronecker product which, for simplicity, will be mostly discarded here. Typically, the two qubit system starts from two separable states $\rho(0)=\rho_1(0)\otimes\mathbb{1}+\mathbb{1}\otimes\rho_2(0)\equiv\rho_1(0)+\rho_2(0)$, and then may slowly become entangled such that $\rho(t)\neq\rho_1(t)+\rho_2(t)$. For many spins, the density matrix or the Hamiltonian can be decomposed into the terms of the product of the different Pauli bases, e.g $S_{1x}\mathbb{1}, S_{1z}S_{2x}, ...$

2.1.2 Relaxation, polarization and decoherence

One of the main challenges for quantum computing is overcoming relaxation and decoherence. As the qubit is manipulated to some determined state, it does not remain indefinitely unchanged over time; instead, it either decays back to one of its eigenstates or slowly sees its phase being shifted. The first phenomenon is called population "relaxation" and the second "decoherence."

Relaxation is akin to the introduction of classical errors in computation as the qubit flips between $|0\rangle$ and $|1\rangle$. The characteristic time for a flip to occur depends on the system being measured, and also on the energy of each eigenstates. Over time, the system reaches a steady-state thermal equilibrium of its population with a density matrix following Boltzmann statistic:

$$\rho_{\text{thermal}}=\frac{1}{Z}\exp(-\beta H) \tag{2.13}$$

where $\beta=1/(k_BT)$ with k_B the Boltzmann constant and T the temperature, H is the system Hamiltonian and Z is the canonical partition function (normalization for $\text{Tr}\,(\rho_{\text{thermal}})=1$). The population distribution is the average time a spin spends at each eigenstate. For a spin ensemble, it also corresponds to a spatial distribution across the material. For the experimental conditions relevant for this work, the temperature and energies are such that $\beta H<1$ and the thermal state is $\approx\frac{1}{Z}(\mathbb{1}-\beta H)$ which is close to a pure mixed state i.e. $\mathbb{1}$. Because $\mathbb{1}$ does not evolve in time (it

commutes with all operators) and thus does not participate in the computation, it is negligible and the thermal state can be written in the simple form $\rho_{\text{thermal}} \equiv -\frac{\beta}{Z}H$. For a single qubit in a thermal state, this is called the "pseudo-pure" approximation [Jon11]. $\frac{\beta}{Z}$ is then just a normalization factor which can also be disregarded from calculations. Thus, a spin-1/2 with Hamiltonian $H = \omega S_z$ simply has for initial density matrix $\rho_{\text{thermal}} \equiv -S_z$. For larger β, the system becomes more polarized and the density matrix more pure. If the state populations are taken out of equilibrium, the characteristic timescale for the system to go back to the thermal state is called T_1. Experimentally, it provides i) an upper bound for the duration of a control sequence applied to spins without a random change in their population and ii) a minimum delay between experiments in order for the system to be initialized into the same thermal state (notwithstanding other processes such as optical relaxation).

Decoherence represents an uncontrolled phase shift ϕ of the qubit. It arises from a frequency shift, and hence a phase shift, described by an undesired Z rotation with either/both a temporal or/and spatial distribution. Starting from a pure state in a coherent superposition, the phase becomes distributed after some time across a plane perpendicular to Z —defined by the population values— in the Bloch sphere. The average phase value hence decays to zero with a characteristic time called T_2.

Though mostly unused in this work, a general description of relaxation and decoherence is possible but requires non-unitary operations which can be obtained from a master equation, e.g using the Lindblad form (Markovian evolution only):

$$\frac{d\rho}{dt} = -i[H,\rho] + \sum_{n,m} \Gamma_{n,m} \left(L_n \rho L_m^\dagger - \frac{1}{2} \left(\rho L_m^\dagger L_n + L_m^\dagger L_n \rho \right) \right) \tag{2.14}$$

where $L_{m,n}$ are rotation operators forming a basis (e.g. the Pauli basis) and $\Gamma_{m,n}$ are associated constants that determine the non-unitary evolutions, that is the population or coherence decays. In this context, relaxation for a spin-1/2 system is the combined absorption and emission be-

tween states described by:

$$\frac{\Gamma_1}{1+e^{-\beta H}}\left(S_+\rho S_+^\dagger - \frac{1}{2}\left(\rho S_+^\dagger S_+ + S_+^\dagger S_+\rho\right)\right) + \tag{2.15}$$

$$\frac{\Gamma_1 e^{-\beta H}}{1+e^{-\beta H}}\left(S_-\rho S_-^\dagger - \frac{1}{2}\left(\rho S_-^\dagger S_- + S_-^\dagger S_-\rho\right)\right) \tag{2.16}$$

where $S_\pm = S_x \pm iS_y$ are the annihilation and creation operators, and H is the diagonalized Hamiltonian (eigenvalues). The Boltzmann factor influences the relaxation rates leading to the steady state solution ρ_{thermal} with a characteristic time $T_1 = 1/\Gamma_1$. For relaxation, the terms in the master equations are due to Z rotations:

$$2\Gamma_2\left(S_z\rho S_z^\dagger - \frac{1}{2}\left(\rho S_z^\dagger S_z + S_z^\dagger S_z\rho\right)\right) \tag{2.17}$$

with similarly $T_2 = 1/\Gamma_2$. In addition, the population relaxation described previously also leads to a coherence decay such that T_2 can be calculated to be limited by $2\times T_1$ for pure X and Y relaxation. In the case of donors in silicon, T_2 is in fact measured to be limited by $1\times T_1$ (using conventional experiments as described in Section 2.2.3) as the mechanism for the population decay is isotropic, and thus gives simultaneously the X/Y relaxation and an additional Z dephasing governed by the same Γ_1 rate.

2.2 Magnetic resonance

In the previous Section, I described a spin qubit mathematically, but how is it realized experimentally? We are interested here in the spins of electrons and nuclei which are mainly susceptible to magnetic interactions. It is through those that the spin qubits can be defined, manipulated and measured.

2.2.1 Theory of magnetic resonance

Spins must have non-degenerate eigenenergies in order to be properly controlled, otherwise their states cannot be distinguished. For spins, these energies are mainly defined by the Zeeman interaction with a magnetic field B_0 (along the Z axis), which gives the following Hamiltonian:

$$H_0 = -\gamma B_0 S_z \tag{2.18}$$

where γ is the gyromagnetic ratio of either the electron or the nuclear spin. This Hamiltonian is already diagonal and thus in the eigenbasis, with eigenstates $|\uparrow\rangle$ and $|\downarrow\rangle$ and eigenfrequencies $\pm\frac{1}{2}\gamma B_0$. The frequency difference is $\omega_0 = -\gamma B_0$, and the Hamiltonian can be written $H_0 = \omega_0 S_z$ (Figure 2.2(a)).

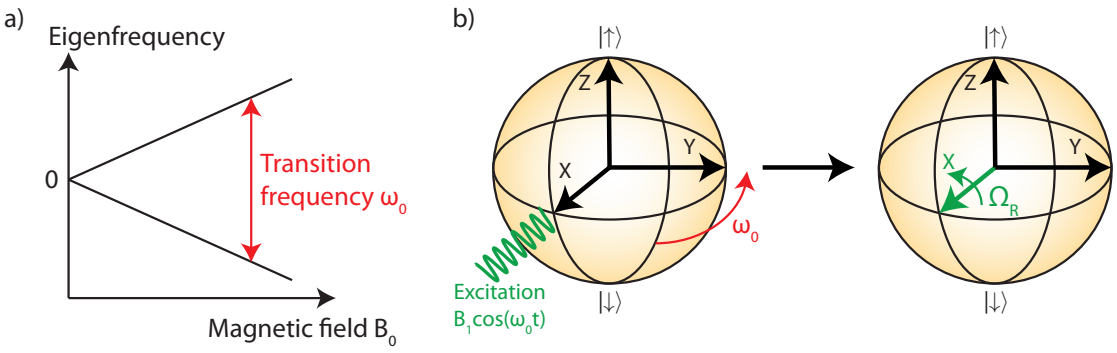


Figure 2.2: **Rotating frame.** a) Eigenfrequencies for a spin-1/2 under an external magnetic field. ω_0 is the difference in eigenfrequencies between two states. b) Rotating frame approximation: under change of basis, a magnetic excitation resonant with a spin rotating at ω_0 is equivalent to a pure rotation for an unmoving spin.

The evolution under this Hamiltonian is a rotation around the Z axis, the so-called Larmor precession. Theoretically, one could just realign the magnetic field from one axis to another to control the spin, however B_0 must usually be quite large for high thermal polarization, necessary to obtain as pure initial states as possible, and therefore a rapid change of the field (in nano/microseconds) is experimentally not viable. The alternative solution to manipulate spins is to send an excitation, i.e. a magnetic field oscillating with some frequency ω for a finite time,

and whose orientation is orthogonal to B_0. The Hamiltonian can thus be written as:

$$H(t) = \omega_0 S_z + \gamma B_1 \cos(\omega t + \phi) S_x \tag{2.19}$$

where B_1 and ϕ are the excitation amplitude and phase, respectively. This is time-dependent and so the evolution does not have a direct solution. This problem can be solved by changing the spin basis from the "laboratory frame", i.e. the frame in which the fields B_0 and B_1 are fixed along X and Z respectively, to a reference frame (the "rotating frame") which rotates around Z at the spin Larmor precession. This change in basis is defined by the operator $P = e^{-i\omega_0 t S_z}$ and is applied to the density matrix $\rho(t) \to P^\dagger \rho(t) P = \rho_{RF}(t)$. In this case, the Schrödinger equation Eq. 2.10 becomes:

$$\frac{d\rho(t)}{dt} = -i[H(t), \rho(t)] \Rightarrow \frac{dP\rho_{RF}(t)P^\dagger}{dt} = -i[H(t), P\rho_{RF}(t)P^\dagger] \tag{2.20}$$

$$\Rightarrow P\frac{d\rho_{RF}(t)}{dt}P^\dagger = -i[H(t) - \omega_0 S_z, P\rho_{RF}(t)P^\dagger] \tag{2.21}$$

$$\Rightarrow \frac{d\rho_{RF}(t)}{dt} = -i[P^\dagger(H(t) - \omega_0 S_z)P, \rho_{RF}(t)] = -i[H_{RF}(t), \rho_{RF}(t)] \tag{2.22}$$

$H_{RF}(t)$ is the Hamiltonian in this new basis. It is equal to $P^\dagger(\omega_0 S_z + \gamma B_1 \cos(\omega t + \phi) S_x - \omega_0 S_z)P = \gamma B_1 \cos(\omega t + \phi) P^\dagger S_x P$ and the Z component is eliminated. According to Eq. 2.12, we have $P^\dagger S_x P = \cos(\omega_0 t) S_x - \sin(\omega_0 t) S_y$, hence the Hamiltonian is:

$$H_{RF}(t) = \gamma B_1 \cos(\omega t + \phi)[\cos(\omega_0 t) S_x - \sin(\omega_0 t) S_y] \tag{2.23}$$

$$= \frac{1}{2}\gamma B_1 [(\cos((\omega - \omega_0)t + \phi) + \cos((\omega + \omega_0)t) + \phi) S_x \tag{2.24}$$

$$+ (\sin((\omega - \omega_0)t + \phi) - \sin((\omega + \omega_0)t + \phi)) S_y] \tag{2.25}$$

If the excitation is on resonance with the Larmor precession, i.e. $\omega = \omega_0$, we have $H_{RF}(t) = \frac{1}{2}\gamma B_1 [\cos(\phi) S_x + \sin(\phi) S_y + \cos(2\omega_0 t + \phi) S_x - \sin(2\omega_0 t + \phi) S_y]$. The double frequency corresponds to a very fast evolution which will simply be averaged out (there is no time for the spin

to rotate as $\gamma B_1 \ll \omega_0$). Those terms can be disregarded: this is the "rotating wave approximation". Finally, $H_{RF}(t) = \frac{1}{2}\gamma B_1(\cos(\phi)S_x + \sin(\phi)S_y)$ is a pure rotation along an axis in the $X-Y$ plane defined by the excitation phase ϕ and the spin can freely rotate in the rotating frame as shown in Figure 2.2(b). $\frac{1}{2}\gamma B_1 = \Omega_R$ is the precession frequency along this axis and is called the "Rabi" frequency. Specific rotation angles θ are realized by pulsing the excitation for the right duration T_{pulse} and power B_1 such that $\theta = \Omega_R T_{\text{pulse}}$. For universal control of the spin within the Bloch sphere, a minimum of two orthogonal control axes is required. Here B_1 was applied only along X as it is experimentally rare to be able to produce excitations along more than one axis, yet thanks to the phase ϕ it is possible to choose arbitrarily between X and Y in the rotating frame and thus the qubit can be fully manipulated.

This technique forms the basis of magnetic resonance. If the spin is a nuclear spin and at magnetic fields of few T, $\omega/(2\pi)$ is between 10 and 100 MHz and the resonant excitation is in the radio-frequency (RF) regime: this is called Nuclear Magnetic Resonance (NMR). Here, we are more concerned with the electron spin, and thus Electron Spin Resonance (ESR), whose larger gyromagnetic ratio (by a factor of $10^3 - 10^4$) gives a frequency in the microwave (MW) regime, e.g. 10 GHz at X-band, around 0.3 T.

2.2.2 ESR measurements and experimental apparatus

There are two principal classes of ESR experiment: the first uses continuous-wave microwave fields and is mainly used to measure at which magnetic field B_0 the MW frequency is on resonance with the spins; this method is not used in this thesis and is not discussed further. The second type is pulsed ESR that uses pulsed excitations to coherently control a spin ensemble, a necessary requirement for quantum information. Measurements in conventional pulsed ESR (or NMR) systems are realized by detecting the emission of photons from the spins when they are in a coherent state. Classically, if an electromagnetic coil is placed around the material containing the spins, their Larmor precession when in a superposition creates a fluctuating magnetic field that produces a detectable current, i.e. a signal, in the coil. In the quantum picture, the

spins couple with the electromagnetic environment and transfer of energy occurs between the two via spontaneous emission of MW photons. As the spins of the ensemble are in-phase after the application of the initial $\pi/2$ pulse (and at the echo time), they are not independent magnetic moments and so they emit coherently in the cavity at a rate proportional to the square of the number of spins, instead of just linearly (and hence undetectable) if the emission was incoherent [SJ01]. The measurement thus only detect the projection of the spins along the X and Y axis (i.e. in a coherent state), that is the expectation value $\langle\psi|S_{x,y}|\psi\rangle$ (often written $\langle S_{x,y}\rangle$) for vectors or $\mathrm{Tr}(S_{x,y}\rho)$ for density matrices. At very high temperature where the density matrix is purely mixed (equal to $\mathbb{1}$), this value is zero and no signal can be measured. This is why low temperatures and high spin frequencies, usually from large magnetic fields, are required to obtain states as pure as possible (or "polarized") and therefore good measurements. This is also one reason why ESR is usually more sensitive than NMR, though even for ESR the states are mostly mixed (≈ 5 % polarization around 10 GHz and 5 K).

The spin-cavity coupling and therefore the entire detection process is typically very weak and it is not possible to measure single spins, only very large numbers, or "ensembles", of them. This is due to two reasons: first, the spin is simply a weak magnetic dipole, and second, in an ensemble each spin has a slightly different Larmor frequency due to inhomogeneous magnetic field and/or different local environment, hence the emission intensity will be more spread in the frequency domain, with typical ESR linewidths in the MHz. High ESR sensitivity requires both the use of low-noise detection electronics and placing the sample in a resonator to enhance the energy transfer/ reduce high frequency loss (see below for more details). The usual figure of merit for the ESR sensitivity of a spin ensemble, at X-band and temperatures around 4-10 K, is about $10^4 - 10^5$ (spins/Hz)/$\sqrt{\mathrm{Hz}}$ (per ensemble linewidth frequency, per square root of inverse acquisition time) and so around 10^{10} spins/$\sqrt{\mathrm{Hz}}$.

A pulsed ESR spectrometer can be divided into three principal components as illustrated in Figure 2.3:

1. *Source:* A MW source produces a continuous oscillating voltage signal at MW frequen-

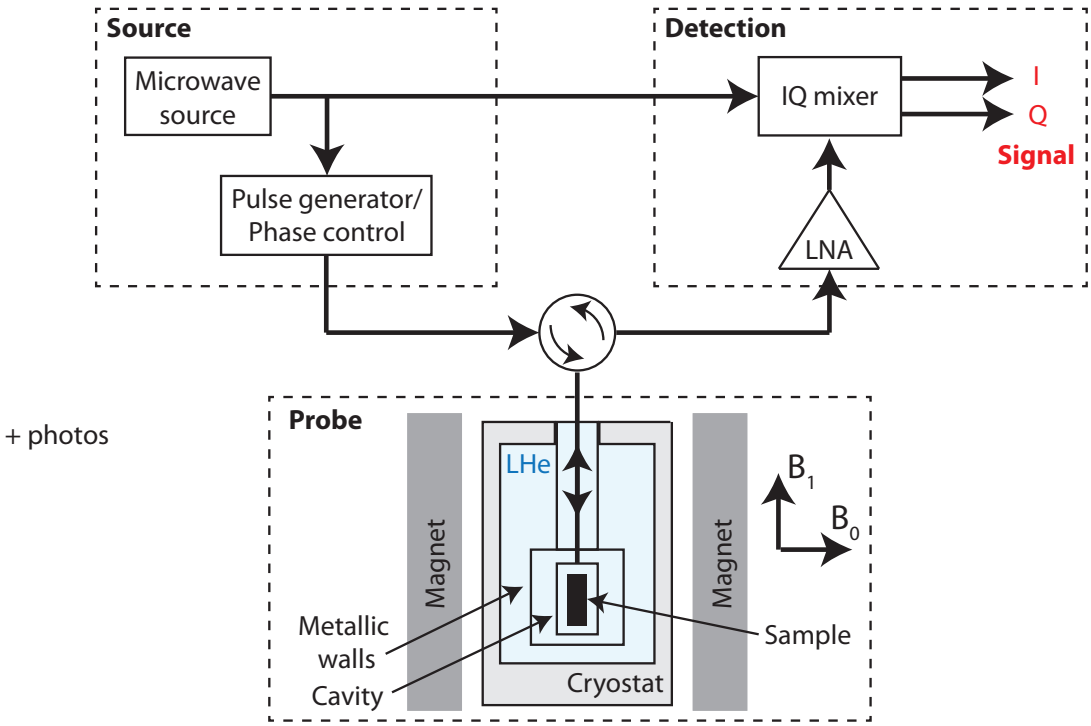


Figure 2.3: **Diagram of an ESR spectrometer.** A spectrometer has three main components: a MW source to create the pulses, a probe within a magnet (B_0) with the sample within a resonator to couple the MW (B_1) to the spins and a detection part to demodulate the MW signal from the spins. "LNA" stands for low-noise amplifier and "LHe" for liquid helium.

cies. This is then divided in two: one part goes to a pulse forming unit which transmits microwave pulses at the right time and for the right duration. The second part of the MW signal is used as reference for the detection block. The pulses can also be more complex by modulating the MW signal to provide arbitrary pulse shapes and phases. High power amplifiers (up to kW) are often used afterward to increase the pulse amplitude and thus the Rabi frequency.

2. *Probe:* For measurement, the sample is inserted in a cavity, and together placed within a large electromagnet to obtain the external magnetic field B_0 and, if necessary, inside a continuous-flow helium cryostat to be cooled down to low temperatures. The incoming resonant pulses are directed via a MW circulator into an antenna that couples to the cavity, which enhances both the excitation and detection of the spins. Reversely, the output photons are picked up by the antenna and directed out of the cavity and toward the detection

components.

3. *Detection:* The signal from the sample, even with the resonator, is still quite weak (comparable with the Johnson-Nyquist noise, ≈ -120 dBm typical at room temperature) and a low-noise amplifier or even multi-stage amplification is required for getting the highest signal-to-noise ratios. In addition, the signal is a MW at the Larmor frequency, matched by the MW source when on resonance, and so can be demodulated using the latter in an IQ mixer. Using quadrature detection, the I and Q outputs represent the projection of the spin states onto the X and Y axes, or any orthogonal combination.

For most experiments presented in this thesis, I used Bruker Elexsys E680 and E580 spectrometers designed to work at X-band at 9-10 GHz. The cavity in the probe is a dielectric resonator fabricated out of a sapphire cylinder that confines the magnetic field within its center (where the sample sits), and with Q factors tunable up to 20000. Pulses can be created with nanosecond resolution, however the maximum experiment time using the built-in pulse sequencer is limited to 1 s. This limitation was a problem for some of the long coherence time experiments and therefore a home-made source/pulse forming unit was built. This allowed to: increase the spectrometer bandwidth, create pulse sequences for arbitrary long times, modulate the pulses to arbitrary shapes, and overall have more control over the experimental apparatus.

2.2.3 Typical ESR experiments

The most basic way to obtain an ESR signal from a spin ensemble is to apply a $\Omega_R t = \pi/2$ pulse (always around X or Y unless otherwise mentioned) to the spins to excite them from thermal polarization to a X and Y magnetisation where they will emit photons. The spins in the rotating frame and without pulses should not evolve over time; yet for an ensemble of spins, they each have slightly different frequencies $\omega_0 + \delta\omega_0$ (so called "inhomogeneous broadening") and so each slowly diverge from one another, acquiring different phases. The total detected signal slowly disappears as the net X and Y magnetisation goes to 0. The decay time associated with

this broadening is called T_2^* and is in the order of ns to μs, which is similar to most pulse durations and thus is too short to allow for long computations (many rotations).

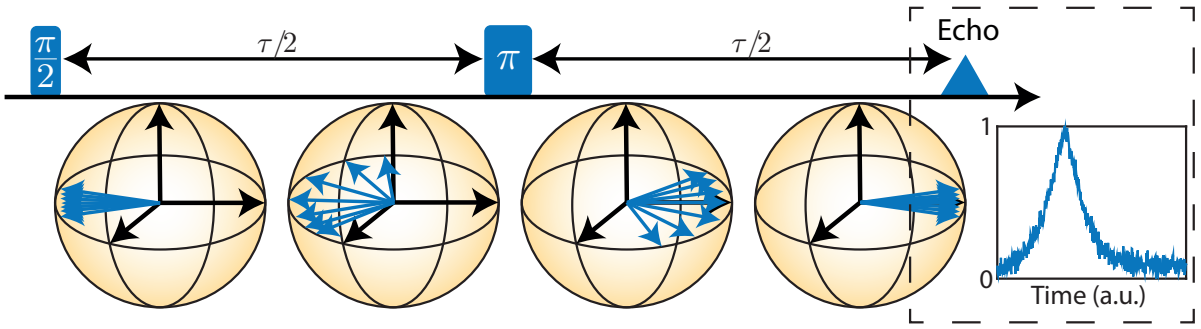


Figure 2.4: **Hahn echo.** The Hahn echo is a core sequence for measuring pulse ESR signals. The middle π-pulse "refocuses" the spins, canceling the phase acquired before and after. The Bloch sphere represents an ensemble of spins evolving through the sequence. On the right side, a typical Hahn echo experimental signal.

In order to solve the issue, a second pulse with rotation angle π can be applied to cancel this effect if the broadening is static in time, as shown in Figure 2.4. The pulse reverses the sign of the phase $\phi = \delta\omega_0\tau/2 \rightarrow -\phi$ acquired by each spin before the pulse. After the pulse, a phase $+\phi$ is again acquired which then cancels out the previous phase, and the spins refocus at the same point on the Bloch sphere, creating a "spin echo" or "Hahn echo" [Hah50]. Most pulsed ESR signals are acquired by integrating the signal from this Hahn echo, which has the main benefit to be properly separated in time from the high power pulses that would otherwise obscure the signal. In fact, the Hahn echo sequence can be considered in many experiments as a black box, placed just after the desired sequence, to provide a measure of the Z magnetisation of the spin ensemble.

As illustrated in Figure 2.5, there are three common experiments used throughout this work:

1. *Rabi oscillations:* They are the signature of coherent control of quantum systems. By incrementing the duration of a pulse, the spins are rotated by increasingly larger angles, resulting in oscillations as they go back and forth between two eigenstates. The oscillations decay after some time: as the pulse length increases, its frequency bandwidth decreases, and if it becomes comparable or smaller than the ensemble inhomogeneous

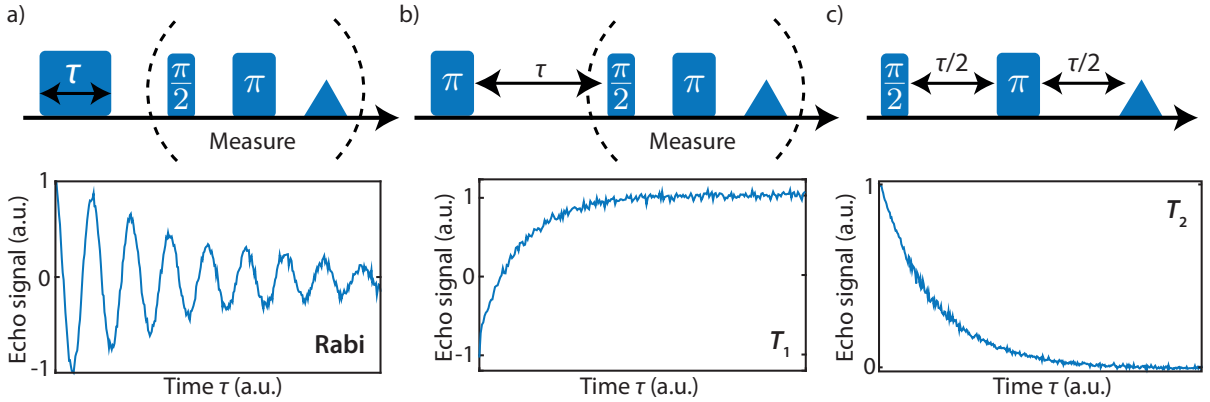


Figure 2.5: **Principal ESR sequences.** Sequences and corresponding typical experiment results. a) Rabi oscillations measurement sequence. b) Spin relaxation T_1 measurement sequence. c) Coherence T_2 measurement sequence.

broadening ($\delta\omega_0$), the rotation is tilted off its axis and becomes non-ideal (low fidelity). Other effects such as T_1 may also play a role in this decay. Rabi oscillations are also the usual sequence to run to calibrate the pulse power and duration to match a particular rotation angle.

2. T_1 *population relaxation:* An initial π pulse excites the spins out of thermal equilibrium. The Z magnetisation then returns to its steady-state value after a time T_1. Therefore, by waiting for increasing durations after the pulse and then measuring the magnetisation with a Hahn echo, the decay from population relaxation is measured. If the thermal echo amplitude is 1, this signal varies from -1 to 1. This is an "inversion-recovery" sequence.

3. T_2 *coherence decay:* In a Hahn echo sequence, for a duration of $\tau/2$ between the $\pi/2$ and π pulses, the echo appears symmetrically at $\tau/2$ after this last pulse. By sweeping τ, the echo decays due to the combined action of T_1 and T_2. Therefore T_1 is first measured with the previous sequence (and has no contribution from T_2 as it is in an eigenstate), and if possible, chosen to be much longer than T_2 to measure the decoherence separately with this sequence.

2.2.4 Typical ENDOR experiments

While ESR measures the state of an electron spin ensemble, the electron spins can interact with local nuclear spins, as is the case for donors in silicon. The coupled system now has more energy levels depending on the nuclear spin number I (as opposed to S for the electron spin). Considering a single nuclear spin-1/2 for simplicity, this two-spin system has 4 states as shown in Figure 2.6(a), with the electron spin state shown as single blue arrows and the nuclear spin as double red arrows. Above 1 K and at X-band, there is usually negligible amount of nuclear spin polarization due to its small frequency (< 1 GHz, radio-frequency (RF) regime) and thus the nuclear spin cannot be directly measured (or would require a doping concentration that exceeds the metal-insulator transition in silicon). It is possible, however, to transfer the electron spin polarization to the nuclear spin, manipulate it with a magnetic excitation at a different frequency (typically in the MHz), and then transfer back the nuclear spin state to the electron spin to be read out with a spin echo. This technique is called Electron Nuclear DOuble Resonance (ENDOR) [Mim65]. The secondary field for nuclear pulses is usually created with a simple coil, wrapped around the resonator, whose low-pass cutoff frequency from the inductance (with a 50 Ω load) can easily be above the low RF nuclear frequencies.

A typical ENDOR experiment can be divided in three parts:

1. *Polarization transfer:* First, an electron π pulse inverts the polarization between $|\downarrow\Uparrow\rangle$ and $|\uparrow\Uparrow\rangle$, or between $|\downarrow\Downarrow\rangle$ and $|\uparrow\Downarrow\rangle$, where the first state is for the electron spin and the second for the nuclear spin. This inversion must be selective on one of these two transitions (i.e. does not excite both), in order to increase the nuclear spin polarization as shown by the gray areas in Figure 2.6(b). This selectivity is allowed due to the coupling between the two spins, the electron spin frequency being thus dependent on the nuclear spin state (note that a selective π pulse is a therefore a CNOT gate in quantum information).

2. *NMR sequence:* Then, the nuclear spin can be controlled with RF pulses exactly like in conventional NMR. Due to the small nuclear gyromagnetic ratio compared to that of

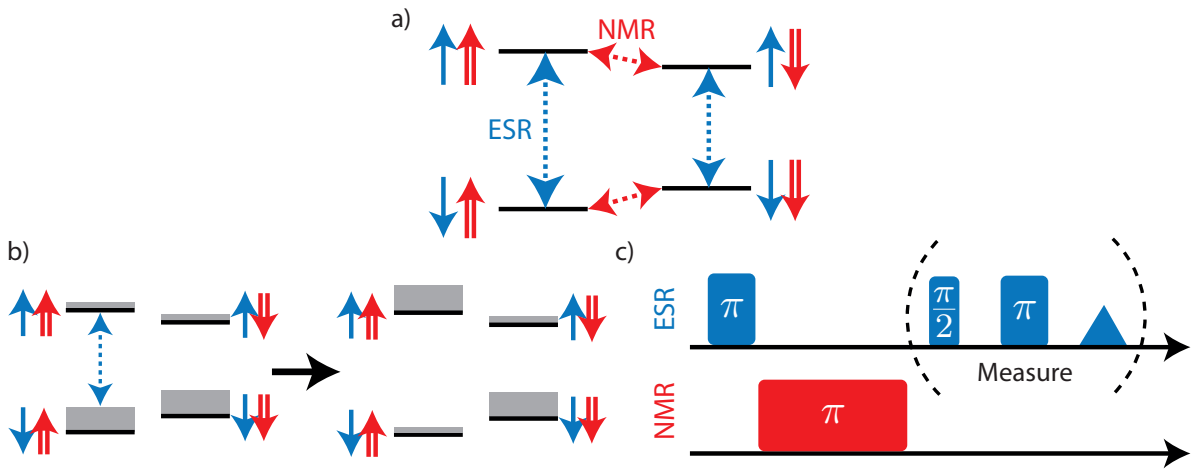


Figure 2.6: **ENDOR.** a) Diagram of energy levels for a spin-1/2 electron spin (blue) coupled to a spin-1/2 nuclear spin (red). The arrows on the side of each level represent the eigenstates. The ESR (MW) and NMR (RF) dashed arrows are the electron and nuclear spin allowed transitions. b) Polarization transfer using a selective ESR π pulse. The gray area represents the population for each state (exaggerated for visibility). c) Davies ENDOR measurement sequence to transfer electron polarization to nuclear polarization.

the electron, RF manipulation is much slower (μs instead of ns) resulting in pulses with narrow excitation bandwidth which can rarely excite both NMR transitions (red dashed arrows in Figure 2.6), thus they are nearly always selective. This assumes hyperfine couplings $> 10 - 100$ kHz, but given the selectivity requirements of the MW inversion pulse, this is normally the case for couplings accessible by ENDOR.

3. *Readout:* To read the nuclear spin state, an electron spin Hahn echo on one of the ESR transition is sufficient: for example, if the majority of the population is in $|\uparrow\Uparrow\rangle$, the electron spin state is just inverted and the echo signal measured on the $|\uparrow\Uparrow\rangle \leftrightarrow |\downarrow\Uparrow\rangle$ transition is -1 (inverted echo amplitude). If some RF pulses transfered the polarization to $|\uparrow\Downarrow\rangle$, there is no more population difference on the electron spin transition and the echo signal is 0.

Figure 2.6(c) with a single RF π pulse shows a Davies-ENDOR sequence [Dav74] where the RF frequency is swept until it is on resonance with the nuclear transition and the electron spin echo signal disappears (-1 to 0). This sequence is used to measure the nuclear gyromagnetic

ratio, as well as the strength of the coupling to the electron spin with higher precision than from an ESR spectrum. Indeed, the lower gyromagnetic ratio of a nuclear spin compared to that of an electron spin means that it is less coupled to the environment and its inhomogeneous linewidth is therefore smaller too, resulting in narrower frequency spectra.

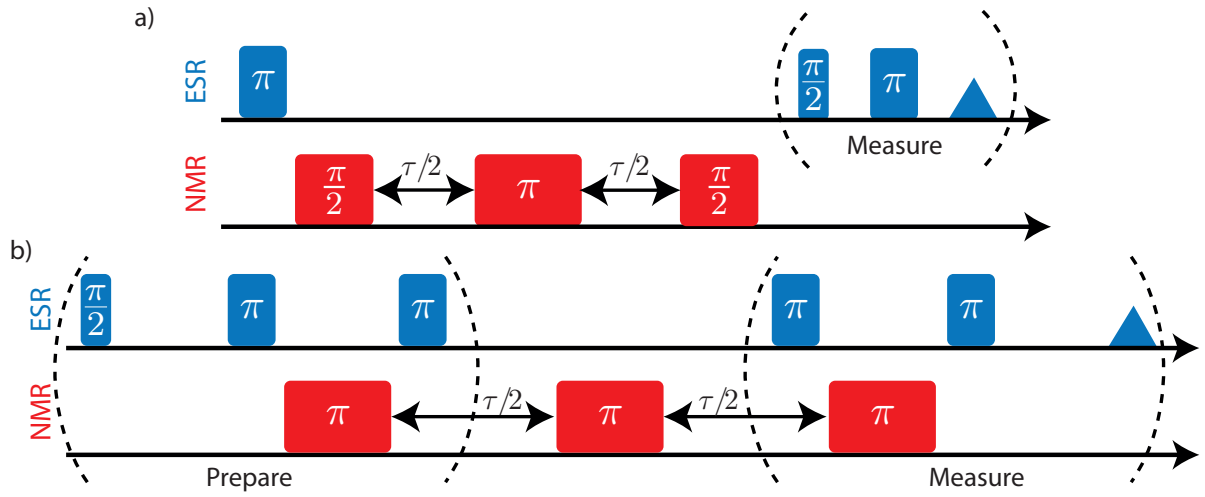


Figure 2.7: **Nuclear coherence measurements.** a) Nuclear spin coherence creation within a Davies ENDOR sequence. T_{2n} can be measured by sweeping τ. b) Alternative sequence using coherent state transfer between the electron and nuclear spins [MTB+08]. Pulses within blocks in bracket move all together when τ is changed.

Measuring the nuclear spin coherence time (T_{2n}) can be realized by replacing the RF π pulse in Figure 2.6(c) by an echo sequence on the nuclear transition, as shown in Figure 2.7(a). For small inter-pulse duration τ, the nuclear spins are still in phase and simply rotate by 2π ($= \pi/2 + \pi + \pi/2$). As τ is increased, the phase spreads out leading to a decrease in the signal after projection with a RF $\pi/2$ pulse. This sequence has some advantages and disadvantages. All the MW pulses can be fixed in time while sweeping τ which removes the risk of measuring in addition to T_{2n} the T_1 of the electron spin (T_{1e}); indeed, without the RF pulses this scheme is simply an inversion-recovery sequence. Another advantage is that the RF pulses which are quite long, in the order of μs and comparable with the electron spin coherence times, are only applied when the electron spin is in an eigenstate. If the electron spin was in a superposition, the signal would have decayed by the end of the sequence. One disadvantage is that only one quadrature, X or Y, can be measured at a time, depending on the final RF projection pulse, compared to ESR

where both X and Y projections are simultaneously observed. This can be an issue when the nuclear coherence times are long: the signal sometimes jumps between the two quadratures due to uncontrolled phase noise in the setup e.g. from the phase of the microwave source or from a drift in the magnetic field. This can only be corrected if both quadratures are known together and then taking the magnitude of the signal $\sqrt{\langle S_x \rangle^2 + \langle S_y \rangle^2}$. Finally, state transfer between the electron and nuclear spins might be desirable to fully use them as qubits, including transfer of a superposition which is not possible in this sequence.

A second sequence was described in [MTB$^+$08] and reproduced in Figure 2.7(b): it will be the preferred sequence in this work. A superposition is first created in the electron spin and then transfered to the nuclear spin with π pulses. After some delay τ and an RF π pulse in the middle to refocus the nuclear spin coherence, it is transfered back to the electron and measured as a spin echo. Hence, the remaining or recovered electron spin coherence is a measure of the loss in coherence for the nuclear spin. In this case, all states can be transfered back and forth between the two qubits compared to the previous sequence, though RF pulses must be short enough compared to the electron coherence time.

CHAPTER 3

Donors in silicon

Donors in silicon have been studied for their spin characteristics as early as 1954 [FYPM54, FYP$^+$54] and extensively by Feher *et al.* a few years later in a series of publications [Feh59a, FG59, WF61]. Further measurements were realized later on, in particular regarding the spin relaxation and coherence properties of the donors. In this Chapter, the spin model of donors in silicon is first introduced as a basis for the various studies presented later, followed by a summary of current knowledge on these properties.

3.1 Donor spin system

3.1.1 Donor spin Hamiltonian

Donors, as spin systems, are first defined by their (isotropic) Zeeman interactions, for both the electron and nuclear spins, with an externally applied static magnetic field. In addition, the electron and nuclear spins are coupled to one another by a hyperfine interaction due to the overlap of the electron wavefunction with the nucleus. This interaction is normally isotropic and

constant, though strain within the crystal or electric fields have a weak influence (see Chapter 6). The fact that the Hamiltonian is purely isotropic makes it ideal for large ensembles or scalable architectures as the system can be expected to always respond to the same excitations.

With **S** and **I** as the electron and nuclear spin operators, the Hamiltonian can be written as follows, in frequency units:

$$H = \gamma_e \mathbf{B_0}.\mathbf{S} - \gamma_n \mathbf{B_0}.\mathbf{I} + A\mathbf{S}.\mathbf{I} \tag{3.1}$$

where $\gamma_e = -g_e\mu_B$ is the electron gyromagnetic ratio (defined positive) with g_e the electron g-factor and $\mu_B =$ the Bohr magneton. $\mathbf{B_0}$ is the static magnetic field (vector). $\gamma_n = g_n\mu_n$ is the nuclear gyromagnetic ratio with g_n the nuclear g-factor and $\mu_n =$ the nuclear magneton. A is the hyperfine interaction between the electron and nuclear spins. For all the group V donors considered in this entire work, the electron spin is a spin-1/2. In Table 3.1, the nuclear spin number I, γ_e, γ_n and A are summarized for all the group V donors. The ^{31}P nuclear spin is 1/2, but for the other donors it can be as high as 9/2 (^{209}Bi): this departs from the typical theoretical quantum information system and into qudits (d-dimensional systems) which can provide more interesting challenges, in particular for quantum error correction [BdGS02, PMBV08]. In this work, most of the experiments were focused on the two cases of ^{31}P and ^{209}Bi.

	^{31}P	^{75}As	^{121}Sb	^{123}Sb	^{209}Bi
Nuclear spin number I	1/2	3/2	5/2	7/2	9/2
Electron gyromagnetic ratio γ_e (GHz/T)	27.972	27.970	27.973	27.973	27.997
Nuclear gyromagnetic ratio γ_n (MHz/T)	17.23	7.3	10.26	5.6	6.9
Hyperfine interaction A (MHz)	117.5	198.3	186.8	101.5	1475.2

Table 3.1: **Group V donors in silicon: spin properties.** The electron spin for the neutral donor is always a spin-1/2. [Feh59a, Sto05, WTG$^+$13]

With an isotropic Hamiltonian, it is possible to exactly solve the eigenstates and eigenenergies of the system, even for bismuth with its 20-dimensional Hilbert space. First of all, if we choose the direction of the magnetic field to be along Z for example, we can simplify Eq. 3.1

to:

$$H = B_0(\gamma_e S_z - \gamma_n I_z) + A\mathbf{S}.\mathbf{I} \tag{3.2}$$

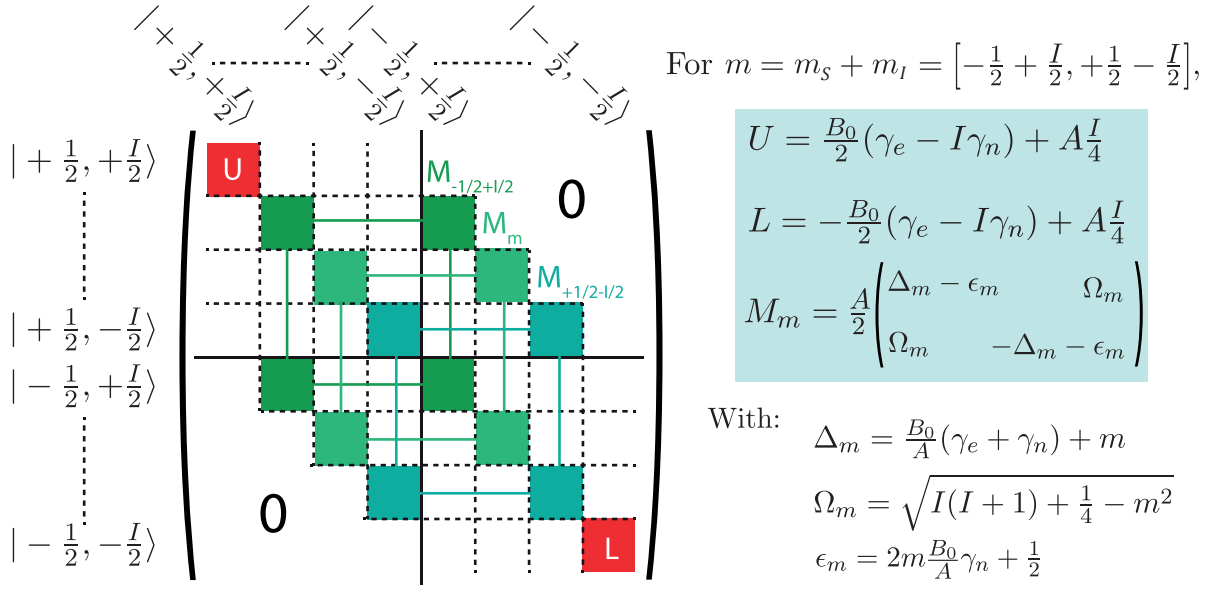


Figure 3.1: **Diagram of the donor spin Hamiltonian.** The Hilbert space can be separated into either 1 (L and U) or 2 (M_m, different shades of green) dimensional matrices. There are always 2 unmixed states and $4I$ mixed states. Non-coloured elements in the matrix are all zeros. I is the nuclear spin number and $m = m_S + m_I$ is the total spin number.

The hyperfine term $\mathbf{S}.\mathbf{I}$ is equal to $(S_x I_x + S_y I_y) + S_z I_z$. In the high field limit, the off-diagonal terms from the "flip-flop" component $S_x I_x + S_y I_y$ become negligible, i.e. they do not modify the eigenstates, and the Hamiltonian is diagonal. This simplification is called the Ising approximation and is commonly used at frequencies around 10 GHz (and $B_0 > 2000$ G) as the hyperfine value -apart from bismuth- is nearly two orders of magnitude smaller than the Zeeman interaction. We will see that it is in fact not always reasonable to use this approximation; indeed not all properties of the system reach their high-field values, even at these relatively high fields and frequencies. Such effects, arising from slight mixing between the electron and nuclear spins via the flip-flop terms, can play a major role on the donor spins' coherence times. The Ising approximation is not necessary however to solve the Hamiltonian; the off-diagonal terms from $S_x I_x + S_y I_y$ always couple a unique pair of eigenstates from the Hilbert space. This means the

Hamiltonian reduces to either 1 (unmixed, U and L) or 2 (mixed, M_m) dimensional subspaces which can be simply solved, as represented in Figure 3.1 (also see [MMNM12] for more details).

The unmixed states correspond to both electron and nuclear spins being both in their lowest or highest spin configuration, i.e. $|\phi_U\rangle = \left|m_S = +\frac{1}{2}, m_I = +\frac{I}{2}\right\rangle$ and $\left|\phi_L\right\rangle = |-\frac{1}{2}, -\frac{I}{2}\rangle$, where m_S and m_I are the electron and nuclear projected spin numbers, respectively. These states cannot evolve via flip-flop without breaking the conservation of the total spin number $m = m_S + m_I$, and thus are always eigenstates with eigenenergies U and L (Figure 3.1). The sub-matrices M_m, for $m = -\frac{1}{2} + \frac{I}{2} ... + \frac{1}{2} - \frac{I}{2}$, each give the following pairs of eigenstates $|\phi_m^{\pm}\rangle$ and eigenenergies $E_m^{\pm}$ in the new basis $\left|F = I \pm \frac{1}{2} \equiv \pm, m\right\rangle$:

$$\left|\phi_m^{\pm}\right\rangle = |\pm, m\rangle = \cos\left(\frac{\theta_m}{2}\right)\left|\pm\frac{1}{2}, m \mp \frac{1}{2}\right\rangle \pm \sin\left(\frac{\theta_m}{2}\right)\left|\mp\frac{1}{2}, m \pm \frac{1}{2}\right\rangle \tag{3.3}$$

$$E_m^{\pm} = \frac{A}{2}(-\varepsilon_m \pm R_m) \tag{3.4}$$

with

$$\cos(\theta_m) = \frac{\Delta_m}{R_m},\ \sin(\theta_m) = \frac{\Omega_m}{R_m},\ R_m = \sqrt{\Omega_m^2 + \Delta_m^2} \tag{3.5}$$

where Ω_m, Δ_m and ε_m are defined in Figure 3.1. The eigenenergies $E_m^{\pm}$ are plotted for each donors in Figure 3.2.

3.1.2 Transition properties

While the population of eigenstates can be measured directly in some systems such as with optical readout, magnetic resonance can only control and observe the difference in population across two states. For ESR, the donor spectrum can only be observed between states whose transition is allowed, i.e. the transition frequency is on resonance with the excitation and corresponds to a single spin flip ($|\Delta m| = 1$). This second condition is quantified by the transition

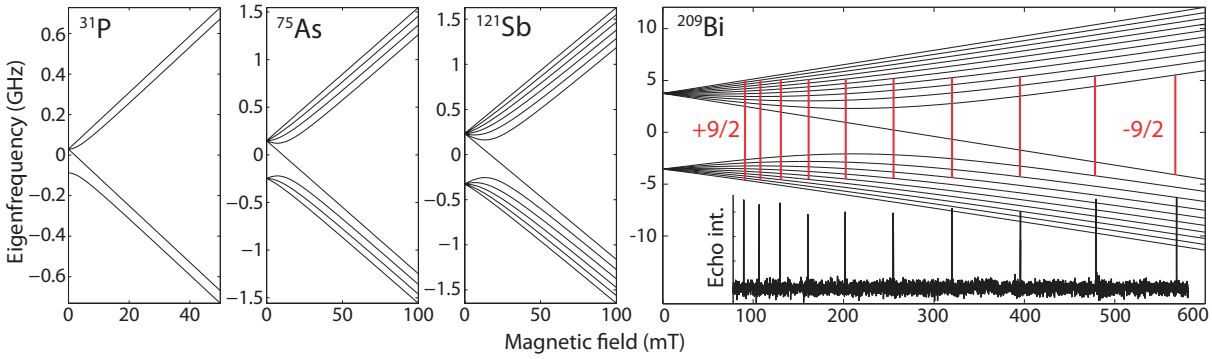


Figure 3.2: **Breit-Rabi diagrams of donors.** Eigenenergies of all four group V donors plotted as a function of magnetic field (in the limit $\gamma_n B_0 \ll A$). For ^{209}Bi, an experimental ESR spectrum taken at X-band (9.7 GHz) is shown with corresponding transitions (red) in the simulated eigenenergies. The transitions correspond from left to right to $m_S = +1/2 \leftrightarrow -1/2$ ($F = 5 \leftrightarrow 4$) and $m_I = +9/2$ to $-9/2$.

probability

$$\langle \psi_1 | \, \gamma_e S_x + \gamma_n I_x \, | \psi_2 \rangle \tag{3.6}$$

between these two states ($|\psi_{1,2}\rangle$). With $S = 1/2$, the total number of states is always $2(2I+1)$, corresponding to $2I+1$ allowed ESR transitions at high fields, i.e. one for each nuclear spin state, as shown for ^{209}Bi in Figure 3.2.

In Figure 3.3(b,c), the spectrum is zoomed in around one such transition: instead of having a single peak, two are now observed. As the electron and nuclear spins slightly mix together, transitions forbidden at high field become allowed. The high field allowed transitions correspond to $\Delta F \Delta m = +1$ (with $\theta_m \to 0$) and the forbidden transitions are $\Delta F \Delta m = -1$. For the latter, they are equivalent at high field to $|\Delta m_I| = 2$, (Figure 3.3(a)) i.e. are indeed forbidden. At the relatively high fields of X-band, these transitions are therefore quite weak as shown by the low-field peak in Figure 3.3(b). Also, because the transition probability is different from the allowed one, rotations require different amount of power or duration. Finally, the two transitions appear at very similar magnetic fields. Indeed, the difference in frequency between the

transition $|-,m\rangle \leftrightarrow |+,m-1\rangle$ and $|-,m-1\rangle \leftrightarrow |+,m\rangle$ is:

$$\begin{aligned}(E^+_{m-1}-E^-_m)-(E^+_m-E^-_{m-1}) &= \tfrac{A}{2}(-\varepsilon_{m-1}+R_{m-1}+\varepsilon_m+R_m+\varepsilon_m-R_m-\varepsilon_{m-1}-R_{m-1}) \\ &= 2B_0\gamma_n\end{aligned} \tag{3.7}$$

Hence, this behaviour is common to all fields and transitions, and below 1 T corresponds to a few MHz shift.

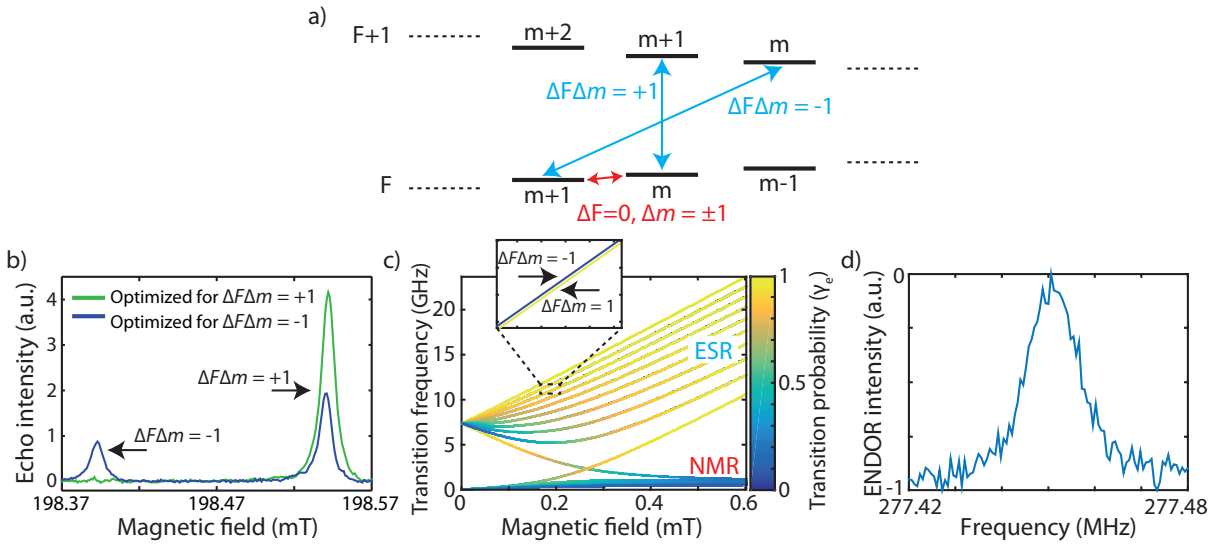


Figure 3.3: **ESR, NMR and forbidden transitions.** a) Energy diagram for an electron-nuclear spin system for $I > 1/2$. The blue arrows correspond to ESR transitions, allowed ($\Delta F\Delta m = +1$) and forbidden ($\Delta F\Delta m = -1$) at high magnetic fields. The red arrows are the typical NMR (ENDOR) transitions. b) Field sweep spectrum from a Hahn echo measurement in ^{209}Bi (concentration 2×10^{15} cm^{-3}) with power optimized to observe either the high field allowed or forbidden transitions. c) All allowed transitions in ^{209}Bi with (inset) a zoomed view of the ESR doublet of allowed and forbidden lines. The colormap gives the expectation value $2\langle\gamma_e S_x+\gamma_n I_x\rangle$ for each transition. d) Davies ENDOR spectrum measured by projection on one of the X-band ESR transition in ^{209}Bi($m_S=+1/2,\ m_I=+5/2\leftrightarrow+3/2$).

For NMR (in red in Figure 3.3(a)), there are no such "forbidden" transitions that may become allowed at low magnetic fields. On the other hand, the high field allowed transitions ($\Delta F=0, |\Delta m|=1$) only become faster to manipulate as they acquire an electronic spin component at low fields, up to a transition probability $\langle\gamma_e S_x+\gamma_n I_x\rangle=\frac{1}{4}\gamma_e$. An ENDOR spectrum of the $m_S=+1/2,\ m_I=+5/2\leftrightarrow+3/2$ NMR transition is shown in Figure 3.3(d).

The spin ensemble inhomogeneous linewidth is also an important property of the silicon sample; it is determined by the distribution of the free parameters $A, \gamma_e B_0, \gamma_n B_0$ of the Hamiltonian across the sample, indicating either the material purity for A, γ_e, γ_n or the homogeneity of the external magnet for B_0. Generally, $\gamma_n B_0$ is too small to contribute to the electron or nuclear spin linewidth compared to either A or $\gamma_e B_0$, and is therefore negligible. Changes in γ_e alone are also very small (see Chapter 6 for more details) and thus the linewidth is mostly due to shifts in the hyperfine ΔA or the local magnetic field ΔB_0. At high field, the NMR transitions are insensitive to $\gamma_e B_0$ and can provide a good estimate of ΔA. For example, Figure 3.3(d) gives the value $\Delta A = 60$ kHz [WST$^+$12]; such distribution in the hyperfine interaction strength is due to crystal defects and strain. ESR transition linewidths are dependent on both ΔB_0 and ΔA, however, $\gamma_e \Delta B_0$ tends to dominate and is between 0.1 and 12 MHz depending on the silicon isotopic purity (this includes in ΔB_0 the effect of the coupling with nuclear spins in the environment of the donor, see next Section). When electron-nuclear spin mixing is important, the sensitivity to change in A and B_0 starts to differ from the high field limit, hence the measured ESR or NMR linewidths might be different for a given distribution in both free parameters. In addition, spin coherence properties which are more related to temporal fluctuations in A or B_0 are also modified and going to mixed regimes can be very interesting (see Chapter 5).

3.2 Spin relaxation and decoherence

Donors in silicon have been particularly appreciated for their long coherence times. As we have seen, this is an essential requirement for quantum computing. Many other qubit systems have coherence times typically limited below the millisecond regime [BGY$^+$11, BFN$^+$11] even today, yet the coherence time for the electron spin of phosphorus was measured to be 0.5 ms as early as 1958 [GB58], and with a relaxation time T_{1e} known to be much longer. Since then, many studies have been realized to understand these properties, model the donor environment, and try to push these times further and further. There are three characteristic timescales of

particular relevance to donor-based spin qubits:

- *Relaxation T_{1e}:* In silicon, spins are coupled to phonons in the lattice, which provides at finite temperature a relaxation mechanism toward a steady-state population (Section 2.1.2). In addition, the electron spin coherence follows $T_{2e} \leq T_{1e}$ [TLAR03]. T_{1e} can also act as a source of dephasing for the donor nuclear spin via the hyperfine interaction resulting in $T_{2n} \leq 2T_{1e}$ [MTB$^+$08].

- *Electron spin coherence T_{2e}:* The electron spin coherence is typically due to magnetic fluctuations in the environment of the donor. The source of these fluctuations can be either simple (e.g. classical noise from a coil) or complex (interactions within a quantum bath of spins). The large gyromagnetic ratio of the electron makes it very susceptible to such noise. Electric fluctuations may also lead to decoherence via modulation of the hyperfine interaction (see Chapter 6).

- *Nuclear spin coherence T_{2n}:* The nuclear spin coherence can also be limited directly by magnetic fluctuations, however it is often the coupling with the electron spin that provides a pathway for decoherence. This can be due to either fluctuations in the hyperfine coupling with the electron spin or via spin mixing causing the nuclear spin states to obtain some S_x character (especially since even a tiny amount of mixing has a large effect due to $\gamma_e \gg \gamma_n$).

Note that there is no discussion here of the relaxation time of the nuclear spin T_{1n} as it is much longer ($>$ hours [FG59]) than any of these times and has negligible influence in any experiments considered in this thesis. The most likely relaxation mechanism for nuclear spin polarization is cross relaxation T_{1x} consisting of a simultaneous flip of both the electron and nuclear spins.

Electron spin relaxation T_{1e} does not usually vary between different silicon samples for a given donor and temperature, apart for large donor concentrations ($> 10^{16} - 10^{17}\text{cm}^{-3}$). Electron and nuclear spin coherences are on the other hand much more sensitive to the silicon crystal,

and in particular we must separate two very different cases:

- *natural silicon* $^{\text{nat}}$*Si:* in its natural abundance, silicon has three different isotopes: ^{28}Si at 92.2%, ^{29}Si at 4.7% and ^{30}Si at 3.1%. ^{28}Si and ^{30}Si are both spin 0, and therefore have no magnetic moment that can interact with the donor spin. ^{29}Si has however a nuclear spin 1/2: in the vicinity of a donor, these spins form a fluctuating magnetic "bath" which is often the strongest source of decoherence.

- *isotopically enriched 28-silicon* ^{28}*Si:* the silicon lattice can be grown from an enriched source of silicon with different content of isotopes. Typically, because ^{28}Si is naturally the most abundant and has no nuclear spin, it is interesting to further eliminate the other isotopes and reduce the strength of the ^{29}Si spin bath. Materials enriched down to 50-100 ppm of ^{29}Si can be made [IKU$^+$03, BFF$^+$09], however they remain rare.

In an ensemble, it is instructive to consider the properties of a single donor, called the "central spin", interacting with other spins in the environment (which could very well include other donors as well). This central spin then provides the model spin for various physical mechanisms, mainly decoherence, and the ensemble properties are mostly an average over all possible coupling strengths to, and configurations of, the environment. Possible correlations between these central spins are neglected as the complexity would be too great to model or intuitively understand.

3.2.1 Electron spin relaxation times T_{1e}

Population relaxation of donor electron spins in silicon happens by exchange of energy between the spin system and the lattice or phonon bath [Shr83]. This is known as the spin-lattice coupling. Phonons can interact with the donors by modulating their potential within the lattice and thus their eigenstates. This results in either mixing of the various conduction bands [WF61] and hence a g-factor modulation, or mixing with higher excited states which have a non-zero spin-orbit coupling (due to an anisotropic wavefunction) [Cas63, Cas67], and therefore fast spin

relaxation. As the phonon distribution depends directly on the temperature (T) of the lattice, T_{1e} follows various functions of T depending on the type of process involved. In addition, there may also be a dependence with respect to the spin transition frequency ω. There are three usual types of relaxation in silicon as illustrated in Figure 3.4(b):

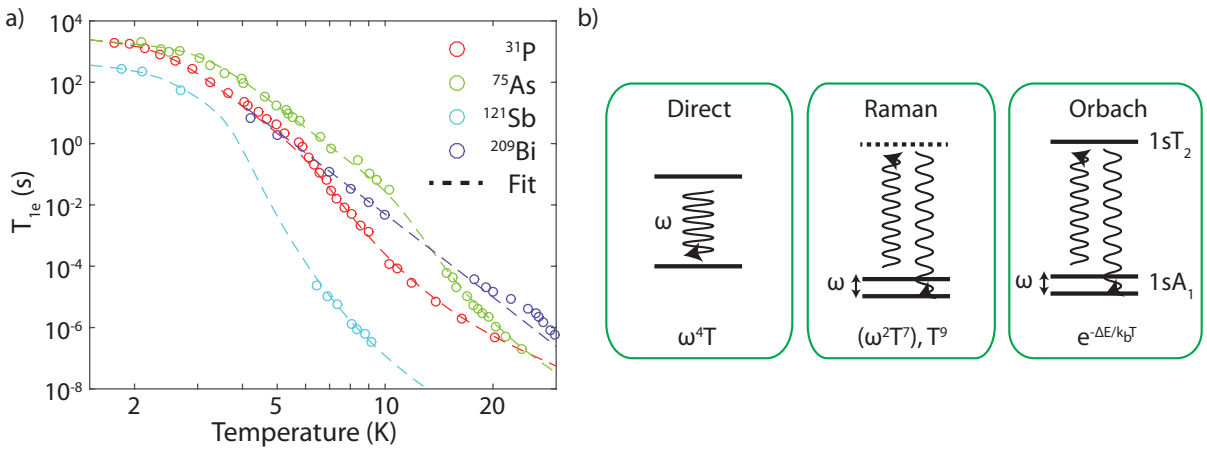


Figure 3.4: **Relaxation mechanisms.** (a) T_{1e} relaxation times for all group V donors in silicon taken from [Cas63] (around 0.33 T), apart for the low temperature ^{209}Bi [WST$^+$12]. Dashed lines are fits to the data according to Eq. 3.8. (b) Schematics of the three relaxation processes: direct, Raman and Orbach. The given relations show the typical dependence with respect to the spin frequency ω and the temperature T.

- *Direct/one phonon:* The direct process is a single-phonon absorption or emission when the frequency of the spin transition ω and of the phonon match. The relaxation is ascribed to both conduction band and excited state mixing (valley repopulation). The direct process follows a $\omega^4 T^{-1}$ dependence when $\hbar\omega \ll k_B T$, which is normally the case for ESR experiments. At temperatures below 4 K, this is the dominant process for all the donors.

- *Raman/two phonons:* Raman processes involve two-phonon transitions through an indirect energy level. This level is usually virtual and all phonon energies can thus contribute. This mechanism can be either $\omega^2 T^{-7}$ from anisotropic Zeeman interaction or T^{-9} from spin-orbit interaction, though the latter typically dominates (the exact power dependence is still subject to question and there are still contradicting results even in recent papers

[MWS$^+$10, WST$^+$12]). The Raman process contributes mostly at intermediate temperatures between 4 and 10 K.

- *Orbach/two phonons:* The Orbach process is also induced by two-phonon transitions but in resonance with a real energy level, usually the $1sT_2$ and to some extent the $1sE$ valley states. Contrary to the other two processes, it follows an exponential dependence with the temperature, which is simply the Boltzmann distribution $e^{-\Delta E/k_bT}$, where ΔE is the energy difference between the ground $1sA_1$ state and these excited valley states. It is also independent of the frequency ω. The Orbach process dominates at the higher temperatures (> 10 K) and depends strongly on the type of donor.

In Figure 3.4(a), T_{1e} measurements from [Cas63, WST$^+$12] are shown for the main donors, and then fitted with the above processes:

$$1/T_{1e} = C_D\omega^4 T + C_R T^9 + C_O e^{-\Delta E/k_bT} \tag{3.8}$$

where C_D, C_R and C_O are fitting coefficient for the direct, Raman and Orbach mechanisms respectively. The Raman T^{-7} power term is neglected here.

In a typical ESR experiment, the temperature is set to obtain a specific T_{1e} which must be within a certain range of values: long so that it has negligible impact on the spin dynamics during the experiment, in particular when measuring long coherence times, yet short so that the spins return promptly to thermal equilibrium in order to start another experiment (e.g. for averaging). Electron spin relaxation in silicon can be strongly enhanced on-demand by illuminating the sample with above-gap light (e.g. 1050 nm in most experiments here) [FG59], generating free electrons which can scatter with the donors, enhancing the electron spin relaxation T_{1e} via spin exchange.

There is a second possible effect of using light, though it was not used here: enhanced spin relaxation can lead to polarization of the spins beyond their thermal value. The most common mechanism for this "hyperpolarization" is the dynamical polarization of the nuclear spin

(e.g. the Overhauser effect) via electron-nuclear flip-flopping as the electron spin relaxation time becomes much faster [Feh59b]. This usually happens at high magnetic fields. More direct polarization mechanisms can be realized with illumination resonant with the donor bound-exciton transitions: the creation of bound-exciton is spin-selective and causes the donor to become ionized and recapture an electron with a random spin polarization, enabling pump experiments [YSK+06, SSS+10, SSY+11, LUR+15].

3.2.2 Electron spin coherence times T_{2e}

As explained above, the electron spin coherence time T_{2e} is always limited by the spin-lattice relaxation. For most donors, $T_{2e} = T_{1e}$ above ≈ 10 K and starts to diverge at lower temperature when T_{1e} is longer than 10 ms. The first experiments in silicon [GB58] were mostly realized in the low temperature regime, with relatively high donor concentration. In these conditions, the main limits to the coherence were due to either (illustrated in Figure 3.5):

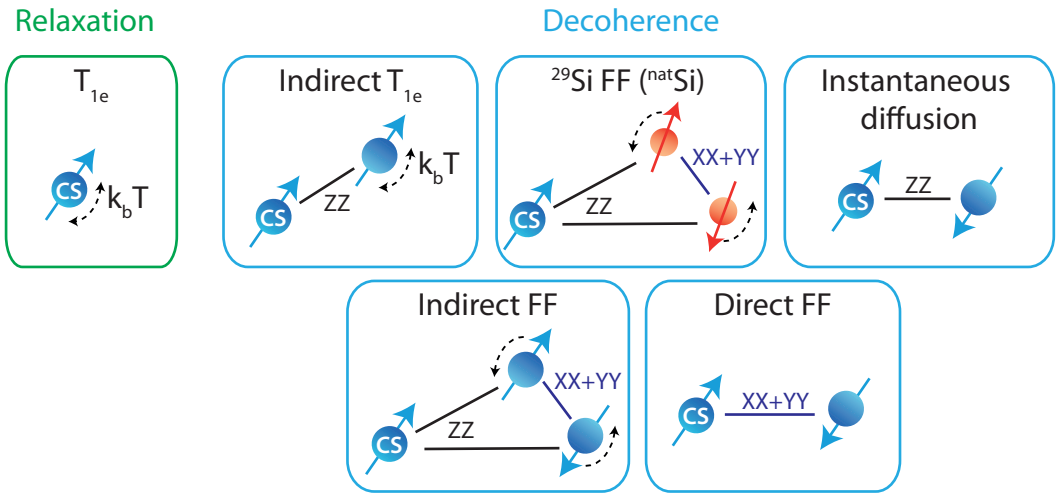


Figure 3.5: **Decoherence mechanisms.** Schematic of the various decoherence mechanisms for the electron spin. In a reading order, the spin-lattice relaxation T_{1e} of the central donor, T_{1e} of neighbour donors, flip-flop of ^{29}Si spin pairs in ^{nat}Si, instantaneous diffusion due to unrefocused ZZ interaction, flip-flop of neighbour donor pairs and finally flip-flop of the central donor with another neighbour donor.

- *^{29}Si bath:* In ^{nat}Si, the ^{29}Si nuclear spins create a fluctuating environment for the electron spin. The electron wavefunction spreads across a few lattice shells around the donor and

overlaps with the nuclear point-like wavefunctions of ^{29}Si nuclear spins, resulting in a hyperfine interaction. Because the electron and nuclear spins have very different frequencies (the ratio of gyromagnetic ratios is about $\approx 10^3 - 10^4$), it is mostly a ZZ Ising coupling between them, the flip-flops being suppressed. Because of the high concentration of ^{29}Si ($\approx 10^{21}\text{cm}^{-3}$), there is a large probability of finding pairs (and larger clusters) of ^{29}Si that are relatively close to one another, and therefore they can have a strong dipolar interaction (≈ 100 Hz). Because the pair of ^{29}Si spins should have similar frequencies, the flip-flopping part $XX + YY$ of their interaction allows for a slow exchange of their states over time. Through the hyperfine interaction, the donor electron spin therefore sees this as a frequency drift and eventually a dephasing: this is called spectral diffusion [KA62]. When not limited by T_{1e} and for donor concentrations below 10^{17}cm^{-3}, spectral diffusion from ^{29}Si is the limiting factor for electron spin decoherence (in fact also for the nuclear spin T_{2n}). Measured T_{2e} vary between 0.1 and 1 ms [AIIY04, ATT$^+$10, GWR$^+$10]. This depends on the donor species, as the Bohr radius varies between donors, and on the orientation of the silicon lattice with the external static magnetic field as it modifies the dipolar couplings between the nuclear pairs.

- *Instantaneous diffusion (ID):* Interestingly, isotopically purified ^{28}Si samples were already measured in the 1958 experiments [GB58], however the coherence time was enhanced by only a factor of two from the reduced ^{29}Si concentration. This was due to another effect as the samples had high donor concentration. Measurements of T_2 times are realized using a Hahn echo sequence where the inhomogeneous broadening T_2^* is refocused by a π-pulse (see Section 2.2.3). In the spin evolution, this corresponds to inverting the sign of any phase acquired by static Z couplings with the environment, i.e. $Z \to -Z$. However, donors are also coupled with the other donors in the ensemble via mainly the dipolar interaction (for concentrations $< 10^{16}\text{cm}^{-3}$). The random distribution of spins results in an inhomogeneous broadening from ZZ couplings between the donor spins. When a π-pulse is applied, all the spins on resonance with the microwave excitation are flipped

together: the interaction becomes effectively $(-Z)(-Z) = ZZ$ and hence there is no phase cancellation. This effect is called instantaneous diffusion (ID) and depends strictly on the donor concentration, i.e. the average dipolar interaction [SDR81, KI92, SJ01]. There is in fact a simple relation for T_2:

$$\frac{1}{T_{2e}^{ID}} = C(2\pi\gamma_e)^2 \frac{\pi}{9\sqrt{3}}\mu_0\hbar \tag{3.9}$$

where C is the concentration of spins on resonance with the pulse. With typical X-band ESR sensitivity, the lowest spin concentrations are about $C \approx 10^{13} - 10^{14}\text{cm}^{-3}$, giving T_{2e} around 10-100 ms [TLAR03, TTM$^+$11, WST$^+$12]. It should be remarked that ID is an ensemble limitation, as one can expect in single-spin devices that the measured spin is the only one being manipulated too (though ID might be relevant again for high qubit densities).

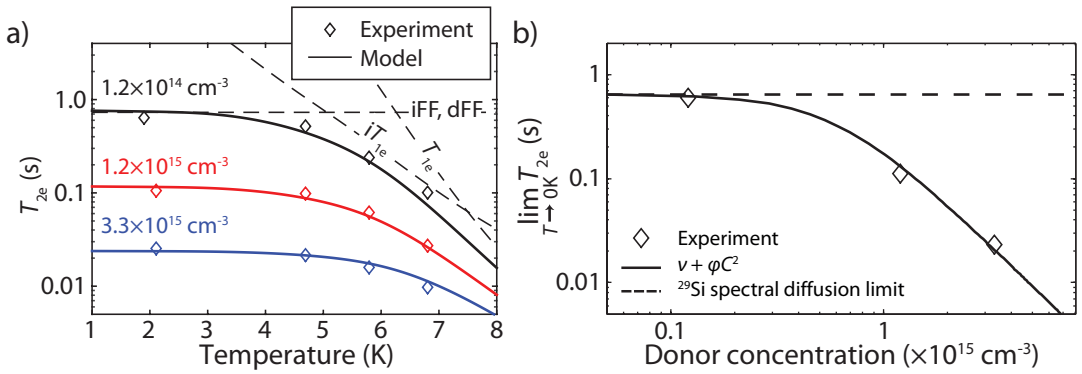


Figure 3.6: **Electron spin coherence beyond ID.** a) Extrapolated T_{2e} in ^{28}Si:^{31}P as a function of temperature and for various ^{31}P spin concentrations (reproduced from [TTM$^+$11]). The dashed lines are the different contributions to the decay times: indirect and direct flip-flop (iFF,dFF), indirect T_{1e} (iT_{1e}) and T_{1e}processes. b) Extrapolated T_{2e} in the low temperature limit as a function of donor concentration in ^{28}Si:^{31}P. With the best isotopically purified ^{28}Si samples, ^{29}Si spectral diffusion limits the electron coherence times to about ≈ 1 s.

The coherence limit from ID is in some way an upper bound for standard ensemble ESR experiments. There is one technique that can reduce this effect though it is not practically useful for quantum computation. All that is needed is to reduce the spin concentration to remove ID,

therefore one can try to simply refocus fewer spins in the ensemble to lower C. This can be achieved by reducing the angle of the refocusing pulse from π to $\rightarrow 0$, which can be seen instead as having statistically a proper π pulse but on fewer spins. Only the spins that are refocused still contribute to the signal, which is therefore reduced along with the effective concentration of on-resonance spins (hence this is more a characterization tool than a useful way of achieving long coherence times). The decay rate follows $1/T_{2e}^{ID} \times \sin^2(\theta/2)$, where θ is the angle of the refocusing pulse. In detailed experiments from Tyryshkin *et al.* [TLAR03, TTM$^+$11], this was used to probe the decoherence mechanisms beyond ID by extrapolating T_{2e} when $\theta \rightarrow 0$. In this limit, there are three of them:

- *Indirect T_{1e}:* As temperatures are lowered and T_{1e} diverges from T_{2e}, there is an intermediate regime where T_{1e} still affects the spin coherence but indirectly through neighbour spins. The relaxation of nearby spins corresponds to a fluctuating environment and phase shift for the central donor spin via ZZ couplings. This is similar to the effect of spectral diffusion from ^{29}Si spins, but the spin flip is due to the phonons instead. This process follows a $\sqrt{T}$ dependence. At even lower temperatures, any effects of T_{1e} finally disappear as shown in Figure 3.6(a) for ^{28}Si:^{31}P.

- *Indirect flip-flops (iFF):* Similar to ^{29}Si spectral diffusion, pairs (and more) of donor electron spins can also exchange their states (FF) and dephase the central spin via the ZZ coupling. This is independent of temperature and depends on the donor concentration. It can become slightly complex to analyze this mechanism for donors with large nuclear spin numbers: for a given pair of donors, the flip-flop rate depends on the given state of each donors. Transitions have to be allowed but this can vary with magnetic field near mixed regime [WST$^+$12].

- *Direct flip-flops (dFF):* Compared to all the other decoherence mechanisms, dFF is more akin to spin relaxation T_{1e}. Indeed, it comes from direct state exchange between the central spin and some other spin due to the $XX + YY$ part of the dipolar interaction. This is

thus a spin flip and not a frequency shift. In an ensemble, the total Z polarization is conserved between the pair, however, for a single spin measurement (where only the central spin matters), the spin flip would be indistinguishable from T_{1e}, though it is temperature independent.

At low temperature ($\lesssim 5$ K), iFF and dFF are the only remaining sources of decoherence (apart for ID). Both mechanisms originate from the dipolar interaction and are dependent on the donor concentration as shown in Figure 3.6(b) for ^{28}Si:^{31}P. In the limit of no ID, low temperature and low concentration, T_{2e} finally saturates around one second: this is due to the remaining ^{29}Si spins for samples with $[^{29}\text{Si}] = 50 - 100$ ppm. The isotopic enrichment compared to ^{nat}Si is a factor of 1000 and the increase in T_{2e} is similar: this was also confirmed in theory where a linear dependence with the ^{29}Si concentration was predicted [WCM$^+$10]. This dependence was calculated to be only valid down to a certain ^{29}Si isotopic fraction (as a function of donor concentration), as the coupling to the ^{29}Si spins ensure small energy detunings between the donors, hence suppressing partially donor flip-flop processes. Similar effects can be achieved by application of magnetic field gradients for example, and generally more isotopic purification is still desirable, though it becomes very difficult. Eventually however, the main issue remains mostly the concentration of donor spins. While efforts can be made to reduce it, for ensemble measurements this also reduces the signal intensity and is therefore not a realistic solution.

There are still some solutions: first, specialized pulse sequences called "dynamical decoupling" (see Section 4.2.1) can be made to extend the coherence times. Second, not all spins have the same sensitivity to their environment. For example, nuclear spins have a much smaller gyromagnetic ratio than the electron spin, resulting in longer coherence times though at the expense of slow control. Due to the interplay between the hyperfine and Zeeman interactions, the donor spin Hamiltonian also offers spin transitions that are nearly insensitive to magnetic fluctuations without any compromise on the manipulation speed (see Chapter 5).

3.2.3 Nuclear spin coherence times T_{2n}

In most cases, the nuclear spin of the donor is subject to the same decoherence mechanisms as the electron spin (Figure 3.5). However with the nuclear gyromagnetic ratio γ_n orders of magnitude lower than that of the electron, there are some differences. First, ID is practically negligible as the dependence on the gyromagnetic ratio is quadratic as given by Eq. 3.9. Then, dFF has also the same dependence as ID (both being from a dipolar interaction between nuclear spins). At low temperature, this only leaves the ^{29}Si FF and iFF of the electron spins. T_{2n} for low donor concentration has been measured in ^{28}Si with times from seconds to minutes (note that this is at a nuclear spin "clock transition", see Chapter 5) [MTB$^+$08, SST$^+$12]. Some measurements in ^{nat}Si are given in Section 4.3 and give a coherence time about one second.

As the low gyromagnetic ratio of the donor nuclear spin reduces sensitivity to all these magnetic-like interactions, this leaves place for electrical noise to become a limiting factor. Electric noise couples to a donor via its hyperfine interaction owing to modulation of the electron wavefunction. The intensity of such coupling is measured and discussed in Chapter 6: though it is generally negligible in bulk ensembles, apart from in configurations such as a layer of spins close to a surface, it is likely to become important in single spin devices. As mixing with the electron is also a result of the hyperfine interaction, this means that for the nuclear spin coherence the presence of the electron is indeed a major issue. It has been proposed and demonstrated in recent results [YSK$^+$06, SSS$^+$13, LSL$^+$14] that ionizing the donor, either electrically or optically, can increase T_{2n} up to hours. Once again, such long coherence times come at the expense of low manipulation speeds characteristic of nuclear spins.

The nuclear spin of the donor is not the only nuclear spin available as a qubit: the ^{29}Si that are mostly a problem for coherence are themselves possible resources for quantum processing (see Section 4.3). Such use of the quantum bath has been shown in the system of Nitrogen-Vacancy centers in diamond [WWZ$^+$14, TCvdS$^+$14].

3.2.4 Outlook

As the boundaries for the coherence times of donor spins in silicon, both electronic and nuclear, were being pushed further and further away, so did the understanding of the various decoherence mechanisms. The modeling of the many-body interactions involved in these processes has always been an important question in itself; the extremely large number of spins in the environment making this problem far from trivial. For this, ^{nat}Si presents a good study case as the ^{29}Si interactions within the bath can be modeled by only pairs or slightly more ^{29}Si, resulting in a complex but manageable system to explore. This is investigated in the following Chapter.

CHAPTER 4

Central spin - bath dynamics

Decoherence of a central spin in a solid-state environment is not only a critical issue for quantum information processes but also a good subject for understanding the foundation of quantum physics [PS00, Zur03]. A donor electron spin surrounded by a ^{29}Si spin bath in ^{nat}Si offers such a model: the donor electron wavefunction, and consequently the hyperfine interaction, is sufficiently large that it can couple to many of the ^{29}Si nuclear spins. There is therefore a constant influence of the donor "central spin" on the bath, and vice-versa, of the bath on the donor. Interactions within the bath are modified by this coupling, the bath evolution hence depends on the central spin, allowing the latter to withdraw information about the bath. Finally, this interaction enables control of the bath spins as well as state transfer with the electron spin, resulting in the addressable bath spins becoming a useful available resource for quantum information. These controllable qubits along with the donor can be then thought of as a well defined system, similar to a molecule. In this Chapter, I address these two subjects: first, understanding the spin bath and in particular the many-body interactions within it. In the second part, I propose the use of some of the bath spins as register qubits for quantum error correction.

4.1 ^{29}Si bath dynamics

In the central spin model, a donor interacts with the ^{29}Si spins via either the hyperfine interaction, which dominates at short-range (< 15 nm), or the dipolar coupling which dominates at long-range (> 15 nm). In addition, the nuclear-nuclear dipolar interaction connects the bath spins. The spin dynamics then arise from the interplay between these various couplings, making the basis of the donor-bath system in ^{nat}Si. The number of sites in the lattice that have non-negligible interactions is in the thousands and is a practically intractable problem without some approximations. Thankfully, numerical simulations have shown that most of the dynamics can be captured by the evolution of small clusters (two or slightly more) of ^{29}Si spins [WD06, WCCD12, BKM$^+$12]. In this Section, I use an intuitive analytical model to understand decoherence from pairs of nuclear spins followed by experimental comparisons on ^{31}P donors. At X-band magnetic fields (≈ 300 mT), the ^{31}P donor is, to a very good approximation, in the high field limit and can be reduced to its electron spin only when considering interactions with the bath.

4.1.1 ^{29}Si ENDOR spectrum for ^{31}P-donors

In order to simulate the effect of the bath, it first needs to be characterized, i.e. the interactions between the donor and bath spins must be determined, as well as the interactions between the spins of the bath itself. ^{29}Si spins are arranged randomly within the crystal lattice according to its abundance in natural silicon (Figure 4.1(a)). Close to the donor, this arrangement combined with the spread of the electron wavefunction gives rise to specific hyperfine couplings for each site. Exact couplings for spins very close to the donor can be directly measured using the ENDOR sequence shown in Figure 4.1(b). Hyperfine values between 100 kHz to the highest at 6 MHz are well separated and therefore distinguishable; an in-depth study can be found in [HM69] where the couplings are classified depending on their shell position from the donor. For weaker hyperfine couplings for which the ^{29}Si are far from the donor, the number of spins

with similar frequency increases drastically, resulting in frequency crowding and the couplings cannot be extracted. For those, simulation of the electronic wavefunction, using the Kohn-Luttinger model for example [Koh57, Feh59a, dSD03], can provide a good estimate of the hyperfine interactions. For a ^{29}Si at distance $\mathbf{r}$ from the donor, the hyperfine coupling A to the donor electron spin is:

$$A(\mathbf{r}) = K\left(F_1(\mathbf{r})\cos(k_0 x) + F_2(\mathbf{r})\cos(k_0 y) + F_3(\mathbf{r})\cos(k_0 z)\right) \tag{4.1}$$

$$\text{with } K = \frac{4}{9}\eta\mu_0 h\gamma_e\gamma_{^{29}Si} \tag{4.2}$$

$$\text{and } F_{\{1,2,3\}}(\mathbf{r}) = \frac{\exp\left(-\sqrt{\frac{\{x,y,z\}^2}{(nb)^2} + \frac{\{y,z,x\}^2+\{z,x,y\}^2}{(na)^2}}\right)}{\sqrt{\pi(na)^2(nb)}} \tag{4.3}$$

where $\{x,y,z\}$ are the Cartesian coordinates of the ^{29}Si, $k_0 = 0.85\frac{2\pi}{a_0}$ with $a_0 = 5.43$ Å the silicon lattice constant, $\eta = 186$ is the charge density on each atomic site, $\gamma_{^{29}Si} = 8.46$ MHz/T is the ^{29}Si gyromagnetic ratio, a and b are characteristic length for hydrogenic impurities with $a = 25.09$ Å and $b = 14.43$ Å, and finally $n = \sqrt{0.029/E_{\text{ion}}}$ is a correction for longer distances with the ratio of the effective mass and observed binding energies (e.g. $E_{\text{ion}} = 0.044$ eV for ^{31}P). Using this equation, the hyperfine interaction is shown for the $x-y$ plane in Figure 4.1(c). The oscillating character of the interaction is due to valley interferences. Closer to the donor (2–3 lattice constants), this model is not very precise due to intervalley coupling induced by the donor potential; it can sometimes still be used as discrepancies tend to be smoothed out in ensemble measurements where all the different configurations and positions of nuclear spins, at both short and long distances, are naturally averaged. Finally, at longer distances (> 15 nm), the dipolar interaction between the donor electron and the ^{29}Si spins must also be taken into account (though it goes as $1/r^3$, the symmetry of the electron wavefunction cancels the dipolar coupling when a spin is too close to the donor nucleus) [Feh59a].

For the group V donors in silicon, the electron wavefunction has tetrahedral symmetry resulting in equivalent ^{29}Si sites with identical hyperfine coupling. Such symmetry is partially reduced by the anisotropic component of the hyperfine interaction, depending on the relative

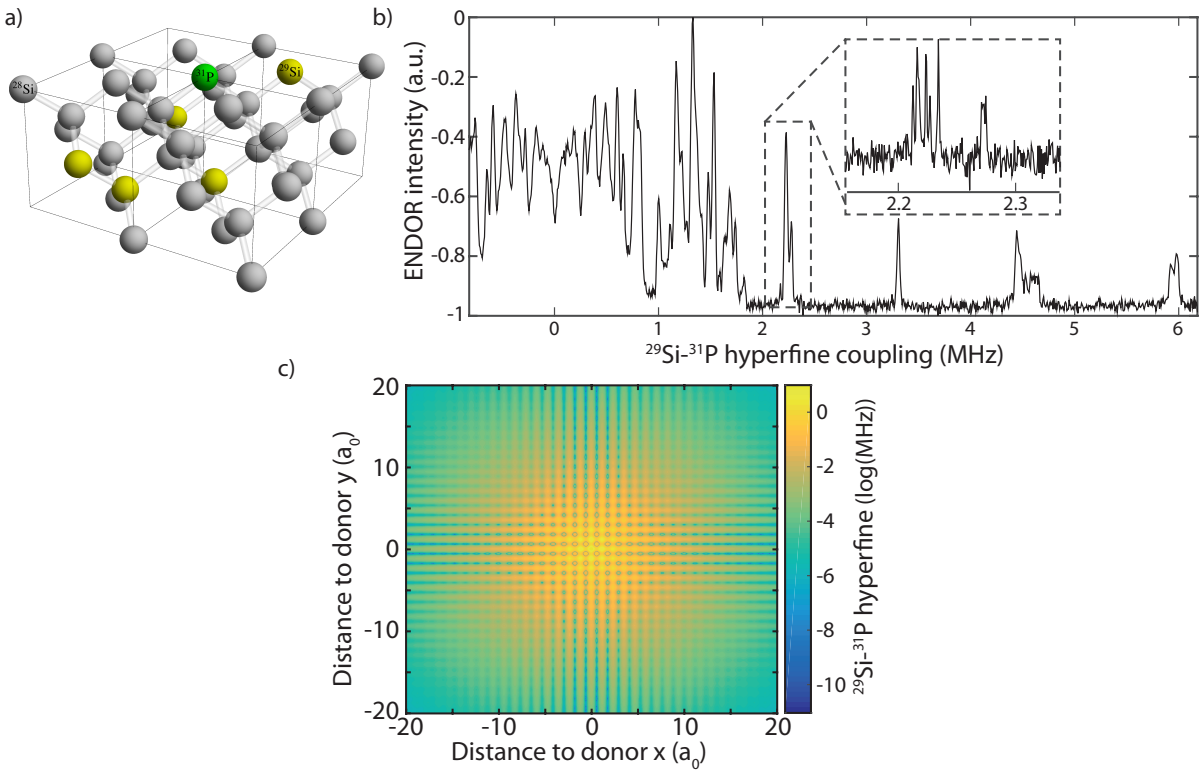


Figure 4.1: **ENDOR spectrum of ^{29}Si in ^{nat}Si:^{31}P** a) Illustration of a silicon lattice with a random arrangement of ^{29}Si spins (yellow) around the donor (green). b) Davies ENDOR spectrum renormalized as a function of the hyperfine interaction with the donor electron spin, considering a ^{29}Si Larmor frequency of 2.91 MHz ($B_0 = 0.3443$ T). In inset, a spectrum around 2 MHz was taken with longer RF pulses (1.6 ms compared to 50 μs previously) for better resolution: the many additional peaks are due to the anisotropic hyperfine/dipolar terms between the donor and ^{29}Si at specific sites. A recovery (or so-called "tidy") pulse was used in the Davies ENDOR sequence [TMAL06]. c) Hyperfine interactions simulated using the Kohn-Luttinger wavefunction for a ^{31}P donor (colorbar in logarithmic scale such that 0 corresponds to 1 MHz). The 2D map is given for distances $(x, y, z = 0)$ from the donor.

orientation of the external magnetic field and the donor-nuclear site distance. In the inset of Figure 4.1(b), one line can be seen to split into many smaller ones from this anisotropy. Such considerations can become important for understanding the bath evolution as any detuning between ^{29}Si due to the donor modifies the nuclear pair flip-flop (FF) process.

4.1.2 Bath modeling: pseudo-spin picture

There are many ways to model the decoherence of a central spin under the influence of a spin bath. For donors in ^{nat}Si, the bath has been treated as a source of classical noise [MMNM12]

or a quantum environment [WD06, SYS07, WCM+10], or even with mixed solutions [YLS06]. Here, we consider the quantum case where the bath is reduced to only two nuclear spins, and include all the dominant interactions within this pair and with the donor. We will see later how decoherence in the full spin ensemble with many configurations of nuclear spins can be modeled, but most of the physics can be first understood with this simple picture.

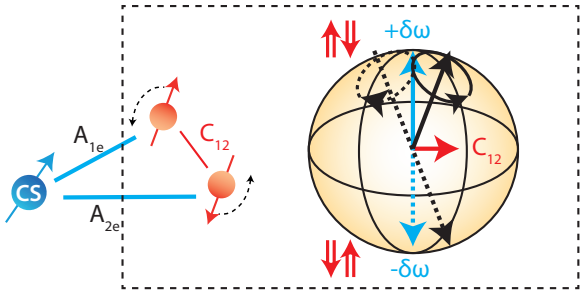


Figure 4.2: **Pseudo-spin model.** A flip-flopping spin pair within the bath, coupled to a central spin (CS), can be modeled as a simple pseudo-spin 1/2 whose evolution (circles with arrow) depends on the central spin state. Filled and dashed arrows correspond to the effective rotations for two opposite central spin states.

The decay in coherence of the central spin can be related to its entanglement with the bath. A measurement of T_2 begins by applying a $\pi/2$ pulse to produce the initial state

$$|\psi(t=0)\rangle = \frac{1}{\sqrt{2}}(|+\rangle + |-\rangle) \otimes |\mathscr{B}(0)\rangle \tag{4.4}$$

where $|+\rangle$ and $|-\rangle$ are a pair of eigenstates of the central spin alone and $|\mathscr{B}(0)\rangle$ is the initial state of the bath. We consider only the pure dephasing case with a ZZ interaction between the central spin and the bath. This is usually valid as the transition frequency of the central spin is much larger than the strength of the FF coupling with the bath. After a finite time delay t, and in the central spin rotating frame, the state evolves into the entangled state:

$$|\psi(t\neq 0)\rangle = \frac{1}{\sqrt{2}}(|+\rangle \otimes |\mathscr{B}_+(t)\rangle + |-\rangle \otimes |\mathscr{B}_-(t)\rangle) \tag{4.5}$$

where $|\mathscr{B}_\pm(t)\rangle$ is the bath state having evolved while the central spin is in the $|\pm\rangle$ states. Dephasing $\mathscr{L}(t)$ is calculated as the expectation value of the in-plane magnitude component of the

central spin, i.e.:

$$\mathscr{L}(t) = |\langle\psi(t)|S_{x,y}|\psi(t)\rangle| \propto |\langle\mathscr{B}_+(t)|\mathscr{B}_-(t)\rangle| \tag{4.6}$$

Hence $|\mathscr{B}_\pm(t)\rangle$ must be calculated to estimate the decoherence. The bath considered here is a pair of nuclear spins (1,2), and for practicality, the central spin is the donor electron spin (e), however the derivations can easily be extended to other systems. The Hamiltonian of the three-spin system is:

$$H = \omega_e S_z + \omega_1 I_{1z} + \omega_2 I_{2z} + \qquad (\leftarrow \text{Zeeman}) \tag{4.7}$$

$$S_z\left[A_{e1}I_{1z} + A_{e2}I_{2z}\right] + \qquad (\leftarrow \text{Hyperfine}) \tag{4.8}$$

$$C_{12}\left(2I_{1z}I_{2z} - \left(I_{1x}I_{2x} + I_{1y}I_{2y}\right)\right) + \qquad (\leftarrow \text{Dipolar}) \tag{4.9}$$

$$S_z\frac{A_{e1}A_{e2}}{\omega_e}\left(I_{1x}I_{2x} + I_{1y}I_{2y}\right) \qquad (\leftarrow \text{Hyperfine}-\text{mediated}) \tag{4.10}$$

where S is the donor electron spin operator, I_1 and I_2 are the nuclear spin operators. Only the Z component of the hyperfine interactions $A_{e1,e2}$ is included here as the frequencies ω_e and $\omega_{1,2}$ are too different too allow for flip-flopping. C_{12} is the dipolar interaction between the ^{29}Si nuclear spin pair. Finally the last term in the Hamiltonian is the hyperfine-mediated nuclear spin interaction; it is a second order correction due to the simultaneous FF of $\mathbf{S}.\mathbf{I_1}$ and $\mathbf{S}.\mathbf{I_2}$ which preserves both the energy and the total spin number. Therefore, a Hamiltonian for the nuclear spin pair can be isolated, but depending on the electron spin state $|\pm\rangle$:

$$H^{\pm}_{^{29}Si} = \frac{1}{2}\begin{pmatrix} \delta\varepsilon_\pm + C_{12} & 0 & 0 & 0 \\ 0 & \delta\omega_\pm - C_{12} & \Omega_\pm & 0 \\ 0 & \Omega_\pm & -\delta\omega_\pm - C_{12} & 0 \\ 0 & 0 & 0 & -\delta\varepsilon_\pm + C_{12} \end{pmatrix} \tag{4.11}$$

where $\delta\varepsilon_\pm = \omega_1 + \omega_2 \pm \frac{1}{2}(A_{e1} + A_{e2})$, $\delta\omega_\pm = \omega_1 - \omega_2 \pm \frac{\Delta A}{2}$ with $\Delta A = A_{e1} - A_{e2}$ and $\Omega_\pm = C_{12} \pm \frac{1}{2}\frac{A_{e1}A_{e2}}{\omega_e}$. In nearly all cases, the magnetic field is considered homogeneous in the bath and

$\omega_1 = \omega_2$. The first and last diagonal terms of the matrix correspond to the nuclear configurations $|\Uparrow\Uparrow\rangle$ and $|\Downarrow\Downarrow\rangle$; they are eigenstates and therefore do not evolve and cannot lead to entanglement (and thus central spin decoherence). Hence, only the states $|\Uparrow\Downarrow\rangle$ and $|\Downarrow\Uparrow\rangle$ with the ability to FF matter and the Hamiltonian can further be reduced to:

$$H_B^{\pm} = \frac{1}{2}\begin{pmatrix} \delta\omega_{\pm} & \Omega_{\pm} \\ \Omega_{\pm} & -\delta\omega_{\pm} \end{pmatrix} \tag{4.12}$$

Note that the C_{12} terms were removed as they correspond to an identity component in $H_B^{\pm}$ and therefore do not contribute to the evolution. This two-level system is a so-called "pseudo-spin" [YLS06, ZWL11] that represents the bath, as illustrated in Figure 4.2. Its Hamiltonian is simply $H_B^{\pm} = \delta\omega_{\pm} I_z + \Omega_{\pm} I_x$, where I is the pseudo-spin operator. The bath evolution (Eq. 4.5) and dephasing (Eq. 4.6) can be analytically calculated:

$$\mathscr{B}_{\pm}(t) = e^{-iH_B^{\pm}t}\mathscr{B}(t=0) \Rightarrow \mathscr{L}(t) \propto |e^{-iH_B^{+}t}e^{+iH_B^{-}t}| \tag{4.13}$$

This is only considering the evolution of the central spin directly after a $\pi/2$ pulse, but for a Hahn echo the evolution operators $e^{-iH_B^{\pm}t}$ become $e^{-iH_B^{\pm}t/2}e^{-iH_B^{\mp}t/2}$, i.e. the π pulse flips the evolution. Looking at Figure 4.2, decoherence of the central spin becomes simply the bifurcation from some initial state of the bath pseudo-spin to two separate states having evolved under the influence of opposite central spin states. To understand under what condition the bath evolves, the evolution operator can be derived using Eq. 2.12:

$$e^{-iH_B^{\pm}t} = \cos(\omega_{\pm}t)\mathbb{1} - 2i \times \sin(\omega_{\pm}t)[\cos(\theta_{\pm})I_z + \sin(\theta_{\pm})I_x] \tag{4.14}$$

where $\omega_{\pm} = \frac{1}{2}\sqrt{\Omega_{\pm}^2 + \delta\omega_{\pm}^2}$ is the precession rate and $\theta_{\pm}$ is the angle between the Z axis and the rotation axis of the pseudo-spin such that $\cos(\theta_{\pm}) = \frac{\delta\omega_{\pm}}{2\omega_{\pm}}, \sin(\theta_{\pm}) = \frac{\Omega_{\pm}}{2\omega_{\pm}}$. After some trigono-

metric calculations, this gives:

$$\mathscr{L}(2t) \propto |e^{-iH_B^+ t} e^{-iH_B^- t} e^{+iH_B^+ t} e^{+iH_B^- t}| = |1-2\alpha(\alpha+i\beta)| = \sqrt{1-(2\alpha)^2(1-\alpha^2-\beta^2)} \quad (4.15)$$

where $\alpha = \sin(\omega_+ t)\sin(\omega_- t)\sin(\theta_+ - \theta_-)$ and $\beta = \sin(\omega_- t)\cos(\omega_+ t)\sin(\theta_-) + \cos(\omega_- t)$ $\sin(\omega_+ t)\sin(\theta_+)$. The most important term of Eq. 4.15 is then $\alpha \propto \sin(\theta_+ - \theta_-)$ which represents the difference in precession axis. The larger it is, the faster $\mathscr{L}(t)$ diverges from 1 and the spins are entangled. Expressing α in term of $\omega_\pm$ is usually not very practical as they often have similar values and the product $\sin(\omega_+ t)\sin(\omega_- t)$ cannot easily be approximated. A better approach is to look at the average $\omega_\Sigma = \frac{\omega_+ + \omega_-}{2}$ and deviation $\omega_\Delta = \frac{\omega_+ - \omega_-}{2}$ in precession rates. In this case, Eq. 4.15 becomes:

$$\alpha = \frac{1}{4}\frac{\delta\omega_+\Omega_- - \delta\omega_-\Omega_+}{\omega_\Sigma^2 - \omega_\Delta^2}\left(\sin^2(\omega_\Sigma t) - \sin^2(\omega_\Delta t)\right) \quad (4.16)$$

ω_Δ is often very small, resulting in little evolution within T_2, and hence can be neglected, leaving only the fast oscillations at the ω_Σ frequency. However, ω_Σ cannot be too large either, otherwise the amplitude simultaneously diminishes. Also, for a large number of pairs with strong ω_Σ values, the distribution in ω_Σ averages out the time-dependence of the sinusoidal oscillation. Overall, there is in effect a filtering behaviour of the central spin regarding the bath frequency, and only a few pairs can be detrimental to the coherence. The amplitude coefficient in front of the sine is typically very small which allows for an expansion of the decay $\mathscr{L}(t)$ in α:

$$\mathscr{L}(2t) \approx 1 - 2\alpha^2 \approx e^{-2\alpha^2} \approx \exp\left(-(2t/T_2)^s\right) \quad (4.17)$$

where s is a stretch factor which depends on the relationship of α as a function of time t. The obtained decay time T_2 is only for a single spin pair; to properly find the coherence of the central spin in an ensemble with a large bath, this decay has to be modified and averaged following the cluster correlation expansion (CCE).

4.1.3 Bath modeling: Cluster Correlation Expansion (CCE)

The pseudo-spin gives a good representation of the bath, but only for a specific pair of ^{29}Si nuclear spins with specific couplings corresponding to specific sites in the lattice. To simulate the decay of the ensemble, the dephasing of Eq. 4.13 must be "averaged" following a particular order given by the theory of Cluster Correlation Expansion (CCE) [WD06, YL09a, YL09b]:

1. *Intra-cluster size averaging:* Around the donor there are many more nuclear spins than just two. In the simulation, a population of nuclear spins must be created randomly throughout the lattice. Compared to the lattice constant, the real sample is basically infinitely large and so must be truncated to avoid long computations. The lattice is thus limited around a certain radius around the donor, determined by coupling strength of the outer spins compared to the final coherence time. This is adjusted partially from trial and error to get convergence on the simulated decays. Once all the nuclear spins are set, the dephasing from every possible spin pair must be considered. To add them all together, the evolutions of the pairs are considered independent i.e. one must take the **product** of the dephasings: $\mathscr{L}(t) = \prod_i \mathscr{L}_i(t)$, where i is the index for a spin pair.

2. *Inter-cluster size averaging:* The exact central spin decoherence must take into account not only spin pairs of the bath but clusters of spins of all sizes (2,3, etc.). While only clusters of two spins are considered here, the total decay should be the **sum** of the decays from increasing cluster sizes (with some additional corrections to avoid over counting of clusters [YL09a]).

3. *Configuration averaging:* Finally, the measurement in the ensemble involves many donors, each with their own local configuration of ^{29}Si spins. Therefore, the last averaging is a **sum** over many realizations of the previous decays for random configurations of the nuclear bath. In addition, if pairs of ^{29}Si spins do not have opposite states, they cannot evolve in time from FF. Apart for very low temperatures and very high fields, the ^{29}Si pair always starts in a completely mixed state, i.e. with equal probability in the $|\Uparrow\Uparrow\rangle$,

$|\Uparrow\Downarrow\rangle$, $|\Downarrow\Uparrow\rangle$ or $|\Downarrow\Downarrow\rangle$ state. For the decay, this means only half of the states participate.

4.2 Electron spin decoherence in ^{nat}Si:^{31}P

In the previous Section, I presented a formalism for an intuitive understanding of the bath dynamics as an ensemble of independent pseudo-spins. Here, I turn toward experimental measurements of the electron spin coherence T_{2e} in ^{nat}Si, for the particular case of ^{31}P. Those measurements are indeed well known [GB58], giving coherence times about 0.3–0.5 ms limited by the coupling to the ^{29}Si bath. As mentioned previously, isotopic purification is one solution to reduce the effect of this nuclear spin environment. A good analogy for this kind of material improvement is to think of it as hardware replacement. By analogy, there often exists a complementary "software" solution, which for our quantum systems consists of spin manipulation via resonant pulses. They can control the evolution of the central spin qubit, and more importantly, can perturb the evolution arising from its interactions with the environment.

The most basic pulse solution to lengthen the electron spin coherence time is the Hahn echo sequence which refocuses static variations in the electron spin frequency throughout the ensemble, e.g. due to the hyperfine interaction with the many ^{29}Si. The refocusing π pulse in the sequence increases the coherence time from T_2^* to the much longer T_2. The coherence time can be further extended by adding more pulses in the sequence in order to also eliminate temporal fluctuations: this is called "dynamical decoupling (DD)". Here, I present results using this technique, first as a way to increase T_{2e}, then as a probe for studying the dynamics within the bath.

4.2.1 Dynamical decoupling (DD)

Dynamical decoupling (DD) describes a broad family of quantum control techniques, usually using pulses, that decouple a qubit from its environment [VL98, VKL99]. It is a vast topic in itself, both for finding optimal pulse sequences [Uhr07, WFL10] and for its various applications.

A common type of DD is the application of repeated inversion (π) pulses which can refocus pure dephasing Z interactions, the main source of decoherence in quantum systems. This was used extensively in NMR [LMY$^+$05, AAPS10], quantum dots [BFN$^+$11], NV centers [dLWR$^+$10] and more recently in silicon [MDL$^+$14].

There are multiple approaches to understanding DD and each of them provide different interpretations and applications. These approaches can be divided into two categories: classical and quantum, as illustrated in Figure 4.3(a,b) and (c,d) respectively. A classical dephasing noise has the usual form $H_I = \gamma B(t) S_z$, and results in a phase $\theta = \gamma \int_0^t B(t')dt'$ acquired by a qubit in a superposition such that $|\phi\rangle = \frac{1}{\sqrt{2}}(|0\rangle + e^{-i\theta}|1\rangle)$ (neglecting any global phase). When a π-pulse is applied, the phase is reversed $\theta \to -\theta$, and for N pulses, this leads to a total phase $|\theta| = |\gamma \sum_{n=1}^{N+1} (-1)^n \int_{t_{n-1}}^{t^n} B(t')dt'|$, where $[t_{n-1}\ t_n]$ is the interval between pulses. In Figure 4.3(a), an oscillating noise $B(t)$, in black, gives rise to some acquired phase depending on N. As N is increased, the time interval between pulses is reduced; the noisy field amplitude $B(t)$ has less time to change and becomes nearly constant between pulses, the corresponding acquired phase is still inverted every pulse, hence the noise effect on the qubit evolution is eventually fully canceled. In the time domain, this decomposition of the phase can be used to measure the dynamical evolution of the noise [CMYC14]. In the frequency domain, DD corresponds to a bandpass filter around a frequency determined by the spacings between the pulses. For a total sequence time τ, this frequency is equal to $\frac{N}{2\tau}$, and the width of the filter narrows with the number of pulses (Figure 4.3(b)) [BUV$^+$09, BGY$^+$11]. This filtering process can be understood 1) at lower frequency by the decomposition process explained in the time domain, 2) at the peak frequency by the fact that a π pulse at half the period of an oscillation reverses the sign at the moment where the noise also changes sign, therefore positively adding the phase, and 3) at high frequency, the spin cannot evolve fast enough compared to the noise and the phase has simply no time to be acquired. This filtering process can be used to sense specific couplings in the bath and has been compared to a quantum version of a lock-in amplifier [KAG$^+$11, ZHH$^+$11, SSP$^+$13]. This application could also be used in $^{\text{nat}}$Si to sense and control

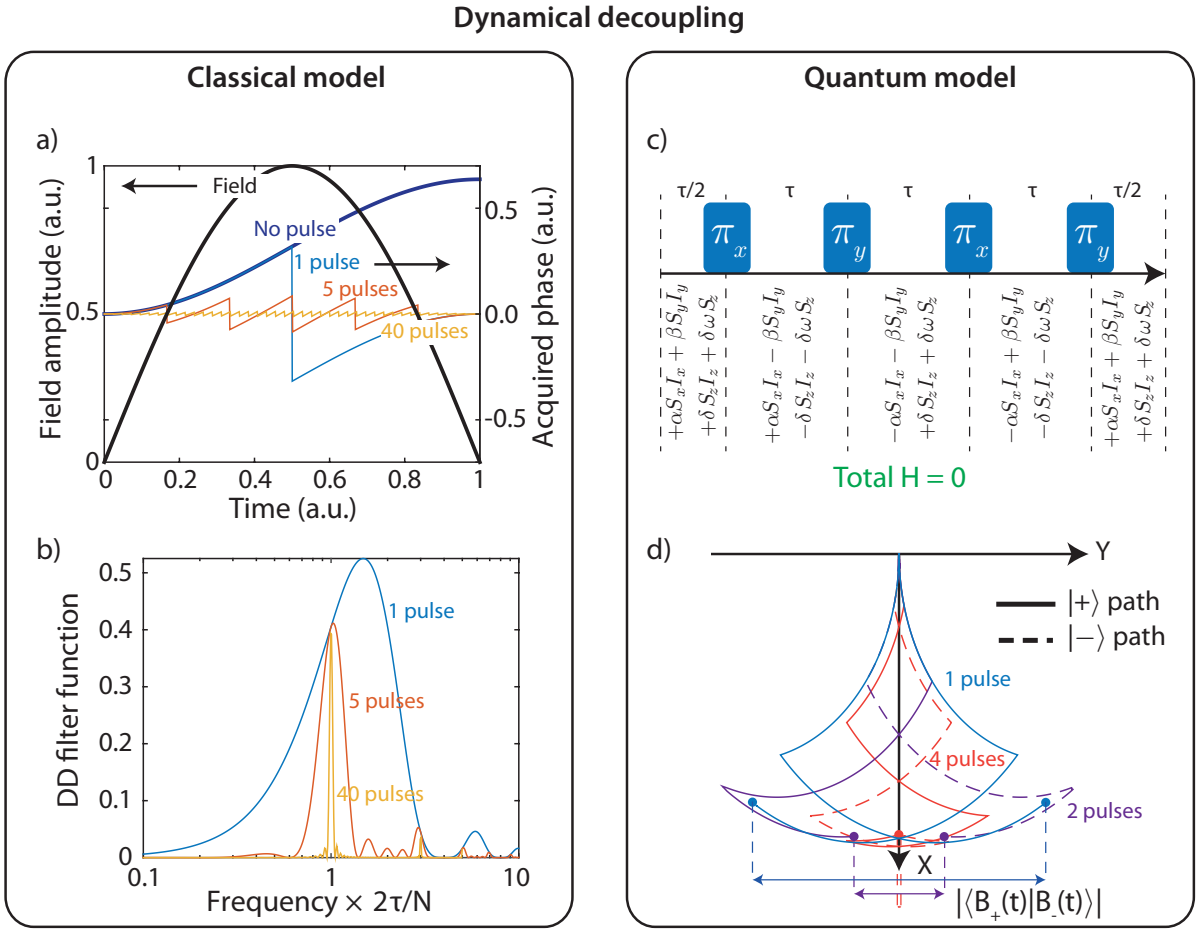


Figure 4.3: **Illustrations of dynamical decoupling (DD).** a) A varying magnetic field as an example for a classical Z noise (in black) results in spin dephasing (blue). When π pulses are applied, the spin state flips and the phase is inverted. As the pulse number is increased, the time appears to be "discretized" corresponding to reduced phase acquisition time. b) Equivalent filter function of DD for N pulses with equal spacings τ/N using the equation in [BUV$^+$09, BGY$^+$11]. As N is increased, DD becomes a very narrow bandpass filter centered around the frequency $\frac{N}{2\tau}$. c) XYXY universal DD sequence. S is the operator for the spin being controlled and I is for spins in the environment. α, β and δ are arbitrary coefficients for the XX, YY and ZZ terms, respectively. Each pulse rotates the spin basis around its axis (x,y), effectively modifying the Hamiltonian in the interval. To first order in τ, the total Hamiltonian of the sequence is the sum of the various intermediate Hamiltonians. Considering an arbitrary coupling with the bath spin here, the sum cancels out at the end thus decoupling the spin. d) Pseudo-spin representation (projected on the X-Y plane) of a bath in the presence of DD pulses. Decoherence of the central spin is directly related to its entanglement with the bath, characterized by the distance between the bath states after their separate evolution for the two central spin states. As the pulse number increases, the distance diminishes reducing the entanglement.

remote ^{29}Si spins.

The quantum side of DD is of more interest to us here. When a control pulse is applied to a qubit, this is usually seen as rotation of its state. Equivalently, it can be seen as rotating the Hamiltonian that defines the system, and, in particular, the interactions with the environment. For any Z noise (i.e. noise based on an interaction that couples to S_z) for example, a π pulse along X or Y thus modifies the interaction from Z to $-Z$. Therefore, a DD sequence can be thought of as adding different interactions together, i.e. with an evolution:

$$U_{DD} = e^{-iH_1 t_1} e^{-iH_2(t_2-t_1)} ... e^{-iH_{N+1}(t_{N+1}-t_N)} \tag{4.18}$$

where $H_n, n = 1..N+1$ are the different interactions for each interval in the N pulse sequence. A Hahn echo sequence for example with a Hamiltonian $H = \delta\omega S_z$ where $\delta\omega$ is a static detuning becomes $e^{-i\delta\omega S_z t} e^{i\delta\omega S_z t} = \mathbb{1}$, and so becomes independent of $\delta\omega$ and the spins are refocused. Matrix exponentials cannot always be added together as the Hamiltonians do not necessarily commute $[H_n, H_{n+1}] \neq 0$. The basis for DD is to make a first order Suzuki-Trotter approximation [HS05] (or similarly use the Magnus expansion [BCOR09]) in time such that $e^{-iH_n \frac{\tau}{N+1}} e^{-iH_{n+1} \frac{\tau}{N+1}} = e^{-i(H_n+H_{n+1})\frac{\tau}{N+1} + O\left(\left(\frac{\tau}{N+1}\right)^2\right)}$ (considering equal intervals for simplicity). At longer spacings $\frac{\tau}{N+1}$, second order terms emerge, the decoupling is not as efficient and decoherence restarts. DD can be demonstrated simply when only π pulses are used: the Hamiltonian always switches between two values $H_\pm$, and if N is large, the expansion gives:

$$\left(e^{-iH_+ \frac{\tau}{2N}} e^{-iH_- \frac{\tau}{2N}}\right)^N \overset{N\to+\infty}{\to} e^{-i(H_+ + H_-)\frac{\tau}{2}} \tag{4.19}$$

For example, for a common Hamiltonian of the form $H_\pm = H_0 \pm H_I$, the interaction H_I is canceled if the qubit is flipped fast enough.

Until now, only DD sequences with π pulses were considered but rotations with different angles and along different axes can be combined to obtain first order cancellation of more complex interaction Hamiltonians at the end of the sequence. An example is given in Figure 4.3(c)

with the XYXY sequence which can cancel any interactions with a qubit, as long as no coupled qubit is simultaneously controlled. XYXY is also quite robust again pulse error and is valid for any input state (see Section 4.3.2). When coupled qubits are simultaneously controlled, sequences using $\pi/2$ pulses are preferred (like WAHUHA in Section 4.3.2). Finally, though not considered in this work, dynamical decoupling can be brought to the limit where $\tau \to 0$, that is the spins are continuously driven. This is called the spin-locking regime as the spins (after the initial $\pi/2$-pulse) are forced to remain in the transverse plane of the Bloch sphere, aligned with the direction of the applied microwave field. While this could theoretically extend T_2 to T_1 [NDH$^+$11], there are a lot of requirements for this method to be practical: high continuous microwave power (which results in heating) to compensate for "B_0" (static magnetic field) inhomogeneity and eliminate high frequency dephasing noise, low power and phase fluctuation (both spatial and temporal) of the microwave field.

Finally, DD can also be interpreted using the pseudo-spin picture for a bath [ZWL11]. Decoherence in this picture emerges from the divergence in the bath evolution for the two different states of the central spin. When a π pulse is applied on the central spin, the rotation axis is suddenly switched, and the two trajectories tend to come back together. To first order approximation, the two trajectories become equal, hence no decoherence. For higher orders, cancellation is not perfect due to non-commutation. As N increases, the trajectories end up closer and closer as shown in Figure 4.3(d). In $^{\text{nat}}$Si this means that the central spin is disentangled from the ^{29}Si, and the coherence times can be extended.

4.2.2 Time symmetry in DD and many-body correlations

As described above, dynamical decoupling (DD) can be used to decouple a central spin from its bath. I therefore investigate experimentally the behaviour of the electron spin coherence T_{2e} in ^{31}P when using DD. Two sequences are considered here (Figure 4.4): the Carr-Purcell-Meiboom-Gill (CPMG) [CP54, MG58] and Uhrig Dynamical Decoupling (UDD) [Uhr07] sequences. Both CPMG and UDD only have π pulses, the former with equal intervals between

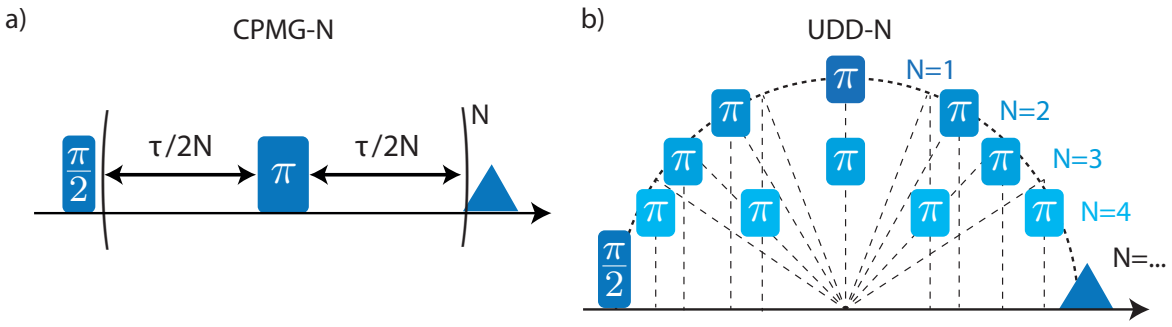


Figure 4.4: **CPMG and UDD sequences.** a) CPMG has equal spacings between pulses. b) The spaces of pulses under UDD follow a sine relation represented by a semicircle divided into N segments (a sequence corresponds to the π pulses aligned horizontally with a specific shade of blue, and with the initial $\pi/2$ pulse and echo signal).

each pulse, the later following the relation $t_n = \tau \sin^2\left(\frac{n\pi}{2(N+1)}\right)$, $n = 1..N$ for the pulse positions. In addition, the π pulses in CPMG must be applied orthogonal to the $\pi/2$ pulse axis (otherwise it is only a Carr-Purcell sequence which is not robust again pulse errors). CPMG is simple to apply in practice and therefore commonly used; UDD is a bit more difficult and less used, but has been demonstrated to be more efficient (N pulses refocus the interaction up to the $N+1$ order in time) [YL08]. Both UDD and CPMG are single axis sequences, i.e. pulses are applied either along X or along Y, but not both. In this case, pulse errors accumulate faster as N increases for spin states orthogonal to the pulse axis, resulting in fast signal decays for such states compared to those parallel. Thus, they are generally not appropriate for quantum computing for high N, as compared to sequences such as XYXY where the pulses are applied along both X and Y. In the following case, both UDD and CPMG were used with $N \leq 6$ (low enough to avoid much error accumulation) and the main interest here is the decay behavior as opposed to very long coherence times.

Measurements presented here are realized at X-band on a ^{nat}Si sample (commercially available Czochralski wafer) with a ^{31}P concentration of 3×10^{14} cm^{-3}. The T_{2e} decays from both CPMG and UDD are shown in Figure 4.5(a) for N between 1 (Hahn echo) and 6. As the number of pulses is increased, the limited fidelity for our π inversions adds up and can result in erroneous signals. In particular, any pair of imperfect pulses can produce an effective π pulse

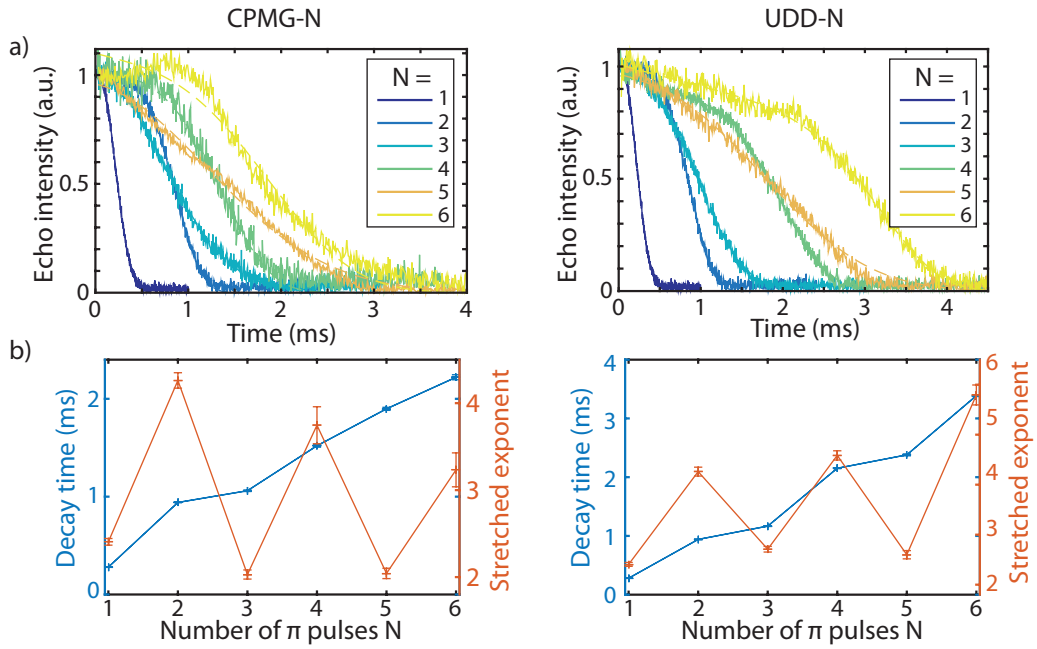


Figure 4.5: **CPMG (left) and UDD (right) experiments in ^{nat}Si:^{31}P.** a) T_{2e} decay curves as a function of pulse number N. The curves are fitted (dashed lines) using a stretched exponential decay $e^{-(t/\tau)^s}$. b) T_{2e} values and stretched exponent value s as a function of N. s varies significantly between odd and even number of pulses. Simulations from W.L. Ma of the decay curves using CCE can be found in [ZWL+14].

and refocus parts of the ensemble at undesired times, leading to so-called "stimulated echoes". When such echoes overlap with the desired one (from the spins that have properly been flipped by all the π pulses), the experimentally observed decay curves gain unwanted contributions. The phases of the applied pulses were therefore cycled in such a way as to remove the contribution of all undesired echoes. For UDD, the timings between each pulse are different and most stimulated echoes fall outside the desired one which can then be isolated. For example, the phase cycling sequence for UDD-4 requires simply subtracting the echo from two experiments where the first two pulses are changed from $+\pi$ to $-\pi$ and the last two are $+\pi$. For CMPG, this is more challenging as the intervals are equal and not all possible stimulated echoes are suppressed for CPMG-5 and CPMG-6. More details on phase cycling can be found in Appendix A.

As N increases, the time constant of the coherence decay extends from 0.5 ms to 2 ms with CPMG and 3 ms with UDD. This indeed confirms the efficiency of the UDD sequence. More interestingly, the shape of the decays seems to depend strongly on the pulse number. For even

pulses for example, the signal amplitude decreases very slowly at short times. This is a signature of a stretched exponential behaviour $\exp(-(t/\tau)^s)$, where s is the stretch factor, which is then used to fit the data in Figure 4.5(b). Instantaneous diffusion (ID) is also taken into account as it is known to limit the coherence times at 10 ms at this concentration, independent of CPMG or UDD pulse numbers. The stretch factor s is seen to oscillate depending on the parity of N: it is about 2 for odd numbers of pulses, and 4 for even numbers. Finally, the decay times seems to be slightly longer with even N than odd numbers, especially with UDD.

Where does this behaviour come from? It is unlikely to be from some classical source of noise as it would only rescale T_{2e} without changing the shape (in the filtering model, larger pulse numbers means mostly that for a given sequence duration τ, the frequency axis is offset). In the quantum picture, there is a major difference between odd and even sequences. Indeed, the latter are symmetric in time, meaning that Eq. 4.18 becomes (considering that the π pulse switches H_n between $H_\pm$ only):

$$U_{DD} = e^{-iH_+t_1}e^{-iH_-(t_2-t_1)}...e^{-iH_-(t_2-t_1)}e^{-iH_+t_1} \tag{4.20}$$

which has the property that $U_{DD}(\{t_n\})U_{DD}(-\{t_n\}) = \mathbb{1}$, where $\{t_n\}$ are the pulse timings. This time symmetry results in cancellation of any even order terms in the Suzuki-Trotter approximation [HS05] such that $U_{DD} = e^{-i(H_++H_-)\frac{\tau}{2}+O(\tau^3)}$. Because the higher order terms are due to non-commuting elements, this symmetry would not be relevant to the pure dephasing case (Z only). In the pseudo-spin picture, this is valid as $[\delta\omega_+S_z + \Omega_+S_x, \delta\omega_-S_z + \Omega_-S_x] \neq 0$, hence odd and even sequences can be expected to behave differently, and the even case to be more efficient. These considerations are not sufficient, however, to offer a quantitative assessment of the stretch factor s as it also depends on the donor-bath and intra-bath couplings (and averaging). For example, in Figure 4.5(b) (clearly for CPMG, not obvious in UDD), the stretch factor slowly decreases with pulse number as the coherence time starts to be longer than the ^{29}Si nearest neighbour coupling of 1 kHz, entering a "Markovian" regime.

The higher orders in the time expansion of the operator U_{DD} correspond to slower pro-

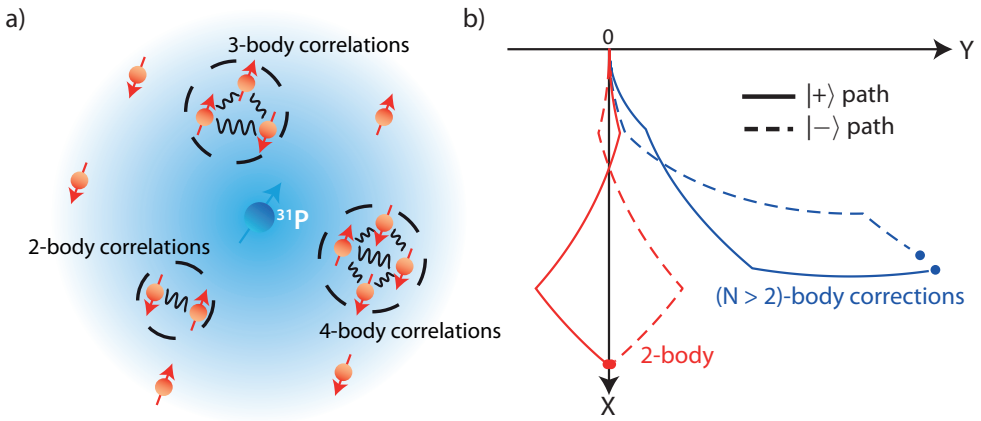


Figure 4.6: **Many-body correlations.** a) Illustration of various ^{29}Si spin clusters with many-body correlations and interacting with the donor electron (blue background for its wavefunction). Interactions are considered dominant between two specific spins of the cluster, forming a pseudo-spin with renormalized Hamiltonian [ZWL$^+$14]. b) Pseudo-spin evolution for an arbitrary ^{29}Si spin pair alone (red) and in a larger cluster (blue). The path difference is due to renormalization of the pair energy $\delta\omega_\pm$.

cesses. They can result from the evolution of the spin pair in the pseudo-spin model, however it is known from the Linked Cluster Expansion (LCE) theorem [SYS07], that the N-th order time expansion also corresponds to dynamics of spin clusters of up to N spins (Figure 4.6(a)). Effects from larger cluster sizes can still be partially captured with a single pseudo-spin whose Hamiltonian is modified, as long as all FF terms are disregarded to keep a two-level system. In this case, the pseudo-spin Hamiltonian (Eq. 4.12) is renormalized by the couplings with the other spins such that (using first and second orders in perturbation theory):

$$\delta\omega_\pm = \pm\frac{1}{2}\Delta A + \sum_k f_{\pm,k}(t)(C_{1k} - C_{2k}) \tag{4.21}$$

$$\Omega_\pm = C_{12} + \sum_k \frac{1}{2}\frac{C_{1k}C_{2k}}{\omega_k} \tag{4.22}$$

where $C_{1,2k}$ are the dipolar couplings between the spin pair $(1,2)$ and another spin in the cluster (k), with energy ω_k. $f_{\pm,k}(t)$ is the expectation value of the ZZ part of this dipolar interaction, but it depends on time (and thus the donor state $|\pm\rangle$) as the evolution of the pseudo-spin changes the relative orientation between the spin pair and the k-th spin. The fact that $f_{\pm,k}(t)$ is time dependent means that the pseudo spin evolution with π pulses is not the same anymore on the

two branches, even to first order, and the time symmetry is not preserved (see Figure 4.6(b)). For the renormalization to be efficient, the new energy $C_{1k} - C_{2k}$ must be quite strong compared to the FF strength C_{12}.

In conclusion, the evolution for odd pulse sequences, such as the Hahn echo, arises from pairs of bath spins. For even pulse sequences, the decays result from higher order configurations, either temporal or spatial, depending on the coupling rates between the various spins. DD hence presents a way to probe this higher processes which is a known challenge in many-body physics.

4.3 Nuclear spin registers in ^{nat}Si

While DD previously offered one order of magnitude improvements to the electron spin coherence time, it remains negligible compared to the three orders of magnitude gain from isotopic purification of silicon to ^{28}Si [TTM$^+$11]. Hence, the role of ^{nat}Si has always been limited to this kind of test-bed studies of more fundamental questions, such as the effects of high order processes or testing classical versus quantum noise models. However, the presence of the many nuclear spins around the donor can also provide new resources for quantum information processing. Recently, it has been demonstrated in the Nitrogen-Vacancy (NV) center in diamond that coupling to its carbon-13 nuclear bath offers a register of multiple spins usable for quantum error correction (QEC) [DCJ$^+$07, TCvdS$^+$14, WWZ$^+$14]. For NV centers, optical single-spin readout is easily accessible and therefore a specific set of spins can be manipulated. In silicon, single-spin control remains a relatively new development so I consider the possibility of doing the QEC on the full ensemble here (though most of the discussion is equally applicable to single spins). I give here a proposal for its realization followed by experimental measurements of the coherence times of the nuclear spins involved in the scheme.

4.3.1 Proposal for quantum error correction (QEC)

Quantum error correction (QEC) was first proposed by P. Shor (1995) and then A. Steane (1996) [Sho95, Ste96b, Ste96a] for preserving a qubit coherence beyond its inherent value. This was a critical step in establishing the practical feasibility of quantum computation. The main idea of QEC is to encode the information of a single qubit into many qubits: if errors happen independently on some of the qubits, as long as there is a dominant amount of non-erroneous qubits, the information can still be retrieved by a majority voting [Got00, KLA+02]. This can also be looked as putting a certain "distance", created by the larger Hilbert space, between the two logical states where the data is encoded. A single error would keep you close to the initial space, and so can be corrected. Experimental realizations of QEC were first done in NMR in 1998 [CPM+98] and later with ion traps [CLS+04], superconducting qubits [RDN+12] and NV centers [TCvdS+14, WWZ+14].

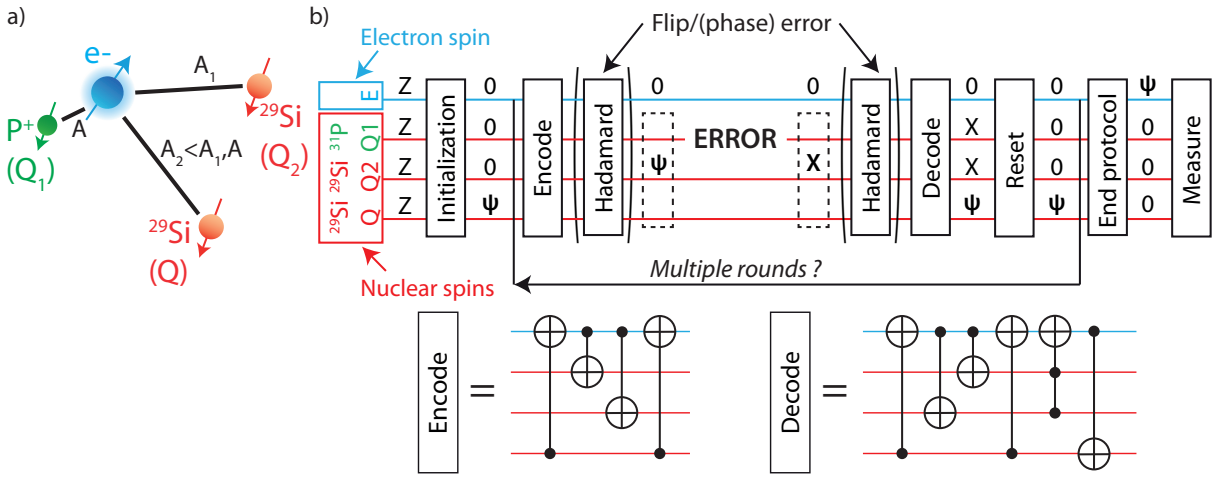


Figure 4.7: **Quantum error correction (QEC) proposal.** a) The most basis QEC protocol requires 1 qubit and 2 ancillae. The qubit here is ^{29}Si spin (Q) weakly coupled to the electron, and the two ancillae are the donor nuclear spin (Q_1) and a strongly-coupled ^{29}Si spin (Q_2). b) QEC protocol: initialization (polarization from thermal equilibrium noted as "Z"), encoding, decoding and reset. The Hadamard in bracket determines whether the QEC sequence corrects errors from bit-flips (if absent) or phase-flips (if present). The electron spin of the donor is not directly part of the QEC scheme, but acts as intermediary between the nuclear qubits. It is also necessary for hyperpolarization and measurement at the very end of the experiment.

The simplest protocol is the 3-qubit encoding, where one "data" qubit, storing the original

information, is entangled -using CNOT gates- with two ancilla qubits, or two ancillae. This results in the following encoded state:

$$|\phi\rangle = \Big(\alpha\,|0\rangle_Q + \beta\,|1\rangle_Q\Big) \otimes |00\rangle_{Q_1Q_2} \Rightarrow |\phi\rangle = \alpha\,|000\rangle_{QQ_1Q_2} + \beta\,|111\rangle_{QQ_1Q_2} \tag{4.23}$$

where Q is the qubit and Q_1 and Q_2 the two ancillae. This encoding preserves a single error, either one bit flip/X-error ($\alpha \leftrightarrow \beta$), or one phase flip/$Z$-error ($\beta \rightarrow -\beta$) depending on the application of additional Hadamard gates (one for each qubit after encoding). For a bit flip, for example, a single error on one of the qubit would go as:

$$\alpha\,|000\rangle_{QQ_1Q_2} + \beta\,|111\rangle_{QQ_1Q_2} \Rightarrow \alpha\,|000\rangle_{QQ_1Q_2} + \beta\,|111\rangle_{QQ_1Q_2} \text{ No error} \tag{4.24}$$

$$\Rightarrow \alpha\,|100\rangle_{QQ_1Q_2} + \beta\,|011\rangle_{QQ_1Q_2} \text{ Error on } Q \tag{4.25}$$

$$\Rightarrow \alpha\,|010\rangle_{QQ_1Q_2} + \beta\,|101\rangle_{QQ_1Q_2} \text{ Error on } Q_1 \tag{4.26}$$

$$\Rightarrow \alpha\,|001\rangle_{QQ_1Q_2} + \beta\,|110\rangle_{QQ_1Q_2} \text{ Error on } Q_2 \tag{4.27}$$

The error can be separated from the data qubit and given to the ancillae only. This is realized by the same operation as the decoding (CNOTs) followed by an additional Toffoli gate conditional on the ancillae such that:

$$\alpha\,|000\rangle_{QQ_1Q_2} + \beta\,|111\rangle_{QQ_1Q_2} \Rightarrow \Big(\alpha\,|0\rangle_Q + \beta\,|1\rangle_Q\Big) \otimes |00\rangle_{Q_1Q_2} \tag{4.28}$$

$$\alpha\,|100\rangle_{QQ_1Q_2} + \beta\,|011\rangle_{QQ_1Q_2} \Rightarrow \Big(\alpha\,|0\rangle_Q + \beta\,|1\rangle_Q\Big) \otimes |11\rangle_{Q_1Q_2} \tag{4.29}$$

$$\alpha\,|010\rangle_{QQ_1Q_2} + \beta\,|101\rangle_{QQ_1Q_2} \Rightarrow \Big(\alpha\,|0\rangle_Q + \beta\,|1\rangle_Q\Big) \otimes |10\rangle_{Q_1Q_2} \tag{4.30}$$

$$\alpha\,|001\rangle_{QQ_1Q_2} + \beta\,|110\rangle_{QQ_1Q_2} \Rightarrow \Big(\alpha\,|0\rangle_Q + \beta\,|1\rangle_Q\Big) \otimes |01\rangle_{Q_1Q_2} \tag{4.31}$$

The data qubit state has been recovered and the error is now on the ancillae. This corresponds to a single round of correction and a full, multi-round, implementation must reset the ancillae to start again. Instead of resetting the spins, another solution when single-qubit measurement

is available is to measure the ancillae and then manipulate them back to some desired state. While this could be achieved in a single-spin device, measurement in an ensemble only gives an average of the spins' state and therefore cannot be used in a feedback control. Hence, only the encoding/decoding/reset protocol is considered as illustrated in Figure 4.7(b). Also, any measurement in the donor system usually requires swapping the state of one of the nuclear spin to the electron spin, as it is the only spin that can be directly measured (though quantum non-demolition (QND) measurement of nuclear spin states can be achieved in single spin devices, without the need to transfer states with the electron spin [PTD$^+$13]).

So how can we realize QEC in silicon? First of all, for an experimental realization, we need to decide where to store the three qubits. They need to have inherently similar and long coherence times, otherwise the QEC scheme will not be very efficient. In the ^{nat}Si system, we have the electron and nuclear spin qubits of the donor and the various ^{29}Si nuclear spins available nearby. The nuclear spin coherence times are not known and so must be characterized; we will see that they are much longer than the electron spin T_{2e} and so combining the electron with the other nuclear spins would not be optimal. Furthermore, choosing one particular ^{29}Si spin means taking a subset of the ensemble as not all donors have the same environment, and thus may not have a ^{29}Si at the required site. Each additional ^{29}Si further reduces the effective number of donors and hence the measured signal in the experiment, which is obviously an issue. Therefore, the best configuration is to use the donor nuclear spin, which is always present, with two other ^{29}Si spins.

How do we then choose which is a data qubit and which is an ancilla qubit? For that we have to consider how to perform the reset protocol. Resetting and initializing the spins to a specific state requires some non-unitary operation with one critical condition: the data qubit must not be affected by the operation. The only non-unitary operation for the nuclear spins is the spin relaxation however this is too slow and would involve equally the data qubit and the ancillae. Therefore, the reset scheme has to involve the electron spin: first by hyperpolarizing it and then transferring its polarization to the nuclear ancilla. One common solution is dynamical

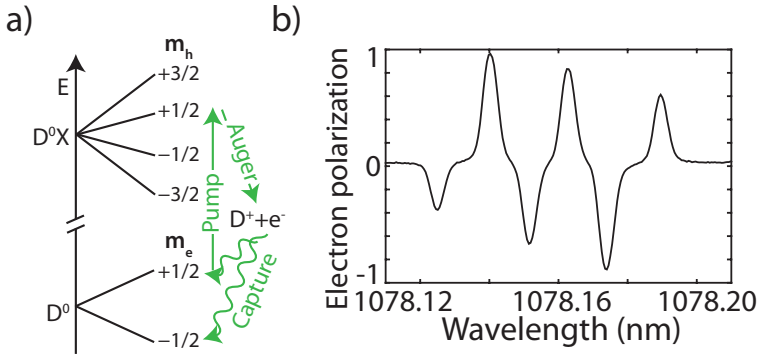


Figure 4.8: **Bound exciton (BE) hyperpolarization scheme.** a) Energy level diagram of a ^{31}P donor (D^0) and the BE hole spin (D^0X), reproduced from [SSY$^+$11]). After laser illumination, an electron-hole pair is created, the free electron spin forms a singlet with the donor electron spin while the hole remains bound to the donor. The BE then undergoes Auger recombination, the donor ionizes ejecting an electron which can be captured later (ms) by any other ionized donor. b) Electron hyperpolarization as a function of laser wavelength in ^{31}P. The value is extrapolated from the echo signal, with and without illumination, and considering thermal polarization at 4.5 K and 9.7 GHz. Note that the real polarization might be slightly smaller as it could be partly from ^{31}P nuclear spin polarization (due to cross-relaxation)

nuclear polarization (DNP) that takes advantage of the fast T_{1e}, however it is not a very efficient process. More recently, the use of the donor bound exciton (BE, electron-hole pair bound to the donor) for hyperpolarization was demonstrated [SSS$^+$10, SSY$^+$11, SST$^+$12] with above 90% electron polarization possible and even some nuclear polarization too (though mainly in ^{28}Si). It works by ionizing the donors with a laser ($\approx$ 1070–1080 nm) selectively for one electron spin state, which then recaptures an electron in a random spin state. Hence, the optically targeted state population is slowly reduced while the other one is increased (see Figure 4.8). The process is relatively fast compared to T_{1e} at low temperatures, about 10–100 ms. Finally, the BE can also be used as a measurement technique for the electron spin state, by collecting the Auger electrons that are ejected from the donor when the BE recombines.

Both DNP and BE polarization mechanisms involve random electron spin flips, either due to relaxation or ionization, which results in sudden frequency shifts for the nuclear spins via the change in hyperfine interactions, and therefore dephasing and complete loss of signal in the ensemble. In NVs for example, optical measurement of the electron gives the same issue and one solution was to use very weakly coupled carbon-13 nuclear spins [TCvdS$^+$14]. If

the coupling is much lower than the time during which the nuclear spin acquires the unknown phase, then dephasing remains limited. For NVs, the time uncertainty is only for a few 100 ns, while the coupling strength is 10–100 kHz. However, the BE polarization process in silicon is much longer and couplings would have to be extremely small (Hz).

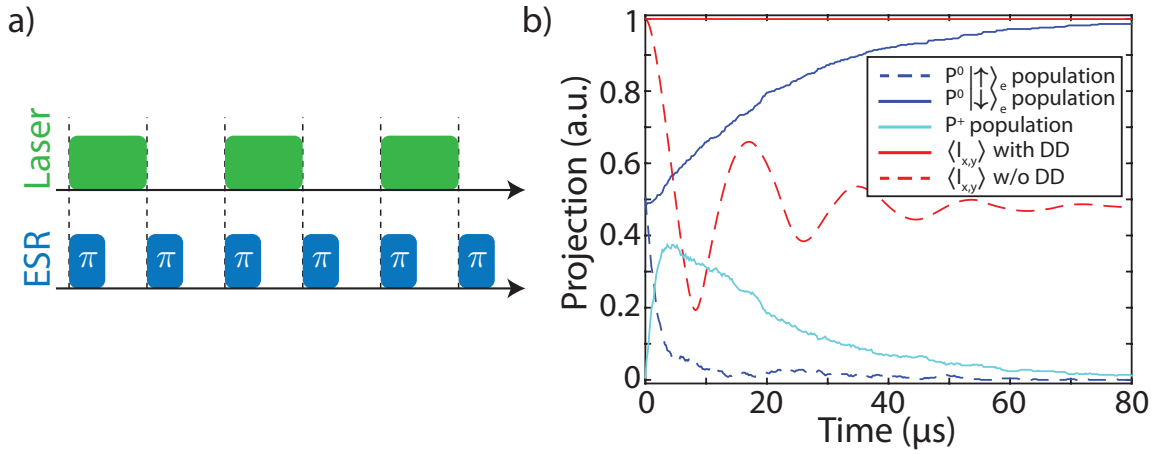


Figure 4.9: **Spin reset.** a) Protection scheme against nuclear spin (^{29}Si) dephasing during laser illumination. DD on the electron spin (ESR) is synchronized with the laser to allow polarization. b) Simulation of the sequence in (a), showing the electron spin up and down populations for the neutral donor P^0, the population of ionized donors P^+, and the nuclear spin coherence ($|\langle S_x\rangle + i\langle S_y\rangle|$) with and without DD on the electron spin. The populations are only measured every other ESR π pulses. Simulation parameters are arbitrary: BE creation and ionization rate is 1 MHz, recombination rate is 0.1 MHz, and π-pulse decoupling rate is 10 MHz for a hyperfine interaction strength of 0.1 MHz.

A possible solution would be to use dynamical decoupling to artificially decouple, at any desired time, the data qubit from the electron spin. The interaction time uncertainty is then reduced to the duration between each pulses, and if fast enough, the dephasing can be minimized. Using π pulses on the electron spin, this can modeled by the two Hamiltonians $H_\pm$ (similar to Section 4.2.1):

$$H_\pm = \pm\omega_e S_z + \omega_n I_z \pm A S_z I_z \tag{4.32}$$

where ω_e, ω_n and S, I are respectively for the electron and nuclear spins, and A is the hyperfine interaction. In the limit of fast switching (compared to A), the evolution becomes $\exp(-i(H_+ + H_-)\frac{\tau}{2}) = \exp(\omega_n I_z \tau)$ which is now independent of A. Here, only the electron spin was flipped because of the much faster manipulation speed compared to nuclear spins, and

it is very convenient as the data qubit does not have to perturbed. This solution is not perfect however due to the BE polarization process. Indeed, applying DD on the electron spin during ionization means that both electron spin states are pumped, preventing polarization. This issue can be circumvented by synchronizing the DD and laser pulses, with illumination occurring only every other π refocusing pulse. In this way, it is always the same spin population that is pumped out, without ever ionizing the donor, while the electron spin state being polarized remains untouched. The full scheme is shown and simulated in Figure 4.9. It should be noticed that multiple rounds of such polarization requires polarizing all ancillae by successive transfer of the electron spin state.

Finally, we conclude that the optimal choice of data qubit is a weakly coupled ^{29}Si while the ancillae are one strongly coupled ^{29}Si (for faster manipulation) and the donor nuclear spin, and the electron spin mediates everything as shown in Figure 4.7(a). Aside from hyperpolarization, the main challenge in the QEC protocol is the ability to efficiently realize all the required gates, in particular:

1. The inversion pulses for the DD scheme, which could well number above 10^4 using BE in ensembles. For single spins, the reset scheme can be adapted to hyperpolarization via tunneling to a charge sensor. In this case, this would require only about 300 pulses. This inversion fidelity is likely to be the most critical component of the QEC scheme, which will have to be $\gg 99.99$ % for multi-round error correction, a hard requirement to achieve. Also, efficient inversions pulses such as composite or adiabatic pulses [Wim94, TG97] might not even be possible due to their long durations (and therefore low DD rate).

2. The CNOT gates on the electron spin conditional on one nuclear spin state for encoding and decoding. Generally, such CNOT can simply be realized by ESR pulses with a narrow frequency bandwidth, of course at the condition that the nuclear spin states can be resolved in frequency. This should be relatively easy for strongly coupled nuclear spins in single spins system. For ensembles, this becomes more complicated as each donor has its own local ^{29}Si bath configuration, leading to a spread in frequency for any given ESR

transition, though this should not prevent selective pulses.

3. The Toffoli gate on the electron spin conditional on two nuclear spin states for decoding. One simple solution would be to use the donor nuclear spin as one of the two nuclear spins, in which case its strong hyperfine interaction with the electron spin offers such a large frequency shift (as a function of the donor nuclear spin state) that the Toffoli gate would be no harder than a CNOT gate conditional on the second nuclear spin.

If these challenges can be overcome (realistically hard in ensembles, much easier for single spins), being able to realize multiple rounds of QEC using only the donor environment might pave the way for very efficient quantum memories in donors in silicon.

4.3.2 ^{31}P and ^{29}Si nuclear spin coherence

T_{2n} of the ^{31}P nuclear spin was measured in ^{28}Si samples in [MTB$^+$08, SST$^+$12], up to 180 s, but there are no data available for ^{nat}Si. For this reason we measured a ^{nat}Si sample with a ^{31}P concentration of 6×10^{15} cm^{-3}, using the T_{2n} sequence described in Figure 2.7(b). At this donor concentration, donor-donor processes do not contribute to the nuclear spin decoherence. The temperature T was 4.5 K, with $T_{1e} > 10$ s. The magnetic field was aligned with the [100] crystal axis to obtain the longest electron and nuclear spin coherence times. The RF π pulse duration was 10 μs which is non-negligible compared to T_{2e} therefore this orientation also offers the best signal intensity. In Figure 4.10(a), the observed decay follows a stretched exponential with $T_{2n} = 1.1 \pm 0.1$ s, which is quite long and so useful for the QEC.

For ^{31}P, the gyromagnetic ratio is 17.23 MHz/T compared to 8.46 MHz/T for ^{29}Si, corresponding to a difference of 3 MHz in Zeeman frequency at X-Band (0.33 T). The ^{31}P nuclear spin is therefore quite detuned from the bath, contrary to a ^{29}Si spin which is readily able to flip-flop. In NMR with very low donor concentration, the coherence of ^{29}Si spins was measured to be about 5 ms [LMY$^+$05], much lower than for ^{31}P and thus a problem for the QEC protocol. However, the presence of a donor provides a hyperfine interaction, detuning the ^{29}Si spins from

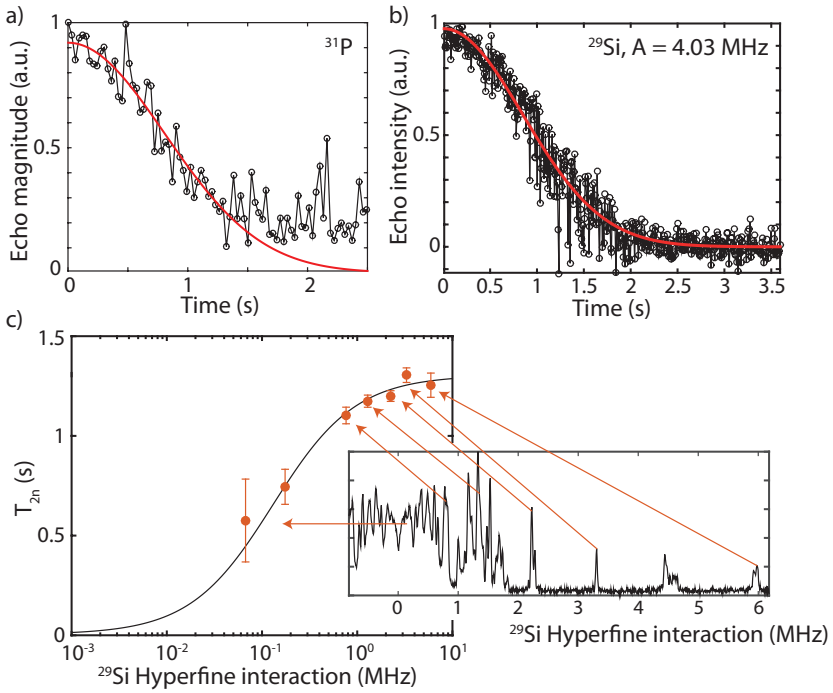


Figure 4.10: **Nuclear spin coherence times T_{2n}.** a) ^{31}P nuclear spin coherence decay. In red, fitting to a stretched exponential $e^{-(t/T_{2n})^s}$ with $T_{2n} = 1.1 \pm 0.1$ s and $s = 1.3 \pm 0.1$. The fitting is constrained to decay to 0 here as we measured the magnitude of the signal here (therefore the noise is always positive). b) ^{29}Si nuclear spin coherence decay with strong coupling to the donor (4.03 MHz). c) T_{2n} times of ^{29}Si for various hyperfine values with the donor. The line in black is only a guide to the eye, limited at weak coupling to the NMR value (4 ms) and at strong coupling to ≈ 1.3 s.

one another, and therefore should extend their coherence times. In Figure 4.10(b,c), $T_{2n}(^{29}\text{Si})$ is measured as a function of the various hyperfine interactions that are available (Figure 4.1(b)): the larger the coupling strength, the longer the spin coherence time which saturates at 1.3 s. This measurement is good news for the protocol, with both ^{31}P and ^{29}Si spin coherence being similar and quite long. We mentioned that a weakly coupled spin is preferable, hence we can conclude from this that the data qubit should be around 0.1 to 1 MHz to obtain a good balance between low coupling strength and long coherence (> 0.5 s).

The origin of the 1 s coherence timescale as well as the hyperfine coupling strength dependence is considered in details, using the pseudo-spin theoretical model, in Appendix C. From the experiments, we can still test directly two competing models, the direct and indirect FF processes. Indeed, there is one special case for which pairs can readily FF despite the

hyperfine-induced detuning: some sites are equivalent under silicon lattice symmetry (they belong to the same shell), and for some orientations with respect to the magnetic field, have equal interactions with the donor. A pair of such spins, called "equivalent pair" (EP), consequently have no detuning and is free to FF (resulting in both iFF and dFF-induced decoherence).

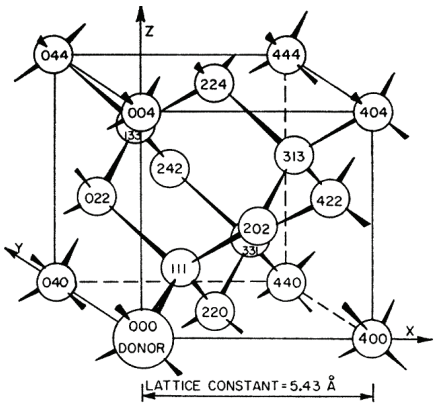


Figure 4.11: **Lattice sites in the silicon crystal coordinate system.** Figure reproduced from [HM69].

Shell	Position (x y z)	Isotropic hyperfine (MHz)	Atoms/shell	Degeneracy $B_0 \parallel [100]$
A	(0 0 4)	5.96	6	{2,4}
B	(4 4 0)	4.51	12	{8,4}
C	(3 3 3)	3.30	4	{4}
D	(-)	2.23	12	{8,4}
E	(1 1 1)	0.54	4	{4}

Table 4.1: **Lattice symmetry.** Example of shells around a donor in silicon with corresponding isotropic hyperfine value for ^{nat}Si:^{31}P, number of atomic sites per shell and degeneracy i.e. number of equivalent sites with equal hyperfine interaction. Data was taken from [HM69]. The shells are given by their position in the lattice (see Figure 4.11) such that any permutation or sign change of the triplet (x y z) is allowed. For example, (0 0 4) is one lattice constant away from the donor and is equivalent to (-4 0 0), (0 4 0), etc.

In Table 4.1, the shells with the largest hyperfine values to the donor are given, along with the number of atomic sites per shell and their degeneracy. Shell E is a special case as it is nearest neighbour with the donor, yet has a small interaction due to the oscillating electron wavefunction (see Figure 4.1(c)). Shells A, C and D correspond to the T_{2n} values with the three

highest hyperfine interactions in Figure 4.10(c). These shells have respectively {2,4}, {4} and {8,4} degeneracies for $B_0 \parallel [100]$, where {} are the numbers of equivalent sites such that the sum is equal to the number of atoms per shell. If dFF was the dominant process here, we would therefore expect a very strong dependence on these values, however the experiment shows only slight variations.

Decoherence from direct and indirect processes can also be separated using dynamical decoupling sequences. As explained in Section 4.2.1, to first order approximation of the matrix exponential, sequences can be constructed such that the total evolution under some Hamiltonian is canceled. For dFF of EPs, the central spin and the paired spin are simultaneously rotated and therefore sequences with only π pulses cannot be used as XX, YY or ZZ type of interactions are left unaltered. On the other hand, π pulses can properly refocus ZZ interactions for iFF processes. It is still possible to refocus dFF interactions by taking advantage of the form of the dipolar interaction: $2I_{0z}I_{1z} - (I_{0x}I_{1x} + I_{0y}I_{1y})$, where I_0 and I_1 are the spin operators of the central and paired ^{29}Si spins. Because of the presence of the minus sign in the interaction, applying $\pi/2$-pulses around specific axis rotates the interaction, permuting the X, Y, Z terms, and the summed Hamiltonian can be made to cancel at the end of the sequence. One such DD sequence is the so-called WAHUHA (Waugh-Huber-Haeberlen) [WHH68, HW68], to which we add 5 additional π pulses to allow for echo refocusing as shown in Figure 4.12(a).

The experiment is realized in Figure 4.12(b) on a ^{29}Si spin with hyperfine coupling of 2.23 MHz with the donor. $T_{2\mathrm{n}}$ is measured as a function of the number of π pulses involved in the DD sequence. CPMG with only π pulses gives a clear improvement in the coherence time, while WAHUHA seems to help only as far as the π pulses used, with no obvious effect of the $\pi/2$ rotations. This is in agreement with the iFF mechanism dominating dFF. Finally, this also demonstrates the viability of DD sequences to enhance further the ^{29}Si coherence time, which goes seemingly linearly with the number of π pulses.

To conclude here, we need to mention one last point regarding the ^{29}Si spin coherence times during the QEC protocol. In the initialization/reset scheme, the donor is ionized for a certain

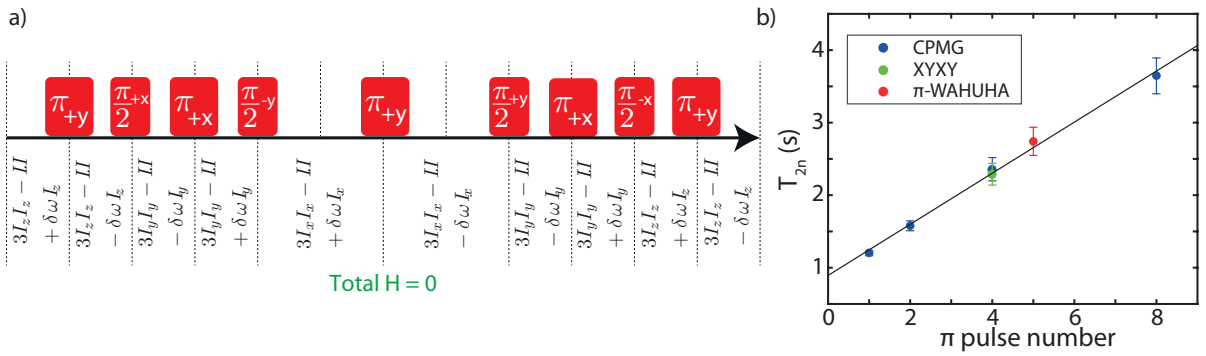


Figure 4.12: **Direct versus indirect processes.** a) π-WAHUHA sequence with effective rotated Hamiltonian between each pulses, considering the coupled spins are flipped together. To first order approximation, the total evolution Hamiltonian is 0. b) Experimental T_{2n} times for various DD sequences for a ^{29}Si with coupling $A = 2.23$ MHz. π-WAHUHA does not improve the coherence beyond what CPMG would do (from linear fit in black), supporting the indirect model. XYXY is a check for pulse errors: if it was higher than CPMG-4, the coherence would be limited by the pulses.

time during which the electron does not prevent the ^{29}Si spins from flip-flopping. The coherence time is then lowered to the bulk NMR value of 5 ms, which is quite problematic. Application of WAHUHA during this time could be a solution, as was demonstrated in [LMY$^+$05] where the ^{29}Si nuclear spin coherence time was lengthen to 20 s (using MREV which is a longer version of WAHUHA).

4.4 Conclusion

In this Chapter, we introduced the concept of the pseudo-spin evolution to explain the bath dynamics and performed experimental tests on it using DD as a probe.The coherence times of nuclear spins in ^{nat}Si, be it that of the donor or the bath, was measured to be in the order of seconds and possibly longer with DD. Even considering the slow manipulation time of the nuclear spins (around 10 μs), they are quite promising as a secondary resource for quantum information.

We now present an alternative method to extend the spin coherence and analyze the effect of the bath: instead of actively modifying the spin evolution with DD, the Hamiltonian is naturally

tuned to a point where certain transitions acquired a reduced sensitivity to the bath dynamics.

CHAPTER 5

Magnetic sensitivity of donor spins

Manipulating the Hamiltonian to produce states insensitive to certain free parameters has been used in many qubit systems in the past. This has been first used in ion-traps to produce atomic clocks and later atomic qubits with transitions insensitive to change in magnetic fields [Kie01, LOJ+05]: they were called "clock transitions (CTs)". Later, in superconducting qubits, transitions insensitive to charge noise were similarly used to create the transmon with longer coherence time than the basic Cooper pair box [Vio02, KYG+07]. There, they were called "optimal working points (OWP)". Finally, magnetic insensitive transitions (this time called "zero first order Zeeman shift (ZEFOZ)") were also studied in rare earth ion dopants [LAS06, MBSL12].

First of all, how do these insensitive transitions arise? Let's take for example the case of a single spin with only its Zeeman interaction with an external magnetic field B_0. For a given value of B_0, the transition frequency f between the two states of the spin is γB_0 where γ is the spin gyromagnetic ratio. The latter is therefore the gradient —or sensitivity— of the frequency with respect to the magnetic field, i.e. is equal to $\frac{df}{dB_0}$. If there are some fluctuations in the field, the frequency varies too depending on this gradient, resulting in dephasing and decoherence

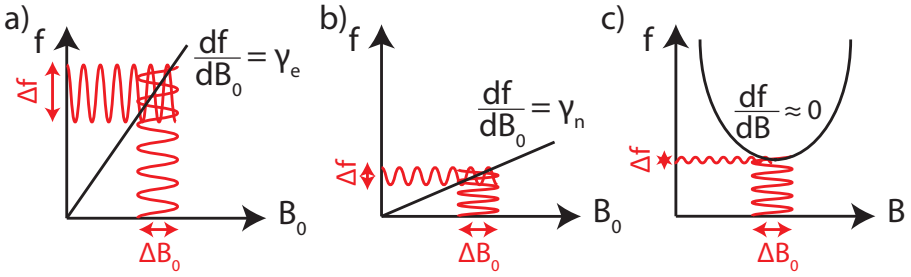


Figure 5.1: **Clock transition illustration.** Transition frequency f as a function of external magnetic field B_0 in systems with different sensitivity $\frac{df}{dB_0}$. In red, a magnetic field fluctuation ΔB_0 results in frequency fluctuations of various amplitudes. a) System with the electron Zeeman interaction only. b) System with the nuclear Zeeman interaction only. c) System with complex Hamiltonian giving rise to clock transitions. The frequency response to magnetic field has a turning point with zero derivative, i.e. insensitivity to the field.

with some corresponding rate. This is illustrated in Figure 5.1(a,b) for an electron and nuclear spin transition: compared with the electron spin, the nuclear spin with its smaller gyromagnetic ratio is already less sensitive to magnetic field noise. A CT occurs when the frequency becomes insensitive to first order in the free parameter, here the magnetic field such that $\frac{df}{dB_0} = 0$ as shown in Figure 5.1(c).

CTs are not available in every systems as they require a certain complexity in the Hamiltonian, for example, the linear behaviour in B_0 illustrated in the Zeeman case cannot provide this. In donors in silicon, this complexity arises from the hyperfine interaction A between the electron and nuclear spin. At low magnetic field ($B_0 \approx A \times I/\gamma_e$), the eigenstates are mixed as the hyperfine coupling is comparable in magnitude to the electron Zeeman interaction, and $\frac{df}{dB_0}$ varies strongly as a function of B_0 and the measured transition.

In order to study these properties, we have to depart here from ^{31}P. While it does provide a simple system, mainly due to having a nuclear spin $1/2$ and being close to the high field limit at X-band, the CTs and in general regime with variations to the magnetic field sensitivity occur at frequency < 1 GHz which cannot readily be measured using ESR. On the other hand, ^{209}Bi has both the strongest hyperfine interaction ($A = 1.475$ GHz) and the largest nuclear spin ($I = 9/2$) of the group V donors, and therefore is fairly mixed even at X-band. The zero-field eigenstates, where the states are fully mixed, are split by $A(I+1/2) = 7.4$ GHz, not so far in

frequency from X-band (9.7 GHz), and can thus be measured with our ESR spectrometer (with some modifications). ^{209}Bi was first characterized in [GWR$^+$10] and later in [WST$^+$12], while CTs in this system were discussed theoretically in [BKM$^+$12, MMNM12].

In this Chapter, I study the spin transitions in ^{209}Bi donors with low sensitivity to magnetic field, not only as a method to increase the electron spin coherence times, both in ^{28}Si and ^{29}Si, but also as a way to better understand the interaction between the donor and the ^{29}Si nuclear bath. In this latter case, I also show the limitations of the $\frac{df}{dB_0}$ model for describing interactions with the bath, when the central spin imposes some back-action on the back dynamics.

5.1 Electron - electron spin interactions at the CTs

In Chapter 3, the various decoherence mechanisms in isotopically purified ^{28}Si samples were summarized, with the electron spin coherence limited by the dipolar couplings between the electron spins of the donors in the ensemble. The dipolar interaction between two spins is proportional to the product of their gyromagnetic ratio, which in the donor basis and for a specific transition is equal to the sensitivity $\frac{df}{dB_0}$. Note that this equivalence is only valid for the Z or ZZ terms of these couplings (see full derivation in Appendix B), because B_0 is applied along Z. However, those terms are responsible to the main decoherence processes in ^{28}Si such as instantaneous diffusion (ID), indirect T_{1e} (iT_{1e}) and indirect flip-flop (iFF). Transitions with low $\frac{df}{dB_0}$ can therefore be expected to have much longer coherence times. This is tested in ^{209}Bi first at X-band where $\frac{df}{dB_0}$ is reduced by about 30 % only, and then at one of its clock transitions.

5.1.1 ^{209}Bi donor electron spin coherence at X-band: the low spin-mixing regime

The first usual limit to the decoherence in ^{28}Si is instantaneous diffusion (ID). ID involves two identical transitions that are excited simultaneously and so is proportional to $\left(\frac{df}{dB_0}\right)^2$, providing a way to eliminate this mechanism which otherwise requires having too low spin concentrations

(Eq. 3.9). In Figure 5.2(a), this is demonstrated with a ^{28}Si:^{209}Bi sample with spin concentration $[\mathrm{Bi}] = 2 \times 10^{15}$ cm^{-3}. ^{209}Bi donors were introduced during crystal growth using the method developed in [RAN06]. Measurements are realized at X-band (9.7 GHz) for each allowed ESR transitions between 0.08 and 0.56 T. As mentioned in Section 3.2, ID can be removed by performing a "tip-angle" experiment where the echo refocusing pulse is reduced from $\theta = \pi$ to 0. The ID contribution to the $T_{2\mathrm{e}}$ decay is therefore proportional to $\left(\frac{df}{dB_0}\right)^2 \sin^2(\theta/2)$ and varying θ enables a direct measurement of the sensitivity $\frac{df}{dB_0}$ (slopes in inset). We observe a very good fit with this model. From Figure 5.2(a), the extrapolated $T_{2\mathrm{e}}$ values at $\theta = 0$ are then plotted in (b): while $\frac{df}{dB_0}$ for each ESR transition seems symmetric with respect to m_I, the $T_{2\mathrm{e}}$ dependence is quite different. We therefore look more closely at the various decoherence mechanisms involved, that is i$T_{1\mathrm{e}}$ or flip-flop (FF), both direct and indirect.

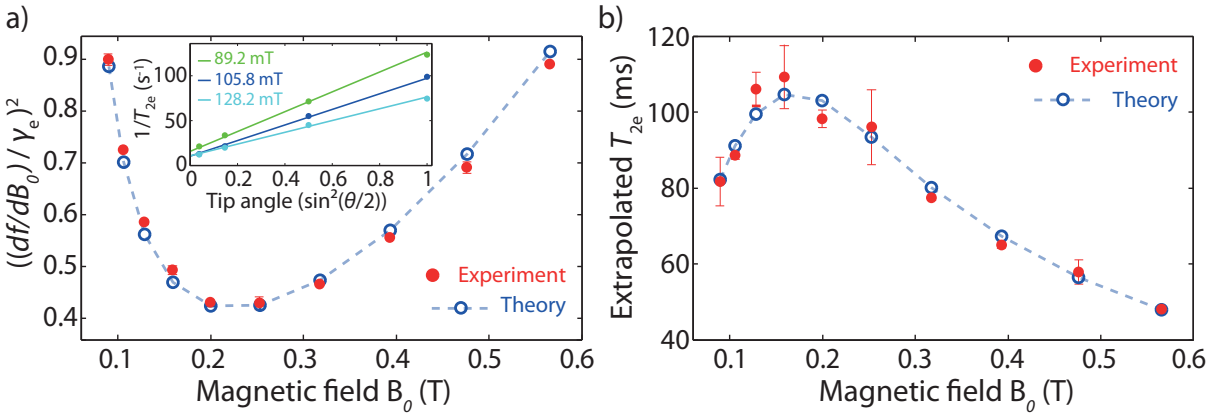


Figure 5.2: **Instantaneous diffusion (ID) and mixing.** Measurements of $T_{2\mathrm{e}}$ for the ten ESR transitions in Si:Bi [WST$^+$12]. a) ID slopes resulting from the fit of $T_{2\mathrm{e}}$ times obtained using $\pi, \pi/2, \pi/4$ and $\pi/8$ pulses as measured at 5 K for each m_I (some examples are shown in inset). The slopes vary according to $(df/dB_0)^2$, as expected from dipole-dipole interactions between neighbouring Bi electron spins. b) Extrapolated $T_{2\mathrm{e}}$ from the fit in (a) in the limit where $\theta \to 0$. The model shown in blue is defined in Eq. 5.1. In the fit, $\alpha = 0.15$ nT and $\beta = 0.023$ nT^2/Hz such that $\beta\langle . \rangle_{\pm}$ varies from 0.27 to 0.57 nT.

Indirect $T_{1\mathrm{e}}$ and FF are very similar processes from the point of view of a central donor spin. Both are ZZ interactions, their main difference being the flip rate of the coupled spin, which for i$T_{1\mathrm{e}}$ is the phonon-induced relaxation and for iFF is the coupling between donors in the ensemble. Of course, there are higher many-body correlations involved in indirect FF, but

those are second or higher order processes and thus can be neglected to first approximation. The central spin sensitivity goes as $\frac{df}{dB_0}$, however the second spin can be in any state as there is no energy or spin conservation involved, contrary to the direct FF process. This neighbour (N) spin therefore undergoes in the ensemble any allowed transition with each their own $\frac{df_{\mathrm{N}}}{dB_0}$ value. In addition, its flip rate changes with mixing as it depends on the expectation value of the transition $\langle +| \gamma_e S_x + \gamma_n I_x |-\rangle_{\mathrm{N}}$, where $|\pm\rangle$ are the two states of the transition. And again, for the indirect FF case, it is a spin pair process and thus also depends on this expectation value for the paired spin. Finally, one positive point for bismuth donors above 5 K is that $T_{1\mathrm{e}}$ is a Raman T^9 process and is independent of the transition frequency (Figure 3.4), hence does not complicate further the dependence of the flip rate as a function of the neighbour spin state.

An exact treatment of these multiple mechanisms rapidly becomes complex and some approximations are needed. First, the main contribution to decoherence comes from the electron spin, and any nuclear spin interaction term ($\gamma_n I_x$) can be neglected. Second, in the flip-flop pair, the paired electron spin expectation value is considered to be an average over all possible states, such that the flip rate for indirect FF can be grouped with indirect $T_{1\mathrm{e}}$. Finally, the direct FF rate is estimated (and measured in the next Section) to be slower than the two indirect mechanisms and is not taken into account here. Overall, the decay follows the relation:

$$\frac{1}{T_2} = \frac{df}{dB_0} \times \left(\alpha + \beta \left\langle \frac{df_{\mathrm{N}}}{dB_0} |\langle +| 2S_x |-\rangle_{\mathrm{N}}|^2 \right\rangle_{\pm} \right) \tag{5.1}$$

where $\langle . \rangle_{\pm}$ is the average over all transitions in the neighbours, α and β are phenomenological parameters. The extrapolated $T_{2\mathrm{e}}$ show quite good agreement over the entire X-band range with the above equation using the fit parameters $\alpha = 0.15$ nT and $\beta = 0.023$ nT^2/Hz.

This shows that even modest changes in $\frac{df}{dB_0}$ by about 30% at X-band have a considerable effect, increasing $T_{2\mathrm{e}}$ from 50 to 100 ms, and we can already probe the different behaviours of these decoherence mechanisms. We now turn toward the extreme case of clock transitions.

5.1.2 ^{209}Bi donor electron spin coherence at the clock transitions

The appearance of CTs can be calculated from the analytical diagonalization of the donor in Section 3.1.1 (as well in [MMNM12]). We consider the transitions that have ESR-like frequencies ($f > A$), i.e. between the eigenstates $|+,m\rangle$ and $|-,m\pm1\rangle$ that are ESR-allowed under $S_{x,y}$ or $I_{x,y}$ with a total spin change $|\Delta m| = 1$. The notation $|+\rangle$ is equal to $|F = 5\rangle$ and $|-\rangle$ to $|F = 4\rangle$ in ^{209}Bi. $\frac{df}{dB_0}$ for such ESR-allowed transitions can be expressed as a function of the spin mixing angle θ_m (defined in Section 3.1.1) of each states:

$$\frac{df}{dB_0} = \pm\gamma_n + \frac{\gamma_e+\gamma_n}{2}[\cos(\theta_{\mathrm{m}}) + \cos(\theta_{\mathrm{m}\pm1})] \tag{5.2}$$

and the condition for having a CT is therefore (considering $\gamma_n \ll \gamma_e$):

$$\cos(\theta_{\mathrm{m}}) \approx -\cos(\theta_{\mathrm{m}\pm1}) \tag{5.3}$$

Transitions involving one of the two unmixed states ($|m_S = \pm1/2, m_I = \pm9/2\rangle$) can be shown to never give a CT. The above condition is fulfilled with $\frac{\pi}{2} + \phi = \theta_m$ and $\frac{\pi}{2} - \phi = \theta_{m\pm1}$, that is the involved eigenstates must be at equal distance to a pure Bell state ($\theta_m/2 = \pi/4$), as shown in Figure 5.3. This means that CTs do not correspond to points of maximal spin-mixing (Bell states), contrary to some belief. In addition, the condition cannot be resolved for all m values. Knowing that $\cos(\theta_{\mathrm{m}}) = \frac{\Delta_{\mathrm{m}}}{\mathrm{R}_{\mathrm{m}}}$, it results in:

$$\left.\begin{array}{c} -m-(m\pm1) \geq 0 \\ m^2 > I(I+1)+\frac{1}{4} \\ (m\pm1)^2 > I(I+1)+\frac{1}{4} \end{array}\right\} \Rightarrow -I < m \pm \frac{1}{2} \leq 0 \tag{5.4}$$

A first conclusion can be made here: with an electron spin $S = 1/2$, the minimum nuclear spin number is $I = 1$. Phosphorus donors in silicon do not then have any "ESR-like" CTs (i.e. for a transition with $|\Delta F| = 1$) as its nuclear spin is only 1/2. From Eq. 3.7, we also know that

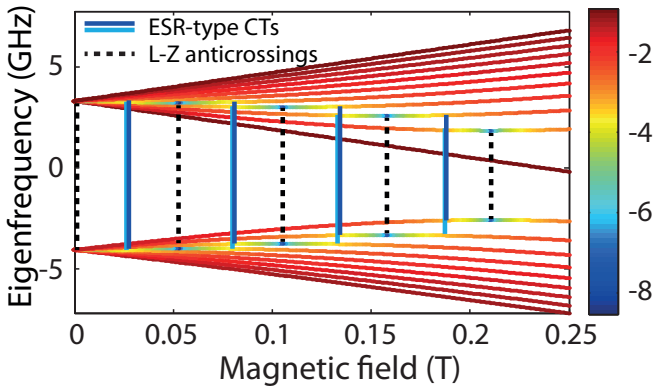


Figure 5.3: **Clock transitions in Si:^{209}Bi.** Eigenstate energies at low magnetic fields. The color scale shows the logarithmic distance to pure Bell states (Landau-Zener (L-Z) anticrossings) in the $|m_S, m_I\rangle$ basis, defined as $\log(|\theta_m/2 - \pi/4|)$ for an eigenstate $|\Phi\rangle = \cos(\theta_m/2)\left|\pm\frac{1}{2}, m\mp\frac{1}{2}\right\rangle \pm \sin(\theta_m/2)\left|\mp\frac{1}{2}, m\pm\frac{1}{2}\right\rangle$. The Bell state at 0 mT is barely visible here due to degeneracy.

the high field allowed ($|+,m\rangle \leftrightarrow |-,m-1\rangle$) and forbidden transitions ($|+,m\rangle \leftrightarrow |-,m+1\rangle$) are very close in frequency, and the difference varies weakly with field, meaning that the two transitions have similar shapes as a function of field, and hence they both have CTs at roughly the same field. From Eq. 5.3, the CT magnetic field is:

$$B_{0,\pm}^{CT} \approx -\frac{A}{\gamma_e + \gamma_n} \frac{m\Omega_{m\pm1} + (m\pm1)\Omega_m}{\Omega_{m\pm1} + \Omega_m} \tag{5.5}$$

	^{75}As ($I=3/2$)	^{121}Sb ($I=5/2$)		^{123}Sb ($I=7/2$)			^{209}Bi ($I=9/2$)			
Magnetic field (mT)	3.8	3.4	10.4	1.8	5.5	9.3	26.6	79.8	133.3	187.8
Frequency (GHz)	0.384	0.552	0.482	0.403	0.376	0.314	7.338	7.032	6.372	5.214

Table 5.1: **Summary of ESR-type magnetic-field CTs in donors in silicon.** CTs exist in pairs ($\Delta F \Delta m_F = \pm 1$) separated by less than 0.15 mT in magnetic field and 3 MHz in frequency.

In Figure 5.4, the eigen-energies, transition frequencies and the gradient $\frac{df}{dB_0}$ are plotted all for bismuth donors. The CTs are highlighted and separated into two types: ESR-like CTs (blue) as analyzed previously and summarized in Table 5.1, and NMR-like CTs (red) whose frequencies are below the hyperfine coupling strength. Not all NMR-like CTs are shown here as they span a much larger magnetic field range. There is another reason why we divide the CTs into these two categories beyond their transition frequency. For ESR-like CTs, the transition

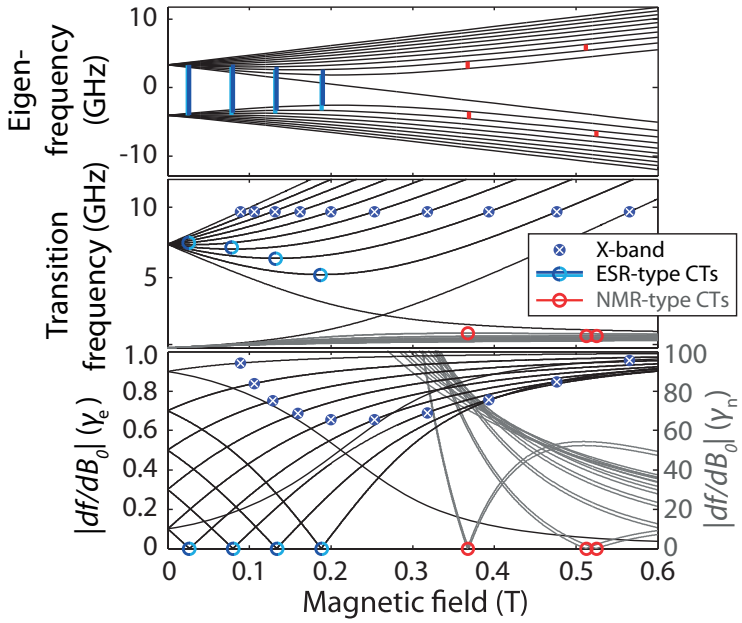


Figure 5.4: **Clock transitions in Si:^{209}Bi.** Eigenstate energies (top) at X-band magnetic fields, their corresponding ESR-type (black) and NMR-type (grey) transition frequencies between these states (middle) and the first-order magnetic field dependence (df/dB_0) of these transition frequencies (bottom). ESR-type CTs (blue lines and open circles) are found at 27, 80, 133 and 188 mT, and appear in the spectrum as doublets $\Delta F \Delta m_F = \pm 1$ separated by up to 3 MHz. NMR-type CTs are found above 300 mT (red lines and open circles).

probability is (normalized to a pure ESR transition):

$$2\left|\langle +,m|\,S_x - \frac{\gamma_n}{\gamma_e} I_x\,|-,m\pm 1\rangle\right| \approx \begin{cases} |\cos(\theta_{\mathrm{m}}/2)\cos(\theta_{\mathrm{m}-1}/2)| \text{ for } |-,\mathrm{m}-1\rangle \\ |\sin(\theta_{\mathrm{m}}/2)\sin(\theta_{\mathrm{m}+1}/2)| \text{ for } |-,\mathrm{m}+1\rangle \end{cases} \tag{5.6}$$

which is close to 1/2 and the manipulation speed of ESR-like CTs is therefore very much like an unmixed electronic spin transition. For NMR (in mixed regime), it is:

$$2\left|\langle +\text{ or } -,\mathrm{m}|\,S_x - \frac{\gamma_n}{\gamma_e} I_x\,|+\text{ or } -,\mathrm{m}\pm 1\rangle\right| \approx |\cos(\theta_{\mathrm{m}}/2)\sin(\theta_{\mathrm{m}\pm 1}/2)| \tag{5.7}$$

and the condition Eq. 5.3 is now $\cos(\theta_{\mathrm{m}}) \approx \cos(\theta_{\mathrm{m}\pm 1})$ leading to $\theta_m \approx \theta_{m\pm 1}$ which is fulfilled at high fields and therefore the transition probability is small. Hence, they behave more closely to pure NMR transitions.

Looking at the gradient $\frac{df}{dB_0}$ and the transition probability $\langle S_x \rangle$ together is important. A long coherence time with very long manipulation time is not particularly interesting. A useful metric is the product $T_2 \times \langle S_x \rangle$ which depends on the decoherence mechanism. Because the transition probability varies quite smoothly with magnetic field and never cancels, CTs are the only points in mixing regimes which provide a real advantage by this metric. Also, the Rabi frequency of nuclear spin transitions can become quite high with even a little mixing [MLH$^+$12], however any small amount of electronic spin component leads to large increase of $\frac{df}{dB_0}$ due to $\gamma_e \gg \gamma_n$.

Experimental setup and realization

Measuring the CTs requires some technical issues to be solved: a typical ESR spectrometer is built around a frequency fixed by both the cavity and partially by the bandwidth of the microwave components. The commercial X-band Bruker Elexsys spectrometer used in the other experiments here worked from 8 to 11 GHz, with a cavity resonance frequency around 9.7 GHz. At 7 GHz, the signal loss due to bandwidth was close to 15 dB which could be compensated by pre-amplification with a low-noise amplifier working around this frequency. The frequency of the resonator can be dictated by its geometry and design, so, to perform experiments at one of the CTs, resonators were designed with the COMSOL® Multiphysics eigenfrequency solver using a split-ring model (Figure 5.5(a)).

Split-ring resonators (SRR) [MSZ00, GBM02, ABG$^+$05] are similar to lumped-element *LC* circuits as there is a clear separation of the electric and magnetic components of the eigenmodes. The electric field is confined here between one or many gaps of small dimensions ($\approx$ 1 mm) corresponding to a capacitor C, and the magnetic field mode is concentrated within a loop that corresponds to an inductance L (see Figure 5.5(a,b)). The interest of such design for ESR is that there is a clear space (4–5 mm diameter hole) within the loop to add the sample and the filling factor can be large as all the magnetic field is confined there. In addition, the resonance frequency can be tuned over 1–2 GHz by only changing the gap size and the hole diameter (Figure 5.5(c)), without changing any of the outer dimensions that can then be fixed to fit within

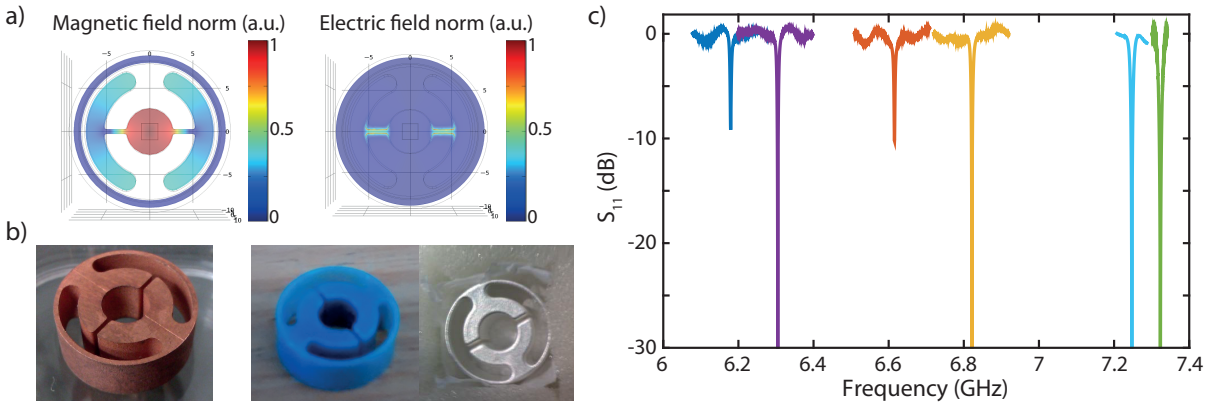


Figure 5.5: **Split-ring resonators.** a) COMSOL® simulations of magnetic and electric fields in a 3D split-ring cavity for an eigenfrequency close to 7 GHz. The magnetic field is concentrated in the central hole whereas the electric field is confined in the gaps. b) Left: resonator machined from oxygen-free copper. Right: resonator 3D printed in ABS plastic (blue color) and then coated with a layer of copper and silver. c) Resonance frequency of split-ring resonators of various dimensions.

a supporting structure. The SRRs can be quite sensitive to external parameters: the sample dielectric constant, its position within the resonator or the temperature all affect the frequency which can move by a few 100 MHz. This problem can also be beneficial as this makes the frequency somewhat tunable within this range. SRRs can simply be machined out of oxygen-free copper which confines the microwaves well. We also developed a second method consisting in 3D printing the resonators in plastic (ABS) and then coating them with a metallic layer of copper and silver ($10 - -100\ \mu$m). This has the benefit of being cheap, they can be manufactured in bulk, and lower frequencies ($\approx$ MHz) can penetrate the thinner layer which can be useful for magnetic field modulation in continuous-wave ESR experiments. With these two techniques, we obtain Q-factors between 500 and 2000.

Using a SRR with resonance frequency at 7.0317 GHz (corresponding to the CT at 80 mT), we perform ESR spectroscopy of the ^{209}Bi donor as shown in Figure 5.6(a). Starting from a high frequency, the field-sweep electron spin echo-detected spectrum shows four peaks, two for each high field allowed ($|5,-1\rangle \leftrightarrow |4,-2\rangle$) and forbidden transitions ($|4,-1\rangle \leftrightarrow |5,-2\rangle$) as the transition frequency has a quadratic dependence on magnetic field and thus crosses the cavity resonance twice. The linewidth can be seen to significantly increase at the CT, which is expected

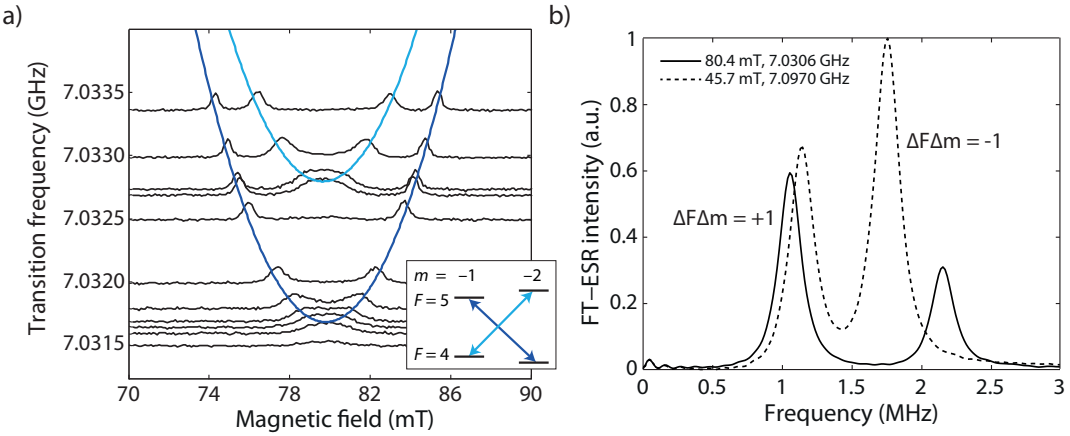


Figure 5.6: **ESR spectra for ^{209}Bi donors measured around a CT.** a) Electron spin echo-detected magnetic field sweep near the 7.0317 GHz CT in ^{28}Si:^{209}Bi [WTG+13] using the split-ring resonator design. Dark and light blue are the high field allowed and forbidden transitions, respectively. b) Fourier-Transform ESR spectrum far (45.7 mT) and close (80.4 mT) to the CT. The two peaks are also from the high field allowed and forbidden transitions which are separated by $2\gamma_n B_0$.

as $1/\frac{df}{dB_0} \to \infty$. Obviously, it does not become infinitely large as it is then limited by the second order derivative $\frac{d^2f}{dB_0^2}$. The fact that the spin linewidth in the frequency domain did not actually increase can be measured using Fourier-Transform ESR (Figure 5.6(b)). This technique simply consists of taking the Fourier transform of the echo signal while being slightly off resonance. The frequency linewidth is indeed measured to be 270 kHz both away and slightly off the CT. The linewidth can be related to a spread in the free parameters in the Hamiltonian, B_0 and A, by (to first order):

$$\Delta F = \frac{df}{dB_0}\Delta B_0 + \frac{df}{dA}\Delta A \xrightarrow{\text{CT}} \frac{df}{dA}\Delta A \tag{5.8}$$

The linewidth can therefore be attributed to a distribution in the hyperfine constant $\Delta A \approx 60$ kHz, consistent with ENDOR measurements (Section 3.1.2). It should be mentioned that this reduction in the linewidth from about 400 kHz at X-band has the added benefit to increase spin manipulation fidelity. As the CT removes most of the sensitivity to magnetic field, uncertainties in the field value become irrelevant, hence enabling a precise measurement of the mean hyperfine value from the measured CT frequency: $A = 1.475169(7)$ GHz. In the simulation, we used $\gamma_e = 27.997(1)$ GHz.T^{-1} [Feh59a] and $\gamma_n = 6.9(2)$ MHz.T^{-1}.

Electron spin decoherence in ^{28}Si

In Figure 5.7(a), we measure T_{2e} in ^{28}Si:^{209}Bi at the 7.0317 GHz CT. With a donor concentration $[\mathrm{Bi}] = 3.6 \times 10^{14}$ cm^{-3}, we obtain a coherence time of 2.7 s using only a Hahn echo sequence. This is far beyond the ID limit for an electron spin in the high field regime, and is measured directly with π-refocusing pulses and no extrapolation. This corresponds to an improvement of nearly two orders of magnitude in the coherence time; with the duration of the π-pulse being 100 ns, the total number of single-spin operation is $10^7 - 10^8$, the highest ever measured, to the best of our knowledge, for any quantum system without dynamical decoupling sequences.

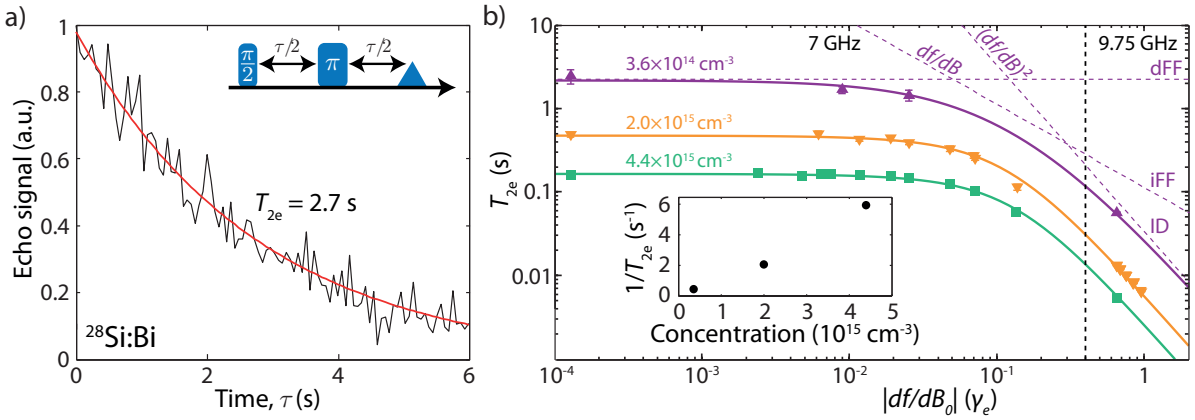


Figure 5.7: **Decoherence near and at the CT in ^{28}Si:^{209}Bi.** a) T_{2e} at 4.3 K with a ^{209}Bi concentration of 3.6×10^{14} cm^{-3}. The decay is exponential with $T_{2e} = 2.7$ s. b) T_{2e} measurements at 4.8 K, for three different donor concentrations, showing a strong dependence on $\frac{df}{dB_0}$. Measurements close to $\frac{df}{dB_0} = \gamma_e$ were taken using the ten X-band ESR transitions, while the remaining points were taken close to the CT. For each concentration, the dependence on $\frac{df}{dB_0}$ is modeled using contributions from ID, indirect and direct flip-flop (iFF, dFF) processes, as shown separately as dashed lines for the lowest donor concentration. Inset: the limit of $1/T_{2e}$ when approaching the exact CT as a function of donor concentration, showing a nearly linear dependence, as expected for direct flip-flop.

While this improvement is considerable, why is it not longer? The CT is a point of fast variation in $\frac{df}{dB_0}$, varying by nearly two orders of magnitude when changing the resonance frequency by less than 5 MHz, which allows a study of the various decoherence mechanisms at work. In Figure 5.7(b), T_{2e} is plotted over three orders of magnitude in $\frac{df}{dB_0}$ using values from both X-band and near the CT. The value of the gradient used at the CT is not zero but takes

into account the second derivative and the spin linewidth to find a lower bound. Measurements were realized on three different samples with concentrations $[\mathrm{Bi}] = 3.6 \times 10^{14}, 2.0 \times 10^{15}$ and 4.4×10^{15} cm^{-3}, and below 5 K so there is no $T_{1\mathrm{e}}$ contribution to the coherence time.

The coherence time is first limited by ID which is quadratic in $\frac{df}{dB_0}$ and becomes negligible for $\frac{df}{dB_0}$ below $0.1\gamma_e$. Then, indirect FF is the next dominant mechanism but is also suppressed as it is linear in $\frac{df}{dB_0}$ (Eq. 5.1). The final limit to decoherence is direct FF: this is a $XX+YY$ process and therefore γ_e is not renormalized to $\frac{df}{dB_0}$. There is some effect of spin mixing as the expectation value of X is about 1/2 at the CT, however if there existed a point where this value was 0, then that would also mean that the manipulation time would be infinite too. The only way for direct FF to be damped is to reduce the spin concentration (i.e. the dipolar interaction strength) as shown in the inset of Figure 5.7(b). Yet, even in an ideal quantum computing device, the spin concentration is set by the qubit density, and so a better way to extend this limit is to introduce frequency detuning between the various donor spins to dampen the flip-flop process, as was demonstrated in [TTM$^+$11] using a magnetic field gradient. In the case of a CT, such gradient would however also detune some of the spins from the CT magnetic field value and therefore is not viable. Short-range magnetic field gradients could still be used, such as provided by ^{29}Si nuclear spins, as the maximum detuning from the CT remains limited. Other alternatives such as the use of electric field gradients (via Stark Shift, see Chapter 6) maybe also be suitable. For large scale devices however, gradients present their own additional complexity as detuning results in frequency crowding and more difficult manipulation.

At 2.7 s, $T_{2\mathrm{e}}$ is already beyond the (1 s) limit of spectral diffusion seen at X-band arising from the remaining 50 ppm of ^{29}Si in these isotopically purified ^{28}Si samples (see Figure 3.6). This means that the CT also reduced this contribution, as expected given that spectral diffusion is a ZZ process. In the next Section, we turn to probing the behaviour of central spin decoherence from the ^{29}Si bath in $^{\mathrm{nat}}$Si for both ESR and NMR-like transitions close to CTs. We will show that in certain regimes the classical $\frac{df}{dB_0}$ model is insufficient to describe the decoherence times, and that the exact quantum evolution must hence be considered.

5.2 Donor electron - ^{29}Si bath interactions near CTs

In ^{nat}Si, interaction with the bath can be thought of classically as a fluctuating magnetic environment. In this case, the decoherence behavior would simply follow $\frac{df}{dB_0}$, and going to the clock transition (CT) should considerably reduce the effect of the ^{29}Si without needing isotopic purification. In Figure 5.8(a), a measurement of ^{nat}Si:^{209}Bi at the CT is shown with $T_{2e} = 93$ ms, compared to 0.8 ms at X-band. The sample had a donor concentration $[\text{Bi}] = 1 \times 10^{15}$ cm^{-3} and the temperature was below 5 K such that $T_{1e} \gg 1$ s. This corresponds to an improvement of two orders of magnitude, so the CT does indeed greatly enhance the coherence.

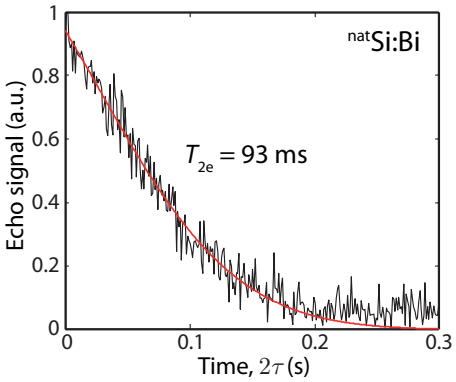


Figure 5.8: **CT in ^{nat}Si:^{209}Bi.** Hahn echo decay in ^{nat}Si with Gaussian behaviour.

Is this improvement expected from the ratio of $\frac{df}{dB_0}$? The mean value of the gradient at the CT considering the spin linewidth in ^{nat}Si (standard deviation of 2.1 G) is about $10^{-3}\gamma_e$, therefore the observed improvement is not enough if the behavior was indeed linear. At this donor concentration, T_{2e} should be at least 1 s in isotopically purified ^{28}Si considering Figure 5.7(b), hence the source of the decay is still clearly from the ^{29}Si bath. In order to answer this question, it is necessary to look more closely at the interaction with the spin bath.

5.2.1 Mixing effect on bath dynamics

To understand the spin dynamics, we start once again from the pseudo-spin picture described in Section 4, with the major difference that the interaction between the donor and the bath must

be expressed in the donor basis, restricted to the states $|\pm\rangle$ of the measured transition. Any Z interaction is renormalized by $P_\pm = \langle\pm|S_z|\pm\rangle$, and it is straightforward to see that $\gamma_e(P_+ - P_-) \approx \frac{df}{dB_0}$. The nuclear operator I_z is not present here as the coupling to the ^{29}Si bath is through the hyperfine interaction with the donor electron only. The parameters $\delta\omega_\pm$ (detuning) and $\Omega_\pm$ (spin pair coupling) in the pseudo-spin picture can be rewritten such that:

$$\delta\omega_\pm = P_\pm \Delta A \tag{5.9}$$

$$\Omega_\pm = C_{12} + P_\pm \frac{A_{e1}A_{e2}}{\omega_e} \tag{5.10}$$

Hence, α which characterizes the entanglement between the central spin and the bath in Eq. 4.17 becomes:

$$\alpha = \frac{C_{12}\Delta A(P_+ - P_-)}{4} \frac{\sin^2(\omega_\Sigma t) - \sin^2(\omega_\Delta t)}{\omega_\Sigma^2 - \omega_\Delta^2} \tag{5.11}$$

where $\omega_{\Sigma,\Delta} = \frac{\sqrt{C_{12}^2+P_+^2\Delta A^2} \pm \sqrt{C_{12}^2+P_-^2\Delta A^2}}{4}$. In order to clearly extract the dependence in $P_\pm$, we consider separately the two cases where $C_{12} \gg P_\pm\Delta A$ (weak coupling to CS) and $C_{12} \ll P_\pm\Delta A$ (strong coupling to CS), and then expand the equation to first order in the dominant parameter. We also consider that $\omega_\Delta \ll \omega_\Sigma$, i.e. $|P_+| \approx |P_-|$, in order to remove the evolution in $\sin^2(\omega_\Delta t)$ which is too slow. This is valid in a large number of cases such as pure ESR $P_+ = -P_-$, pure NMR $P_+ = P_-$, and close to a CT $P_+ = P_- \to 0$. First, if $C_{12} \gg P_\pm\Delta A$, then α simplifies to:

$$\alpha \approx \frac{\Delta A}{C_{12}}(P_+ - P_-)\sin^2\left(\frac{C_{12}}{2}t\right) \tag{5.12}$$

The hyperfine-mediated term is disregarded here, considered to be weaker than C_{12}, which is especially true as $|P_\pm| \ll 1/2$ close to a CT. To obtain the final decay, calculations must be realized over all the spin pairs and configurations according to the CCE. It is known both numerically [WD06, BKM$^+$12] and experimentally [AIIY04] that a Hahn echo measurement limited by ^{29}Si spectral diffusion always gives a Gaussian (or near-Gaussian) decay. From CCE calculations, this shape emerges from the product of all pairs. This was also observed here in

Figure 5.8 and in the previous Chapter in Figure 4.5(b) and Figure 4.10(a). This means that the product over all spin pairs, which is hard to solve analytically, can be phenomenologically written as:

$$-(2t/T_2)^2 \equiv -2\int\int \alpha^2 f(C_{12},\Delta A)dC_{12}d\Delta A \tag{5.13}$$

where $f(C_{12},\Delta A)$ is the probability density function for the values of C_{12} and ΔA for the spin pairs in the bath. This sum (product of exponentials) is normally discrete however we use continuous notations for simplicity. Combining both Eq. 5.12 and Eq. 5.13 gives:

$$-(2t/T_2)^2 \equiv -2\,(P_+ - P_-)^2 \int\int \frac{\Delta A^2}{C_{12}^2}\sin^4\left(\frac{\mathrm{C_{12}}}{2}\mathrm{t}\right)\mathrm{f(C_{12},\Delta A)dC_{12}d\Delta A} \tag{5.14}$$

$$\Rightarrow \frac{1}{T_2} \propto |P_+ - P_-| \approx \left|\frac{1}{\gamma_e}\frac{df}{dB_0}\right| \tag{5.15}$$

Hence, in the case where $C_{12} \gg P_{\pm}\Delta A$, decoherence would follow $\frac{df}{dB_0}$ which is contrary to the observed behaviour in Figure 5.8. Intuitively, this also means that when the dipolar coupling within the spin pair dominates, the bath behaves independently of the donor states and can be treated as a classical fluctuating magnetic field. We now turn to the other case where $C_{12} \ll P_{\pm}\Delta A$. In this case, α is now:

$$\alpha \approx \frac{4C_{12}}{\Delta A}\frac{P_+ - P_-}{(|P_+| + |P_-|)^2}\sin^2\left(|\Delta\mathrm{A}|\frac{(|\mathrm{P_+}| + |\mathrm{P_-}|)}{4}\mathrm{t}\right) \tag{5.16}$$

The hyperfine-mediated term was not neglected here but cancels itself during the calculations. Following the same ad hoc solution for the cluster products is not directly possible in this case as $|P_+| + |P_-|$ modifies the evolution in the $\sin^2$ term. However, the Gaussian behaviour is supposed to be valid for all times t and one can simply re-normalize the time to $(|P_+| + |P_-|)t$ such that:

$$\frac{1}{(|P_+| + |P_-|)T_2} \propto \frac{|P_+ - P_-|}{(|P_+| + |P_-|)^2} \Rightarrow \frac{1}{T_2} \propto \frac{|P_+ - P_-|}{|P_+| + |P_-|} \approx \frac{1}{|P_+| + |P_-|}\left|\frac{1}{\gamma_e}\frac{df}{dB_0}\right| \tag{5.17}$$

This solution still involves the classical $\frac{df}{dB_0}$ sensitivity of the central spin, however an additional component from its "back-action" on the bath now appears. At the 7.0317 GHz ESR-like CT, we have $P_{\pm} \approx 0.05$ hence the enhancement in T_{2e} is damped by a factor of 10, leading to the measured two orders of magnitude increase in Figure 5.8.

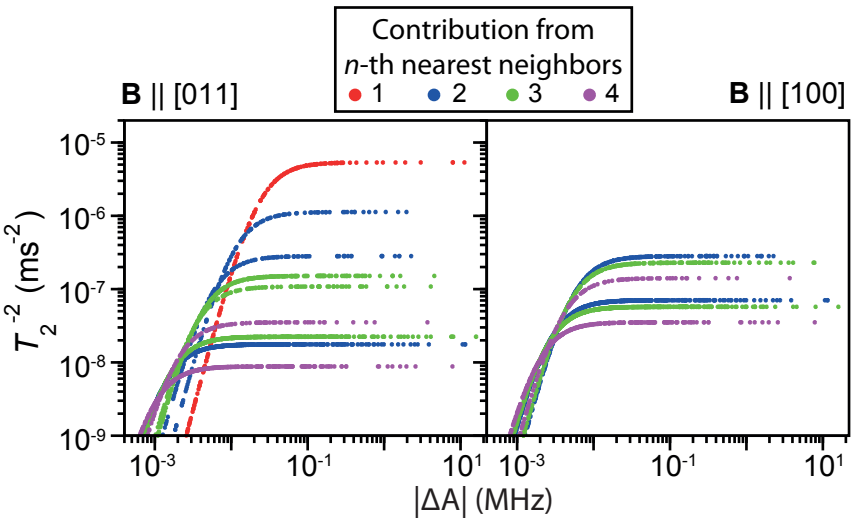


Figure 5.9: **Individual spin pair contribution.** Individual contribution of each spin pair in the bath to the total $1/T_2^2$ near the 7 GHz CT, calculated using CCE [BWMM14] for two magnetic field orientations. The spin pairs are distinguished by their ^{29}Si-^{29}Si distance. The dominant pairs are those for which $|P_{\pm}\Delta A| \gg C_{12}$.

This model seems to agree well with the experiment, however some of the hypotheses must be tested. Exact numerical calculations of the decays can be realized with CCE (see [BWMM14]) starting directly from the interacting Hamiltonian. The parameters C_{12} and ΔA for each pair are calculated from the dipolar interaction and using the Kohn-Luttinger electronic wave function for the hyperfine values. From this, the contribution to T_2 from each spin pair is calculated and plotted in Figure 5.9 as a function of $|\Delta A|$. The decay rate can be seen to be maximum for $|\Delta A| > 10$ kHz, that is when it is much larger than C_{12}. So this approximation seems quite valid. T_2 appears to be defined mainly by the high $|\Delta A|$ pairs, but interestingly, the dependence saturates and so becomes independent of the $|\Delta A|$ value. This observation enhances the validity of the numerical simulation which, being based on calculated and not measured hyperfine values, does not require them to be exact. Each pair is classified in the figure by the

distance (first to fourth nearest neighbours) between its two ^{29}Si spins, for the two orientations [011] and [100] with respect to the static magnetic field. When B_0 is parallel to [100], the field is at the magic angle (54.7°) with the first nearest neighbours; the dipolar interaction disappears and so does its contribution to T_2. For other orientations, the nearest neighbour coupling dominates and defines the decay time. Looking at Eq. 5.16, if T_2 does become independent of $|\Delta A|$ after averaging, it makes sense that a large decay rate comes with the strongest dipolar coupled pairs. Finally, in the example of $B_0 \parallel [011]$ in Figure 5.9, the origin of the decay can be reduced to those few nearest neighbours (NN) with high $|\Delta A|$ value, such that $1/T_2 \propto C_{12}^{NN}\sqrt{N}$, where N is the number of such pairs ($N \approx 100-200$).

5.2.2 Experiments: model test

Equation 5.17 can be further tested by looking at different regimes apart from right at the CT, as long as $|P_+| \approx |P_-|$. The difference between $\frac{df}{dB_0}$ and the equation is shown in Figure 5.10(a) for a large range of magnetic fields in ^{209}Bi, while in (b), the three regimes of high field ESR, NMR and the ESR-like CT are illustrated by their bath pseudo-spin Bloch spheres. While all regimes have $|P_+| \approx |P_-|$, they each have different signs or values for $P_\pm$ leading to different trajectories for the pseudo-spin evolution. For ESR, the opposite sign for the two donor states lead to fast divergence in path and therefore fast decoherence. For NMR and ESR-like CTs, P_+ and P_- have the same sign and therefore a less divergent pseudo-spin evolution, however the speeds of the two trajectories are slightly different leading to the coherence decay.

In addition to both the ESR-like CT and the simple high field ESR T_{2e}, we perform measurements on NMR transitions with a range of $\frac{df}{dB_0}$ values. At X-band between 200 MHz and 1 GHz, the accessible NMR transitions show large variations in $\frac{df}{dB_0}$ and thus provide a good test-bed for the model. They are measured using the ENDOR sequence described in Figure 2.6(c). Experimental results are shown in Figure 5.11 along with both pure numerical calculations (CCE) and from the analytical Eq. 5.17 which is scaled to match the data. The agreement is quite astounding as any small variations from the classical $\frac{df}{dB_0}$ are accounted for by the additional $|P_+| + |P_-|$

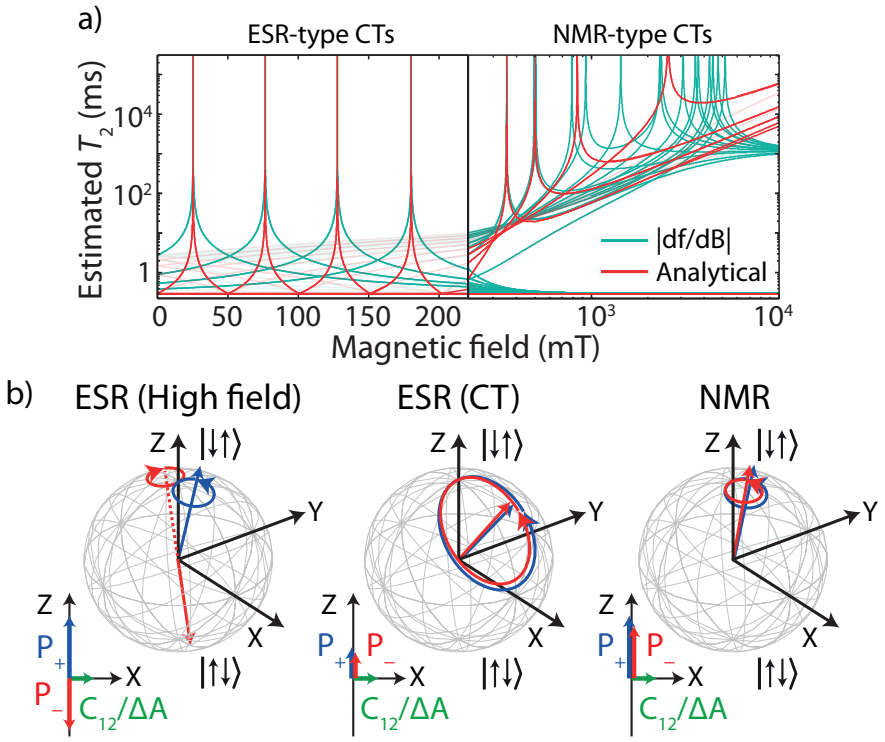


Figure 5.10: **Pseudo-spin and mixing in ^{nat}Si.** a) Difference between the field-frequency gradient $\frac{df}{dB_0}$ and Eq. 5.17 ("Analytical") as a function of magnetic field for a variety of allowed transitions in ^{nat}Si:^{209}Bi. The curves are plotted as T_2 by using a scaling factor estimated from CCE calculations of the integral in Eq. 5.13 [BWMM14]. Transitions with no CT are shown only faintly. At very high fields, T_2 of NMR transitions are eventually limited by the donor nuclear spin-^{29}Si dipolar coupling. b) Pseudo-spin illustration of the evolution of the bath states in various spin mixing regimes. At both CTs and NMR transitions, bath trajectories correlated with the upper and lower central spin states follow similar trajectories and hence decoherence is suppressed compared to ESR transitions. However, at ESR CTs, $|P_\pm| \simeq 0.05$ leads to a larger trajectory and proportionately shorter T_2 values relative to some NMR transitions.

term, and this over three orders of magnitude in $\frac{df}{dB_0}$ and corresponding to three quite different types of magnetic resonance transition.

In conclusion, the deduced formula seems quite robust and valid over a larger range of mixing regimes. Instead of a single-sided effect of the bath on the donor coherence, there is now a back-action of the donor on its environment, expressed through the $|P_+| + |P_-|$ term. Varying free parameters of the Hamiltonian to alter the behaviour of the spin transitions is therefore a powerful method to obtain informations on a system and its environment.

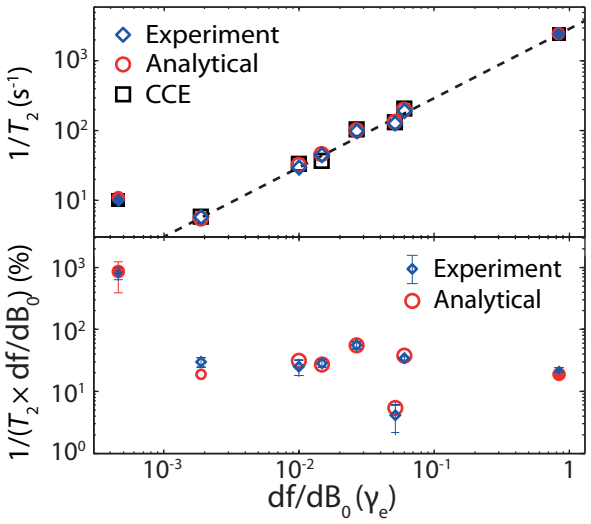


Figure 5.11: **Test of Eq. 5.17 in different regimes.** Comparison between theoretically predicted and measured T_2 in ^{nat}Si:^{209}Bi for various transitions, showing remarkable agreement across a wide range of $\frac{df}{dB_0}$. The label "analytical" refers to Eq. 5.17. Measurements were made at 4.8 K using ESR with a microwave frequency of 9.77 and 7.03 GHz (filled symbols), ENDOR between 200 MHz and 1 GHz (empty symbols), at magnetic fields between 100 and 450 mT. The dashed line is a guide to the eye, linear in $\frac{df}{dB_0}$. In the lower panel, the decay rates are normalized by $\frac{df}{dB_0}$ to highlight the effect of $|P_+| + |P_-|$, and shown relative to the case when $|P_+| = |P_-|$.

5.3 Conclusion

In this Chapter, the sensitivity to magnetic field of a measured spin transition was efficiently tuned all the way to zero, to first order. In ^{28}Si samples, we were able to obtain electron spin coherence times up to 2.7 s using CTs for a simple Hahn echo, and more importantly, a ratio of coherence over spin manipulation time of $\approx 10^8$, way above error-correction thresholds ($10^4 - 10^5$). In ^{nat}Si, in addition to a two orders of magnitude increase in coherence times, the tuning of the magnetic field sensitivity allowed for probing the interaction between the donor and the ^{29}Si spin bath.

Further experiments could be realized by combining both the advantage of dynamical decoupling sequences and the CTs. In ^{nat}Si, the limit even at 0.1 s is still due to the remaining coupling with the ^{29}Si, therefore DD is still quite viable. For probing the bath dynamics, the CT reduces the detuning withing the bath which can flip-flop at the "undamped" nuclear-nuclear

dipole rate, and combined with DD, the CT coherence time can be expected to become longer than the bath memory, taking the overall donor-bath system into a more classical Markovian regime. In ^{28}Si, the use of DD at the CT might not be as useful as the coherence is limited by direct flip-flop between the donors, requiring sequences similar to WAHUHA but tailored for a weak Z interaction (if possible).

CHAPTER 6

Manipulating the hyperfine interaction via the Stark shift

Until now in this thesis, spin decoherence was studied as originating from magnetic sources of noise, mostly spins in the environment, however, it may also result from fluctuations in the local electric field surrounding a donor. Coupling of donor spins to the electric field can occur via the so-called Stark effect which modifies both the electron g-factor and the hyperfine interaction, though it is a weak effect: indeed, this is one of the main reason behind the long spin coherence times in ensembles of donors in silicon. Nevertheless, the disadvantage of the weak Stark effect is that donors cannot readily be manipulated with electric fields, which would help in realizing many scalable quantum computing architectures. Indeed, most schemes involve nano-scale devices with many qubits that require local and independent control; electric fields are then preferred over magnetic fields as they are easier to confine in space, which in the long term may result in less power dissipation. The issue of decoherence from electric field fluctuations is also more relevant for donors in nano-devices, where the donor is much closer to an interface with local electric charges or electrostatic gates. In this case, it could become interesting to investigate clock transitions not insensitive to magnetic field but to the electric field.

In this Chapter, I therefore characterize the sensitivity of group V donors to an external electric field to estimate its possible importance to decoherence, and then demonstrate partial spin control by combining DC electric fields and RF magnetic fields as was proposed by Kane in his concept for a nuclear spin quantum computer in silicon.

6.1 Background

6.1.1 A scalable architecture for donors in silicon

Magnetic resonance takes advantage of the Zeeman interaction to coherently control spins with magnetic fields. However, the donor Hamiltonian has in addition to the electron and nuclear Zeeman terms a hyperfine interaction A. While it is typically considered a constant parameter, variation in the coupling results in changes in the Hamiltonian and therefore is suitable for manipulating the donor spins. The hyperfine interaction is dipolar in nature, resulting from the overlap of the electronic wavefunction with the nuclear point-like dipole. It is not sensitive to external magnetic fields, but to change in the local configuration of the donor that alters the wavefunction. While strain is one possible way to achieve this [WF61, DHB$^+$11], the most practical solution is to apply electric fields which intuitively is equivalent to pulling the electron away from the donor as illustrated in Figure 6.1. The response of the spin to changes in the wavefunction is called the Stark effect, and is due to variations in the hyperfine coupling as mentioned, but also a shift in the electron g-factor though it is typically much weaker. This affects directly the transition frequencies of the donor system which can therefore be tuned by the application of electric fields, i.e. a voltage on a nearby electrostatic gate.

This phenomenon was a central feature in the Kane proposal (see Section 1.3 and Figure 1.1). By combining global control by magnetic resonance, e.g. by having the device in a cavity, and local electrostatic gates to tune desired spins on and off resonance for local control, a scalable architecture could be realized without the need for arrays of microwave lines on the chip. In addition, the electric field can be also used to couple pairs of nearby donors by shifting

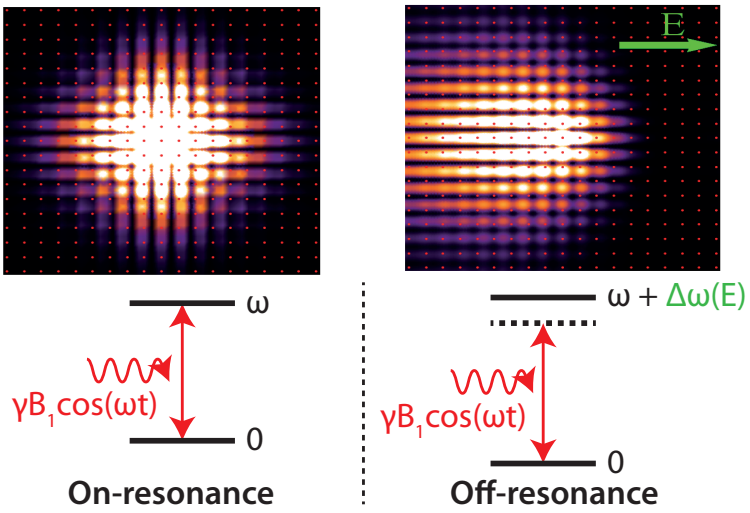


Figure 6.1: **Scalable donor architecture.** Electronic wavefunction of a ^{31}P donor in a silicon lattice. The application of an electric field E stretches the wavefunction away from the nucleus at the center, mainly modifying the hyperfine interaction [PWU$^+$14]. An external magnetic excitation is shifted on or off resonance as the transition frequency is modified ($\Delta\omega(E)$).

both electron wavefunctions and increasing the exchange interaction between the two. Though research in this domain has long since evolved from the Kane paper, especially regarding single-spin measurement methods [PTD$^+$12, PTD$^+$13], the proposal still provides a good method for the local manipulation of spins. In the original paper, the nuclear spin is used as the qubit, mostly due to the measurement mechanism, and a shift in the hyperfine interaction affects in a similar way both the electron and nuclear spin transitions. Other versions of the Kane proposal [HHF$^+$05] have preferred using the electron spin as the qubit due to its faster manipulation time, however there is a real unanswered question here: the faster control is only usable if the spin's resonance frequency can be tuned by a larger amount than the manipulation speed, in order to have frequency selectivity between resonant and non-resonant spins. Since the Kane proposal, many theoretical papers [Fri05, RWB$^+$07, RPB$^+$09, PWU$^+$14] have successively attempted to estimate the intensity of the Stark shift. A single experiment by Bradbury *et al.* in 2006 [BTS$^+$06] gave the first measurement of the Stark effect for ^{121}Sb donors, followed later by a study in ^{75}As [LSL$^+$14], however it remains unknown for other donors. It is therefore important to properly characterize this tuning mechanism in order to choose an optimal archi-

tecture using donors in silicon, including whether to choose a nuclear or an electron spin as the main qubit, and determine points at which the electric field sensitivity can be minimized.

In this Chapter, the Stark shift is characterized for all four Group V donors, and then used to demonstrate tuning as a switching technique for the response of ^{121}Sb donor nuclear spins to an external magnetic field. Finally, a solution for coherent manipulation is proposed using microwave electric fields, removing the need for AC magnetic fields altogether.

6.1.2 Stark shift theory

The theory of the Stark shift has been mainly investigated using Effective Mass Theory (EMT) [SRCK04, Fri05, PWU$^+$14] and to a lesser extent with ab-initio calculations [RPB$^+$09]. While the latter is highly numerical and offers mainly qualitative results, EMT can provide good physical understanding of the effect for which the key points are briefly summarized here.

Group V dopants in silicon are substitutional impurities, that is they replace one silicon atom in the lattice and provide one additional electron. At low temperature, this electron is bound to the donor resulting in a system very similar to a hydrogen molecule, with the main difference that the environment is now the silicon lattice. It is therefore usual to use the "scaled hydrogen model" to obtain the energy levels of the donor, mainly by replacing the dielectric constant and mass in vacuum by their effective value in the material. Using this transformation, EMT provides a description of the electron wavefunction bound to the donor in its ground state:

$$\psi(\mathbf{r}) = \sum_{i=1}^{6} \alpha_i \phi_i(\mathbf{r}) F_i(\mathbf{r}) \tag{6.1}$$

The wavefunction is decomposed here in wavefunctions along the 6 valleys of the conduction band in silicon with, for each valley i (along the directions $\pm x, \pm y, \pm z$): α_i the weight, $\phi_i(\mathbf{r})$ the Bloch wavefunction due to the lattice periodicity such that $\phi_i(\mathbf{r}) = u_i(\mathbf{r})e^{i\mathbf{k_i}\cdot\mathbf{r}}$ where $u_i(\mathbf{r})$ has the periodicity of the crystal and $\mathbf{k_i} = k_0\mathbf{i}$ with k_0 the valley minimum momentum along the direction $\mathbf{i}$, and finally $F_i(\mathbf{r})$ is a slow varying (compared to the lattice constant) envelope

wavefunction.

The envelope wavefunctions $F_i(\mathbf{r})$ have equal eigenvalues under a hydrogen-like Hamiltonian (kinetic energy and Coulomb attraction) leading to a six-fold degeneracy of the ground state, which is lifted however when taking into account the real impurity potential. Finding this potential and correspondingly the exact form for $F_i(\mathbf{r})$ is one of the main challenge in EMT. While on the one hand ^{31}P is very similar to a silicon atom, ^{209}Bi is on the other hand quite different (mass, binding energy, ...) and therefore corrections to the standard hydrogen potential become more complex. A good model encompassing all donors was presented only recently by Pica *et al.* in [PWU$^+$14]. Due to the diamond structure for the silicon lattice, a donor at a substitutional site has tetrahedral symmetry which is not affected by the presence of the donor [SRCK04], hence the non-degenerate valley ground states must still follow this symmetry. The wavefunctions are therefore combinations of the valleys with weight α that can be divided into three groups with equal eigenvalues:

$$\text{Singlet } (1\text{sA}_1) \begin{cases} \alpha_{\mathbf{g}} = \frac{1}{\sqrt{6}}(1,1,1,1,1,1) \end{cases} \tag{6.2}$$

$$\text{Doublet } (1\text{sE}) \begin{cases} \alpha_{\mathbf{r}} = \frac{1}{\sqrt{12}}(-1,-1,-1,-1,2,2) \\ \alpha_{\mathbf{s}} = \frac{1}{2}(1,1,-1,-1,0,0) \end{cases} \tag{6.3}$$

$$\text{Triplet } (1\text{sT}_2) \begin{cases} \alpha_{\mathbf{x}} = \frac{1}{\sqrt{2}}(1,-1,0,0,0,0) \\ \alpha_{\mathbf{y}} = \frac{1}{\sqrt{2}}(0,0,1,-1,0,0) \\ \alpha_{\mathbf{z}} = \frac{1}{\sqrt{2}}(0,0,0,0,1,-1) \end{cases} \tag{6.4}$$

The wavefunctions ψ corresponding to each vector α form an eigenbasis. The singlet 1sA_1 has the lowest energy level by far, forming the ground state of the donor. All spin measurements are realized in this state. In addition, it is the only wavefunction that has non zero electronic density at the nuclear site and therefore has a hyperfine interaction with the nuclear spin. 1sE and 1sT_2 have similar energies.

The application of an electric field $\mathbf{E}$ along some particular direction first results in break-

ing of the tetrahedral symmetry, and therefore mixing between the various valley states. These states are coupled by the electric dipole moment $e\mathbf{E}.\mathbf{r}$, where e is the elementary charge, and changes to the wavefunctions can be estimated by perturbation theory. The first order perturbation to the $1sA_1$ eigenenergy is $\int \langle \psi_g(\mathbf{r}) | e\mathbf{E}.\mathbf{r} | \psi_g(\mathbf{r}) \rangle d\mathbf{r}$ and is equal to zero by symmetry. The second order perturbation shift in energy is $\sum_{i \neq g} \int \frac{|\langle \psi_g(\mathbf{r}) | e\mathbf{E}.\mathbf{r} | \psi_i(\mathbf{r}) \rangle|^2}{E_g - E_i} d\mathbf{r}$ which is non-zero. Therefore, the ground state eigenfunction becomes:

$$|\psi_g(\mathbf{r})\rangle \rightarrow |\psi_g(\mathbf{r})\rangle \left(1 + \frac{1}{2}\eta_A E^2\right) + ... \tag{6.5}$$

where $E = \|\mathbf{E}\|$, η_A is a negative constant, and ... are terms using the higher energy states. The hyperfine interaction A is proportional to $|\psi_g(\mathbf{r}=0)|^2$ and the change due to the electric field can be written as:

$$\frac{\Delta A}{A} = \frac{|\psi_g(\mathbf{r}=0, E \neq 0)|^2}{|\psi_g(\mathbf{r}=0, E=0)|^2} - 1 = \eta_A E^2 + O(E^4) \tag{6.6}$$

This change is the hyperfine component of the Stark shift: it is quadratic to lowest order in E and is parametrized by η_A which is negative, i.e the hyperfine always diminishes (as mixing with the higher states can only reduce the electronic density at the nuclear site). Also, this is valid only for donors far from any interfaces as it would break symmetry leading to linear terms for example.

The Stark shift also involves a change in the electron g-factor g_e. g_e depends on the electron orbit through the spin-orbit interaction, this orbit being different depending on the orientation of the external magnetic field with each valleys along $\mathbf{i} = \{\pm\mathbf{x}, \pm\mathbf{y}, \pm\mathbf{z}\}$ as they have an anisotropic effective mass for $\mathbf{k} \parallel \mathbf{i}$ and $\mathbf{k} \perp \mathbf{i}$ (non-spherical) [WF61, RPB$^+$09, STL14]. Because the ground state ψ_g has an equal combination of all valleys, this anisotropy is normally averaged out. The application of an external electric field leads to two phenomena: first, when it is applied along a particular direction, the weight for each valley are redistributed ("valley repopulation"), modifying the total g-factor which also becomes orientation dependent with the magnetic field as the

symmetry is broken. If the electric field is applied along a valley axis ($\{100\}$), this repopulation is also strongest, whereas if it is along the direction $\{111\}$ it remains unchanged. The second process that changes g_e is due to mixing of conductions bands and the parallel and perpendicular g-factors for each valleys are altered. Overall, the g-factor Stark shift is defined as:

$$\frac{\Delta g_e}{g_e} - 1 = \eta_g(\theta_{\mathrm{BE}}, \theta_{\mathrm{BC}}) E^2 \tag{6.7}$$

where the Stark parameter η_g is dependent on the relative orientation θ_{BE} of the magnetic field with the electric field and the relative orientation θ_{BC} of the magnetic field with the crystal axis. For the same symmetry considerations as for the hyperfine, the g-factor shift is quadratic to lowest order. The dependence in θ_{BE} has been described theoretically and measured in [WF61] with strains, which are mostly equivalent to electric fields, giving the relation: $\eta_g(\theta_{\mathrm{BE}}, \theta_{\mathrm{BC}}) = \eta_g(\theta_{\mathrm{BC}}) \times \left(1 - \frac{3}{2}\sin^2(\theta_{\mathrm{BE}})\right)$.

6.2 Electrically-induced hyperfine control and conditional gates

Starting from the above theoretical considerations, I measure in this Section the Stark shift parameters, η_A and η_g, using ESR measurements, and then demonstrate some practical tests of electrical control on the donor spins.

6.2.1 Stark shift characterization

Model

When taking into account the effect of an applied electric field E, the donor spin Hamiltonian can be rewritten as (always considering the magnetic field along z):

$$H = B_0\left[(\gamma_e + \Delta\gamma_e(E))S_z - \gamma_n I_z\right] + (A + \Delta A(E))\,\mathbf{S}.\mathbf{I} \tag{6.8}$$

where $\Delta\gamma_e(E)$ and $\Delta A(E)$ are the shifts in electron gyromagnetic ratio and hyperfine interactions due to E. This shifts can be written as:

$$\Delta\gamma_e(E) = -\mu_B g_e \eta_{g_e} E^2 \tag{6.9}$$

$$\Delta A(E) = A\eta_A E^2 \tag{6.10}$$

where η_A and η_{g_e} are the Stark parameters defined in Eq. 6.6 and Eq. 6.7, with η_{g_e} also depending on the orientation with respect to the magnetic field and the crystal axis (but not explicitly written for simplicity). They both can be extracted via the change in either electron or nuclear spin transition frequency, which to first order is:

$$\Delta f(E,B_0) = \frac{df}{dA}(B_0) \times \Delta A(E) + \frac{df}{d\gamma_e}(B_0) \times \Delta\gamma_e(E) \tag{6.11}$$

where $\frac{df}{dA}(B_0)$ and $\frac{df}{d\gamma_e}(B_0)$ are the sensitivities, for a particular transition and magnetic field, to the variations $\Delta A(E)$ or $\Delta\gamma_e(E)$. In the high field limit, $\frac{df}{dA}$ is equal to m_I for an electron spin transition and $1/2$ for any nuclear spin transition. $\frac{df}{d\gamma_e}$ is equal to B_0 for an electron spin transition and 0 for any nuclear spin transition. This difference in sensitivity for various transitions can be used to separate the hyperfine and g-factor Stark terms.

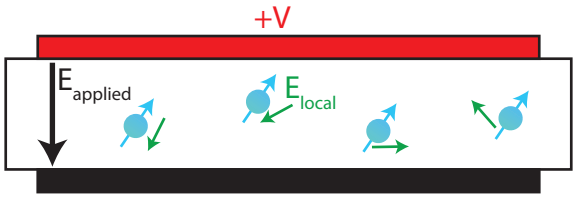


Figure 6.2: **Schematic of electric fields in a sample.** Applied electric fields are in general combined with local electrostatic potentials within the sample. This gives rise to a local Stark shift contribution.

The estimation of the Stark shift depends strongly on the estimation of the electric field. Here, there are some issues to consider, in particular the applied field is rarely the only electric field existing in the sample. In a device for example, local electrostatic gates would result in built-in potentials or the proximity of an interface often has an abundance of charge defects.

In addition, strain in the lattice, also from an interface or simply from the crystal growth, can be equivalent to very large electric fields with strong spatial variation (Figure 6.2). Because the Stark response is quadratic, the effect of an additional electric field can have important consequences due to the simple relation:

$$\|\vec{E}_{\text{local}} + \vec{E}_{\text{applied}}\|^2 = \|\vec{E}_{\text{local}}\|^2 + \|\vec{E}_{\text{applied}}\|^2 + 2\vec{E}_{\text{local}}.\vec{E}_{\text{applied}} \tag{6.12}$$

where $\vec{E}_{\text{local}}$ and $\vec{E}_{\text{applied}}$ are the existing "local" and applied electric fields, respectively. $\|\vec{E}_{\text{local}}\|^2 \equiv E_{\text{local}}^2$, which may simply look as a small constant detuning, results directly in the inhomogeneous broadening T_2^* in an ensemble measurement as the field varies throughout the sample (ΔA in Section 3.1.2). E_{applied}^2 is the expected quadratic Stark shift. However, because of the local term, there is also a linear contribution $E_{\text{local}}E_{\text{applied}}$ which depends both on the applied electric field and the electric environment of each particular spins. This linear term is inhomogeneous due to variations in E_{local}, even if the applied electric field is perfectly homogeneous.

Characterization sequence

The first measurement of the Stark shift was realized by Bradbury *et al.* [BTS$^+$06] using pulsed ESR measurements of ^{121}Sb donors ($I = 5/2$). The frequency shift was measured on the six ESR transitions available at X-Band, however because the linewidth was much broader than the observed shift, it couldn't simply be measured in a field-sweep spectrum. In the time-domain, the inhomogeneous broadening is given by T_2^* however it is always possible to apply a Hahn echo sequence to go beyond this limit to T_2 times. In this case, acquiring a frequency shift is equivalent to a phase shift in time when applying an electric field during the sequence, similar to a Ramsey experiment. Because the echo cancels any static phase before and after the refocusing pulse, the electric field was therefore pulsed and applied only during the first half of the sequence, as shown in Figure 6.3(a).

The existence of the local Stark shift due to local electrostatic fields is quite a problem here: indeed, if each spin acquires a phase at a different rate due to variations in E_{local}, then the

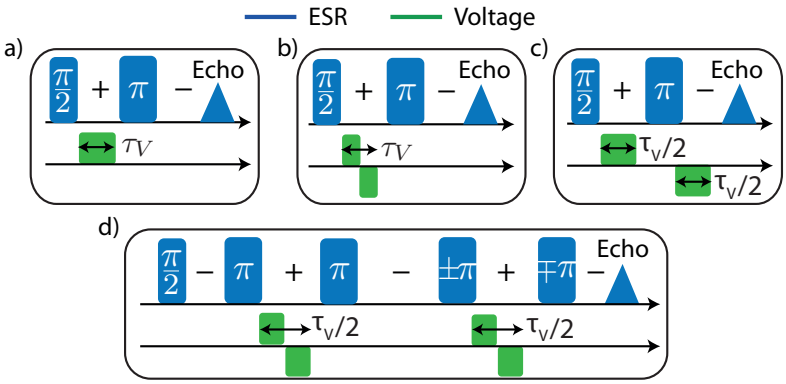


Figure 6.3: **Stark shift sequences.** Various sequences for measuring the Stark shift by phase acquisition. The + and − signs between each pulses show how phases are added due to the MW π refocusing. a) Linear and quadratic contributions. b) Quadratic contribution only: the linear term is canceled by the bipolar voltage. c) Linear contribution only: the quadratic term is canceled by the MW pulse, while the negative voltage compensate the refocusing phase inversion for the linear term. d) Quadratic contribution only with UDD dynamical decoupling (see Section 4.2.1) for longer phase acquisition. Here, the last two π-pulses are phase-cycled to remove stimulated echoes, as given by the $\pm$ and $\mp$ signs (see Chapter A).

ensemble signal rapidly averages out. A simple solution used in [BTS+06] consists of sending voltage pulses to the sample with different polarities. In Figure 6.3(b,c), it can be shown that either the local or the applied contribution can be separated. If both positive and negative voltages are applied during the first half of the echo, the phase acquired is $\phi \propto [(E^2_{\text{applied}} + 2E_{\text{applied}}E_{\text{local}}) + (E^2_{\text{applied}} - 2E_{\text{applied}}E_{\text{local}})] = 2E^2_{\text{applied}}$ and only the quadratic term remains. If the two polarities are applied separately before and after the refocusing pulse, only the linear term remains.

As in most long T_2 measurements, the coherence is not actually limited by dipolar coupling with other spins but simply by magnetic field noise from the experimental setup. This noise typically starts as a phase noise on the measurement, shifting the signal "randomly" between the in-phase and quadrature components but without loss in magnitude. Typically, this is solved by magnitude detection, however in this case the phase component is also the signature of the Stark shift and so must remain stable during the experiment. As such, the acquisition time is limited at the noise onset. This can be significantly improved using a dynamical decoupling sequence, such as UDD (Figure 6.3(d)), and applying the voltage between alternating pairs of

refocusing pulses.

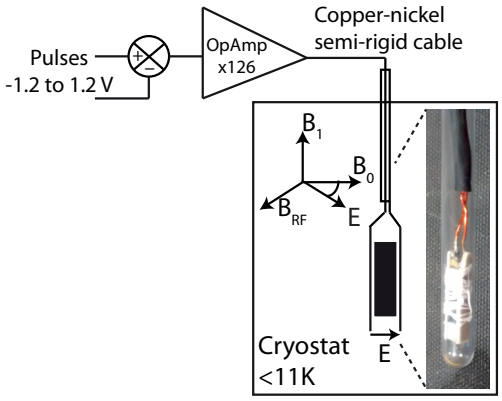


Figure 6.4: **Setup.** Schematic and image of the setup: the electric field is applied using capacitor plates along either the [100] or [110] crystal orientations of the sample. The sample+plates assembly can be rotated along the [110] axis (along B_1) in order to set the angle between magnetic and electric fields. For both ESR and ENDOR experiments, the microwave and radiofrequency excitations are orthogonal to each other and the static magnetic field.

For this experiment, a very simple setup was used: metallic contacts were directly pressed on the side of a bulk ^{28}Si sample as shown in Figure 6.4, connected via a semi-rigid cable (copper-nickel for low thermal conductivity) to a pulse generator outside the cryostat. Bipolar voltage pulses with amplitude up to 1.2 V are produced then amplified by an operational amplifier with gain $G = 126 \pm 1$. The overall circuit has a low-pass RC constant $\tau_{\mathrm{RC}} = 6 \pm 0.6\ \mu$s which is also taken into account in the measurement sequence. Measurements were realized on four group V donors (all but ^{123}Sb) on two isotopically purified ^{28}Si samples: material 1 contains ^{31}P, ^{75}As, and ^{121}Sb donors ranging in concentration between 10^{14} and 10^{15} cm^{-3}, with a thickness of 1.71 mm (float-zone growth). Material 2 has ^{209}Bi in concentration of 2×10^{15} cm^{-3}, with a thickness of 0.79 mm (pedestal growth).

By sweeping the duration τ_V (Figure 6.3(d)) of the voltage pulses, the phase is acquired and Larmor oscillations from the electric field-induced detuning can be obtained as shown in Figure 6.5(b,c) for ^{121}Sb. In the frequency domain (Fourier-tranform), the signal gives the distribution of frequency which is a measure of the electric field distribution within the sample. The electric field deviation, $\sigma_E/\langle E \rangle$, is found to be around 15%. This is of course at the condition that the linear effect is canceled as local effects further broaden the line as seen in Figure 6.5(a).

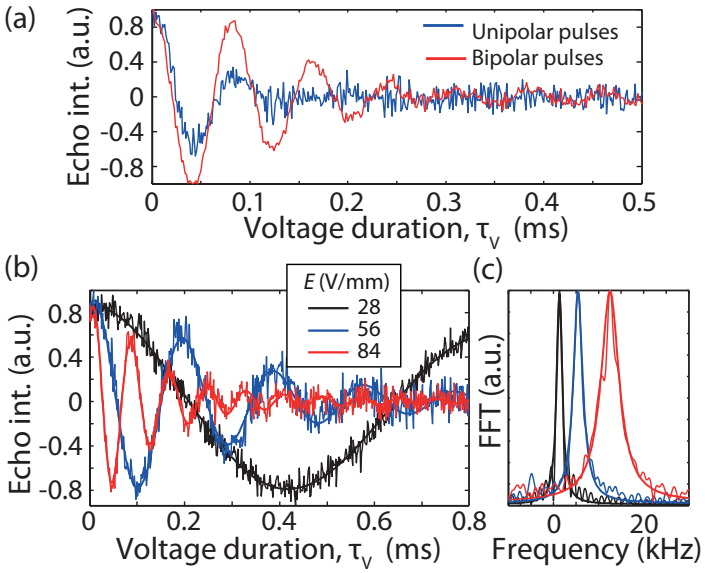


Figure 6.5: **Stark shift characterization.** Electron spin phase evolution measurement using the $m_I = -5/2$ ESR transition with: (a) unipolar versus bipolar pulse (Figure 6.3(a,b)) sequences and (b) bipolar sequence with different electric field intensities. (c) Fourier transform showing the frequency shift distribution in the sample with a Lorentzian fit.

Because the design is just that of a capacitor, the expected distribution should come mainly from surface roughness. It should be mentioned here that in the Bradbury [BTS+06] experiment, the electric field was applied using an interdigital capacitor structure with μm gaps between the fingers. This solution was used to prevent a potential impact ionization, i.e. as soon as the electric field reaches a certain threshold, many donors become ionized. This happens abruptly by an avalanche effect from high energy free electrons and until the applied electric field becomes compensated within the sample by the creation of a depletion layer [KW59, Soh61, vD84]. Estimated impact ionization fields are around 0.1–1 V/μm in similar samples, however it may depend on temperature, voltage duration, separation between the contacts or exact donor/acceptor compensation. The apparent Lorentzian behavior of the measured electric field distribution seemed to suggest such ionization events. However, as no increase in current was observed below 0.3 V/μm with continuous voltage, and considering all experiments were run with pulses up to 0.2 V/μm, there is no reason to believe there was any effect from impact ionization here.

In Figure 6.3(c), the frequency shift was measured for each ESR transition (each m_I state)

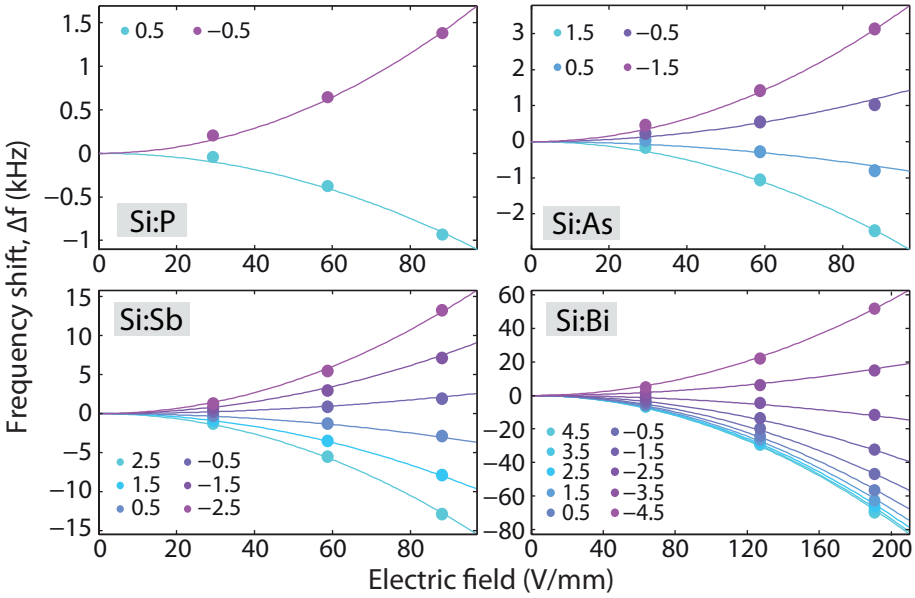


Figure 6.6: **Stark shift characterization.** Quadratic Stark shift for each of the group V donors in silicon, for each ESR transitions according to their high field m_I values.

at X-Band (around 9.7 GHz) for each of the donors. In the high field limit, $\frac{df}{dA} \propto m_I$ and pairs of lines with the same $|m_I|$ Stark shift symmetrically about 0, while $\frac{df}{d\gamma_e} \propto B_0$ and so this effect enhances the frequency shifts for more negative m_I as they are resonant at higher magnetic fields. For ^{209}Bi and to some extent for ^{121}Sb, the Stark shifts in Figure 6.6 look quite antisymmetric but this is actually purely due to electron-nuclear spin mixing as $\frac{df}{dA}$ has not reached its high-field limit at X-band. Finally, the Stark parameters η_A and η_{g_e} are estimated using Eq. 6.11 and fit simultaneously for all transitions and electric fields for a given donor species. The values are reported in Table 6.1 and fits shown in Figure 6.6.

	^{31}P	^{75}As	^{121}Sb	^{209}Bi
$\eta_A(\times 10^{-3}\mu m^2/V^2)$	-2.5 ± 0.5	-1.2 ± 0.1	-3.5 ± 0.05	-0.26 ± 0.05

Table 6.1: **Group V donors in silicon: Stark properties.** η_{g_e} was below the experiment sensitivity ($\approx 10^{-5}\mu m^2/V^2$).

The measured hyperfine shifts are in very good agreement with both previous experimental values in ^{75}As [LSL$^+$14] and ^{121}Sb [BTS$^+$06], and theoretical simulations as shown in Figure 6.7(a). For the electron g-factor, no conclusive data can be reported as the shifts appear to

be much smaller than our setup sensitivity ($\approx 10^{-5}\mu m^2/V^2$), for all possible respective crystalline, magnetic field and electric field orientations as the sample was rotated along the [110] axis. This remains an unanswered question as previous theoretical and experimental values have been contradicting [RPB$^+$09, BTS$^+$06, STL14]. Increasing the sensitivity of the experiment could be achieved with higher static magnetic field (to enhance the g-factor contribution) or stronger and more homogeneous electric fields.

Summary and prospects

This characterization of the Stark shift gives a link between electric field and a phase shift for a donor spin in a coherent superposition. Estimating the decoherence induced by fluctuations in E for donors in a device is therefore possible, though this would depend strongly on the setup and device architecture. In addition, the electric field has specific frequency dependences for various sources of the noise (charge distribution, Johnson-Nyquist, harmonics of 50 Hz, etc...), and the sensitivity of the spin to those depends on the measurement sequence (e.g. π pulse spacings). Such considerations can be found for silicon spin devices in [FCHC06, MDL$^+$14] for example. Finally, just as we have been able to tune the sensitivity to magnetic field in Chapter 5, this is also possible with regards to the electric field. Clock transitions would arise from $\frac{df}{dE} = 0$ which can happen here in two ways: one, at low magnetic fields where in particular $\frac{df}{dA} = 0$, or two at much higher magnetic fields where the g-factor Stark term can compensate the hyperfine interaction shift at the right orientation (as proposed in [STL14]).

For spin control, the relative shifts in g-factor or the hyperfine coupling strength are of less importance than the absolute maximum frequency detuning achievable in a donor as this directly defines the manipulation timescales. The smaller the detuning, the longer the pulses have to be for frequency selectivity and the fidelity of an operation is likely to lower too if the detuning becomes comparable to the spin linewidth. The maximum frequency shift depends on the Stark shift parameters, which transition is being measured and the maximum applicable electric field. For the latter, large electric fields are quite easy to produce in nanoscale structures,

but donors can also ionize. The ground state binding energy ($1sA_1$) was calculated by Effective Mass simulations [PWU$^+$14] to be quite insensitive to electric fields, however it can be crossed by the $2p$-like orbital level whose energy decreases more strongly. In this case, the electron can tunnel off the donor, resulting in ionization. The ionization thresholds for each donor are plotted in Figure 6.7(b).

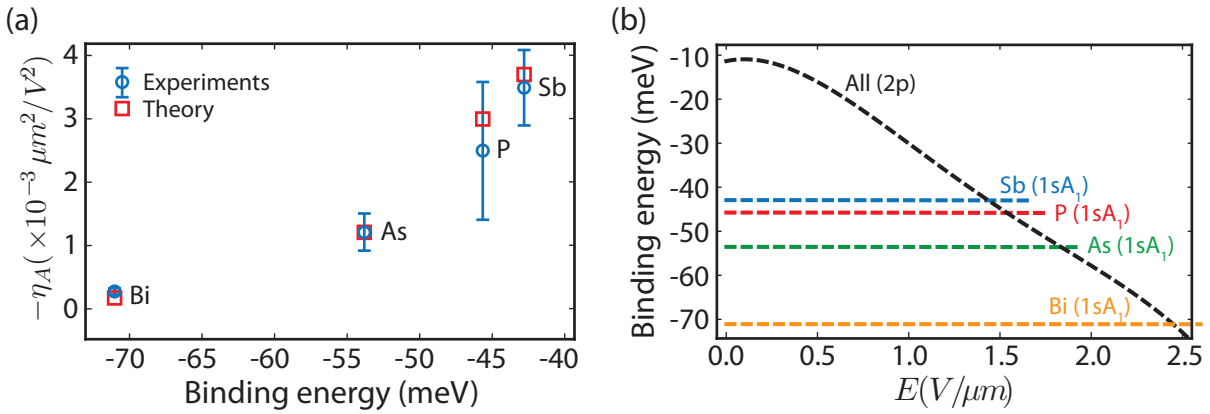


Figure 6.7: **Theory vs. experiment** (a) Theoretical (reproduced from [PWU$^+$14]) and experimental η_A coefficients as a function of the ground binding energy. (b) Donor binding energies of the ground state decrease very weakly as a function of the electric field. On the other hand, the excited 2p energy level, common to all the donors, decreases strongly: where it crosses the ground binding energy, the donor is expected to ionize.

Donor	Ionization field E_c (V/μm)	Maximum hyperfine shift $\Delta A^{\max}$ (MHz)	Maximum ESR frequency shift $\Delta f_{\mathrm{ESR}}^{\max}$ (MHz)	Maximum NMR frequency shift $\Delta f_{\mathrm{NMR}}^{\max}$ (MHz)
^{31}P	1.55	0.8	0.4	0.4
^{75}As	1.84	0.8	1.2	0.4
^{121}Sb	1.45	1.4	3.5	0.7
^{209}Bi	2.45	2.1	9.5	1.1

Table 6.2: **Achievable frequency detuning.** The ionization field is calculated from the crossing in Figure 6.7(b) and used to find the highest achievable frequency shifts. For ESR, this value is calculated at the high field limit where $df/dA \to 9/2$, however at low field, $df/dA \to I+S = 5$ due to mixing and so the shift is slightly larger. The g-factor shift contribution is always neglected.

The maximum achievable frequency shifts are shown in Table 6.2. These values must be compared to principal spin timescales. For an ESR transition in ^{28}Si, the Rabi frequency is typi-

cally $20-50$ MHz, the linewidth is $0.01-0.2$ MHz and the decoherence rate about 10^{-6} MHz. For a NMR transition, the Rabi frequency is typically 0.1 MHz, the linewidth is 0.001 MHz and the decoherence rate about $10^{-8}-10^{-9}$ MHz. In order to prevent any operations from affecting an electrically-detuned qubit, the spin must be shifted by at least a few times the linewidth. For example, the fidelity can be estimated by the simple model:

$$H = \delta\omega(E)S_z + \Omega_R S_x \tag{6.13}$$

where $\delta\omega(E)$ is the detuning and Ω_R the Rabi frequency (e.g. from a global magnetic excitation) whose value is typically slightly larger than the linewidth to fully excite the spins. This gives a state fidelity (e.g. for a pure state $|\uparrow\rangle$):

$$F = |\langle\uparrow| e^{-iHt} |\uparrow\rangle|^2 = 1 - \frac{\Omega_R^2}{\Omega_R^2+\delta\omega^2}\sin^2\left(\frac{1}{2}\sqrt{\Omega_R^2+\delta\omega^2}t\right) \Rightarrow F_{\min} = \frac{\delta\omega^2}{\Omega_R^2+\delta\omega^2} \tag{6.14}$$

or in another way, the ratio $\delta\omega/\Omega_R = \sqrt{F_{\min}/(1-F_{\min})}$. If little inversion is desired when detuned, e.g. $F_{\min} = 0.99$, this ratio must be close to 10. For ^{31}P with ESR, to achieve this ratio the Rabi frequency must be limited to at most 40 kHz, nearly three orders of magnitude slower than what is possible. For ^{209}Bi, it is a little bit better, with maybe up to MHz rotations. In any case, the manipulation times are now much closer to typical NMR, whereas the decoherence rate remains much lower: the electron spin is not a very good qubit anymore. On the other hand, for NMR transitions, the Stark shift is only a few times ($\approx m_I$) smaller than with ESR and the manipulation time remains very similar. The NMR linewidth is sufficiently narrow that it can provide high fidelity local pulses and the decoherence rate is also much lower. Therefore, the nuclear spin appears to be the better choice in an architecture requiring the Stark effect.

While these considerations are quite general, there are other issues that may bring back an ESR transition as a qubit of choice. First of all, the ionization thresholds used here are calculated for bulk silicon and is not valid close to an interface [RPB+09]. Indeed, the interface can act as a potential barrier which confines the electron wavefunction as it is pushed toward

it when the electric field is applied. This enables much higher thresholds and thus larger Stark detunings are possible. A second point is that there may be a class of general operations, such as dynamical decoupling, to apply simultaneously on all qubits, tuned and detuned alike, and therefore could make use of the ESR manipulation speeds as it would not require fine frequency resolution. Finally, the realization of 2-qubit gates may impose further constraints on the choice of qubit, but this depends on the exact scheme used.

6.2.2 Conditional spin control using electric fields

With this characterization of the Stark effect-induced detuning in donors, we can come back to the original question: can the response of spins to a global magnetic excitation be switched on and off by using static electric fields? And how can it be done? Two techniques are proposed here:

- **Phase gate:** the phase acquisition experiment to measure small frequency shifts can also be seen as a phase gate. Any detuning from the resonance frequency results in rotations around the Z axis in the Bloch sphere. By combining both global magnetic and local electric phase gates, universal control is possible.

- **Tuning gate:** if the transition frequency can be shifted by more than the linewidth, then selective magnetic excitation is possible between tuned and detuned spins.

Considering the maximum values estimated in Table 6.2, we can first choose the best donor to perform these demonstrations. In Figure 6.6, a maximum shift of ≈ 70 kHz was obtained with the bismuth sample (material 2) due to a lower thickness and the large $m_I = -9/2$ coefficient, however the ESR linewidth was about 100 kHz. Therefore, frequency resolution is not possible. For a nuclear spin transition the linewidth is much smaller, however df/dA is always close to 1/2 independent of the donor: the high nuclear spin number in bismuth that makes its Stark shift of ESR transitions so large does not do so for the NMR transitions, which are thus only weakly detuned by electric fields. And despite the smaller sample thickness and thus

larger electric field, material 2 had a larger linewidth than material 1 (50 kHz) due to different growth processes. After ^{209}Bi, ^{121}Sb is the next most responsive donor by a large margin. As such, all the following experiments were realized on the $|+1/2,+5/2\rangle \leftrightarrow |+1/2,+3/2\rangle$ nuclear transition of the ^{121}Sb donors of material 1.

Phase gate

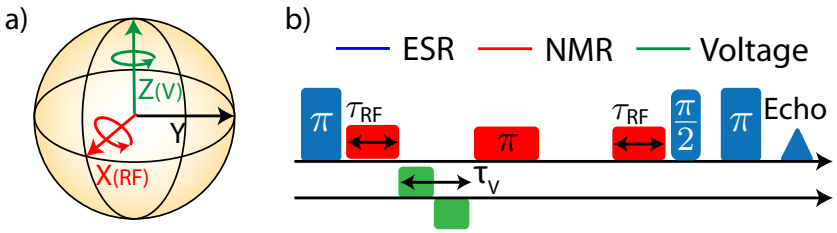


Figure 6.8: **Electrically-controlled nuclear phase gate.** (a) Bloch sphere representation of the nuclear spin rotations: in red, X-rotation from the RF pulse. In green, Z-rotation from the voltage pulse. (b) Pulse sequence with Hahn echo to refocus the inhomogeneous broadening happening during the application of the voltage pulse.

We consider now the Stark shift as a Z-rotation with (Larmor) frequency given by the detuning $\delta\omega(E)$. In addition, a resonant magnetic RF excitation gives a X-rotation with some Rabi frequency Ω_R. These two orthogonal rotation axes provide full control of the Bloch sphere (Figure 6.8(a)). Here, the aim is not to switch-off the spin response but to effectively create a net identity operation, i.e. whatever X-rotation is applied, the spins must come back to their initial states at the end of the evolution. This can be realized with the three-pulse sequence: X-Z-X rotations, such that the propagator is (with I for the nuclear spin operator):

$$U = \mathrm{e}^{-i\theta_X I_X}\mathrm{e}^{-i\theta_Z I_Z}\mathrm{e}^{-i\theta_X I_X} \tag{6.15}$$

$$\Rightarrow U = \mathrm{e}^{-2i\theta_X I_X} \text{ if } \theta_Z = 0 \tag{6.16}$$

$$= \mathrm{e}^{-i\pi I_Z} \text{ if } \theta_Z = \pi \tag{6.17}$$

where $\theta_X = \Omega_R t$ the X-rotation angle from the magnetic field and $\theta_Z = \delta\omega(E)t$ the Z-rotation angle from the electric field. So when $\theta_X = \pi$, the propagator does not depend anymore on the

X-rotation and so the interaction is effectively "switched-off". The additional π Z-rotation is left as is here but could always be compensated. The detuning $\delta\omega$ is 2.5 kHz here, whereas the linewidth is about 500 Hz. The electric field-induced π Z-rotation therefore has a duration which is a significant proportion of the nuclear T_2^*; however, by adding a RF π pulse between the two RF X-rotations and just after the voltage pulse the spins are refocused, similar to Figure 6.3(b). The total sequence is shown in Figure 6.8(b): the RF and voltage pulses are embedded within a Davies ENDOR experiment in order to project the nuclear spin state into the electron spin for measurement. The voltage pulses are still bipolar in order to cancel the inhomogeneous linear Stark effect.

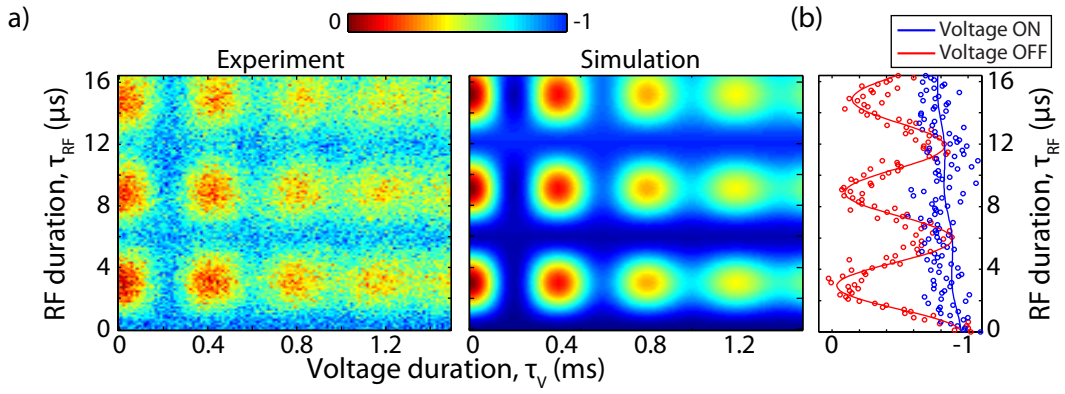


Figure 6.9: **Electrically-controlled nuclear phase gate.** (a) 2D Larmor (voltage)/Rabi (RF) map. The simulation of the evolution follows Eq. 6.18. (b) Projection of the 2D map for $\tau_V = 0$ ("OFF") and 0.2 ms ("ON"), showing how the nuclear spin can be made effectively insensitive to the applied RF field for an appropriate duration of the (150 V) voltage pulse.

The voltage and the RF pulse durations are then both independently swept in a 2D Larmor/Rabi map (Figure 6.9(a)). As expected, the Rabi oscillations alternatively appear and disappear as the Z-rotation angle undergoes multiple of π. The observed dynamics can be modeled using the following equation:

$$S = \frac{1}{2}\left[\left(\cos(\theta_X)^2 - \sin(\theta_X)^2\cos(\theta_Z)D(\theta_Z)\right)D(\theta_X) - 1\right] \tag{6.18}$$

where $D(\theta_X)$ and $D(\theta_Z)$ are two phenomenological distributions for the electric field and the RF magnetic field across the ensemble, leading to finite rotation fidelities. The simulation is

shown in Figure 6.9(a). For $D(\theta_Z)$ a Lorentzian distribution was used, as measured in the characterization experiment. For $D(\theta_X)$, nuclear Rabi oscillations in the absence of any voltage show a Gaussian decay as expected from the nuclear spin linewidth. The normalized echo signal is always between 0 and -1 as is the case for Davies ENDOR experiments. Finally, in Figure 6.9(b), two Rabi oscillations for $\tau_V = 0$ and 0.2 ms, corresponding to 0 and π rotations around Z, are extracted: the effective RF evolution can indeed be influenced and switched off with voltage pulses.

This technique has one interesting advantage: because phase can be acquired during T_2, the Stark shift does not have to be larger than the spin linewidth. However, any real quantum computation would become slightly more complex as three RF pulses are needed for each single rotation.

Tuning gate

I now turn toward the possibility of switching on/off directly the response to RF pulses by detuning the nuclear spins sufficiently off-resonance. For the nuclear spin transition of ^{121}Sb and using Figure 6.9(a), the RF Rabi frequency is $\Omega_R/(2\pi) = 0.5$ kHz and the Stark-induced detuning is $\delta\omega/(2\pi) = 2.5$ kHz, which according to Eq. 6.14 gives a state fidelity of 0.96 (assuming the RF Rabi frequency is equal to the nuclear spin linewidth), quite sufficient for demonstrating this technique.

There is one important issue here: in the previous experiments, the Stark shift was used as a phase gate which allowed for the linear Stark effect to be canceled using bipolar voltage pulses. Here, the spins are simply set off-resonance, perturbing their evolution from an RF pulse. It is therefore not possible to switch the voltage polarity half way to cancel the linear Stark effect. Indeed, the spin model is now for the opposite polarities:

$$H_{\pm} = \pm\delta\omega_{\text{lin}}(E)I_z + \delta\omega_{\text{quad}}(E)I_z + \Omega_R I_x \tag{6.19}$$

where $\delta\omega_{\text{lin}}$ and $\delta\omega_{\text{quad}}$ are the linear and quadratic Stark contribution, respectively. As I_z and

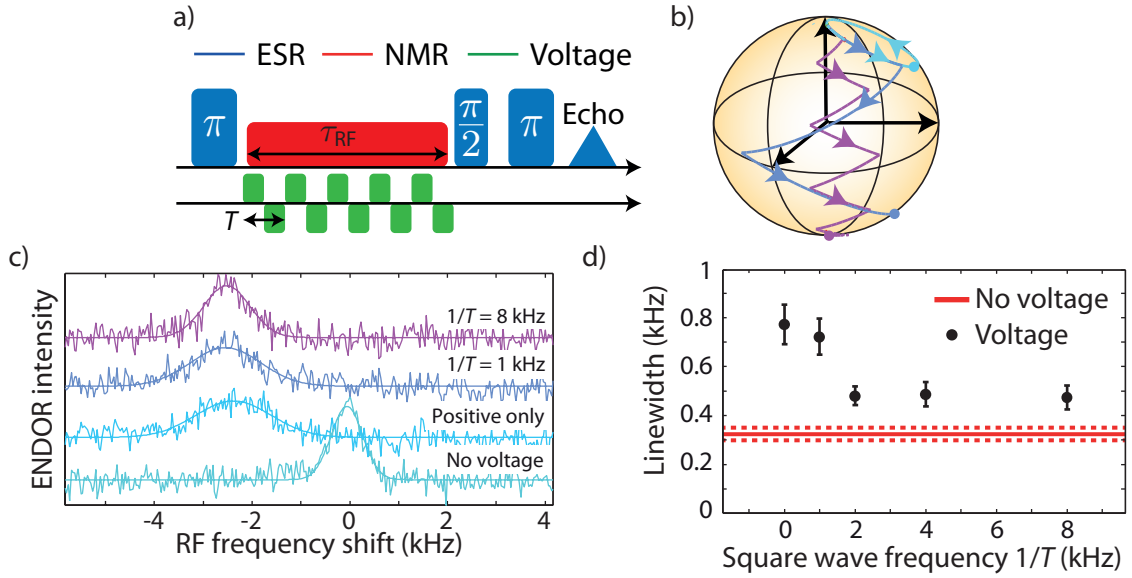


Figure 6.10: **Nuclear tuning gate.** (a) Davies ENDOR sequence with square wave voltage pulses. (b) Bloch sphere representation of the nuclear spin evolution, considering an RF pulse and only the linear Stark shift. The latter adds additional off-resonant evolution, which can be compensated by applying a square-wave voltage pulse with higher and higher frequencies (see different trajectories). (c-d) ENDOR spectra (c) and fitted linewidth (d) measured with and without 150 V pulses, where $\tau_{RF} = 1$ ms corresponds to a π pulse. For a single unipolar voltage pulse, the shifted line is broadened by the linear Stark shift. The shifted ENDOR line can be narrowed by increasing the frequency of a square wave bipolar voltage pulse, up to a point, when it becomes limited by electric field inhomogeneity. In (d), the dashed lines are the error bars for the "no voltage" case.

I_x do not commute, the evolution from H_+ followed by H_- still depends on $\delta\omega_{\text{lin}}$, and the fidelity thus varies from spin to spin. This can be solved by taking inspiration from dynamical decoupling: if the Hamiltonian can be flipped between $+\delta\omega_{\text{lin}}(E)I_z$ and $-\delta\omega_{\text{lin}}(E)I_z$ faster than the total spin evolution, then the effect of $\delta\omega_{\text{lin}}(E)I_z$ can be removed. Similarly, if the voltage polarity can change fast enough, the linear Stark effect can be canceled as shown in Figure 6.10(b). For example, with a square wave pulse with period $T = T_{\text{end}}/N$, where T_{end} is the total evolution time and N is the period number, the propagator becomes:

$$U = \left(e^{-iH_+\frac{T_{\text{end}}}{2N}} e^{-iH_-\frac{T_{\text{end}}}{2N}}\right)^N \tag{6.20}$$

which becomes for large N (Section 4.2.1):

$$U \overset{N\to+\infty}{\to} e^{-i(H_+ + H_-)T_{\text{end}}/2} = e^{-i\left(\delta\omega_{\text{quad}}(E)I_z + \Omega_{\text{R}}I_{\text{x}}\right)T_{\text{end}}} \tag{6.21}$$

In this case, the contribution from the detuning $\delta\omega_{\text{lin}}(E)$ cancels out, and the effect of the linear Stark shift on the linewidth is suppressed.

The measurements start again using a standard Davies ENDOR sequence, but a square wave voltage pulse is applied simultaneously with the RF π pulse as shown in Figure 6.10(a). In the ENDOR spectrum (c), the nuclear spin frequencies with and without voltage are significantly separated as expected. The spin linewidth for positive only or low frequency $(1/T)$ square voltage pulse is broader compared to the no voltage case (see linewidth fits in (d)). For higher square wave frequencies, the linewidth narrows back but saturates around $1/T \approx 2-3$ kHz: this is due to the inhomogeneity of the applied electric field which always results in a distribution of quadratic Stark shifts and hence a broadening.

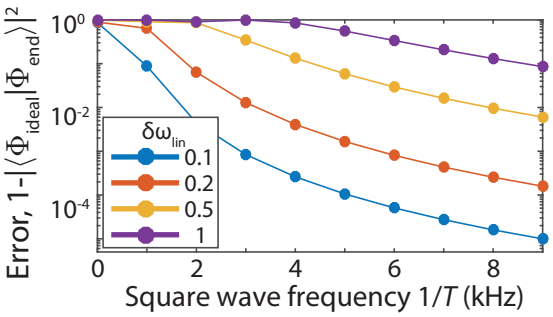


Figure 6.11: **Square wave voltage.** Simplified simulation of the experiment under square wave pulses of varying frequency and different values of the linear Stark shift ($\delta\omega_{\text{lin}}$).

Evidently from the experiment, the linear Stark effect was effectively removed with only a finite number N of pulses. The minimum value for N can be estimated by looking at the second

order of the Suzuki-Trotter expansion:

$$U = e^{-i(H_+ + H_-)T_{\text{end}}/2 + \frac{(-iT_{\text{end}}/2)^2}{2N}[H_+, H_-] + O\left(\frac{T_{\text{end}}^3}{N^2}\right)} \tag{6.22}$$

$$= e^{-i\left(\delta\omega_{\text{quad}}(E) I_z + \Omega_{\text{R}} I_{\text{x}}\right) T_{\text{end}} - i\left(\frac{T_{\text{end}}^2}{4N}\delta\omega_{\text{lin}}\Omega_{\text{R}} I_{\text{y}}\right) + O\left(\frac{T_{\text{end}}^3}{N^2}\right)} \tag{6.23}$$

The requirement for N becomes $N \gg T_{\text{end}}\delta\omega_{\text{lin}}/4$. Following Eq. 6.14, the spin evolution is simulated from some initial eigenstate that is inverted with a RF π pulse. In Figure 6.11(e), the error from a perfect inversion ($|\Phi_{\text{ideal}}\rangle = |\uparrow\rangle, |\Phi_{\text{end}}\rangle = U|\Phi_{\text{ideal}}\rangle$ with $\Omega_R T_{\text{end}} = \pi$) is simulated as a function of the square wave frequency and various amplitude of the linear Stark shift.

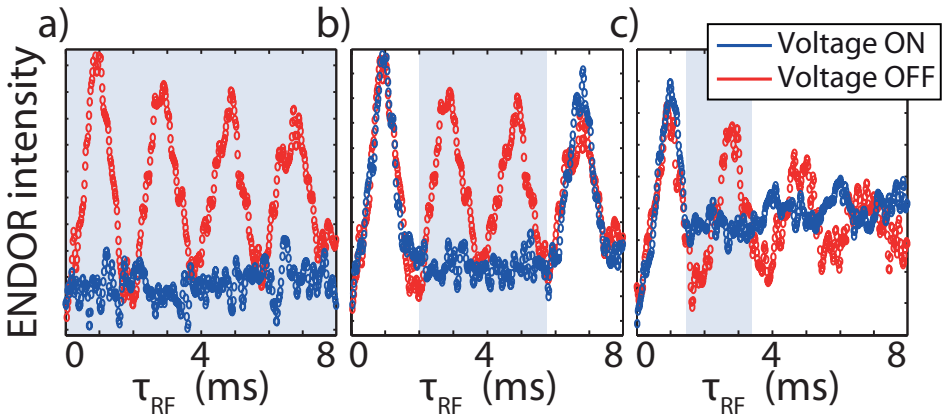


Figure 6.12: **Conditional Rabi oscillations.** Nuclear spin Rabi oscillations, where: (a) the voltage is constantly applied; (b) the voltage is applied only within the light blue window which starts when the nuclear spin is in an eigenstate; (c) the voltage is applied within the light blue window which starts when the nuclear spin is in a coherent superposition state. (For (c), the lower RF pulse fidelity is due to calibration errors compared to (a,b))

With the linear Stark effect removed once again, the tuning mechanism can be tested. In Figure 6.12(a-c), the RF duration τ_{RF} is swept in a Rabi experiment (sequence of Figure 6.10(a)) with the voltage wave applied at different timings:

1. (a): the voltage is applied during the whole RF pulse, right after the electron π pulse (Figure 6.12(a)) which prepared the nuclear state into an eigenstate. The blue curve (with voltage) shows barely any evolution, apart from a negligible decay.

2. (b): this is similar to (a) but the voltage is applied after the population was inverted

(i.e. the nuclear spins are not in a superposition), and stopped after two oscillations. It is interesting to notice that, because the RF Rabi oscillations show limited fidelity control, the second oscillation observed with voltage appears at the same time as the fourth oscillation without voltage but with a greater amplitude. In fact, the amplitude with voltage is more or less equal to that of the second oscillation without, meaning that the spins indeed did not undergo any significant evolution (including decay) while the voltage pulse was applied.

3. (c): the voltage pulse is now turned on after a rotation of angle $3\pi/2$, meaning that the spins are in a coherent superposition. In this case, the spins show significant decay after the voltage is removed. Furthermore, a phase shift can be observed between the blue and red curves.

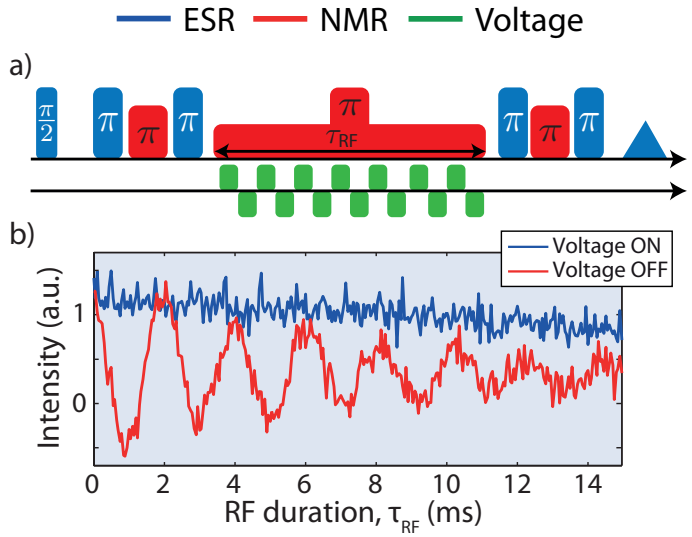


Figure 6.13: **Conditional Rabi oscillations.** (a) Improved sequence for conditional Rabi oscillations with a global refocusing RF pulse to correct for dephasing during the voltage-induced off-resonance. (b) Nuclear Rabi oscillations with and without voltages for an input coherent superposition. The oscillations decay quite fast for negative amplitudes as they correspond to even number of π pulses which prevent refocusing of the nuclear coherence.

So why is the sequence not working in the same way between an eigenstate and a superposition? The problem is that the applied voltage, which detunes the spins, is still very much

a phase gate as before, even though this was not the goal anymore. With the inhomogeneous electric field in the ensemble, this results in the measured signal decay in addition to the phase shift. Furthermore, in an architecture with many qubits and gates, this additional phase is undesirable as it imposes more constraints: either pulse calibration must be very good or each spins acquires different phases which must be tracked separately. To solve this issue, the usual ESR "trick" can be applied, i.e. a refocusing pulse to cancel the acquired phase. Because such refocusing pulses do not need to be applied locally, it is more efficient to apply short pulses with large bandwidth that do not distinguish between on and off resonant spins. The new sequence is shown in Figure 6.13(a), where the transfer from the electron spin to the nuclear spin is furthermore modified to be coherent (adapted from the sequence in Figure 2.7(b)). This will be necessary for characterizing the fidelity using quantum tomography (see below). In (b), the voltage pulse is applied during the entire Rabi oscillation and starting from a nuclear superposition. The signal does not show any sign of phase shift anymore and very little decay is observed (and is in fact partly due to T_1 being $\approx 30-40$ ms).

The application of an electric field allowed us to pause the Rabi oscillations, or, more generally, disable the quantum operation performed via resonant RF excitation of the nuclear spin. The fidelity of this conditional operation can be measured by performing quantum process tomography (QPT) and comparing the measured operation with the ideal one, which is either the π-rotation with voltage or the identity without (i.e. the RF pulse has no effect as the spins are tuned off-resonance by the applied electric field). QPT aims at finding the process that transfers any input states to specific output states [OPG+04]. This is realized by reconstructing from experimental measurements a completely positive map ε of this transformation, represented by the matrix χ, such that for an input density matrix ρ, the output is:

$$\varepsilon(\rho) = \sum_{m,n=0}^{d^2-1} \chi_{mn} A_m \rho A_n^\dagger \tag{6.24}$$

where (A_m) is the Pauli basis $\{\mathbb{1}, \sigma_X, \sigma_Y, \sigma_Z\}$ and $d = 2$ the dimension of the Hilbert space.

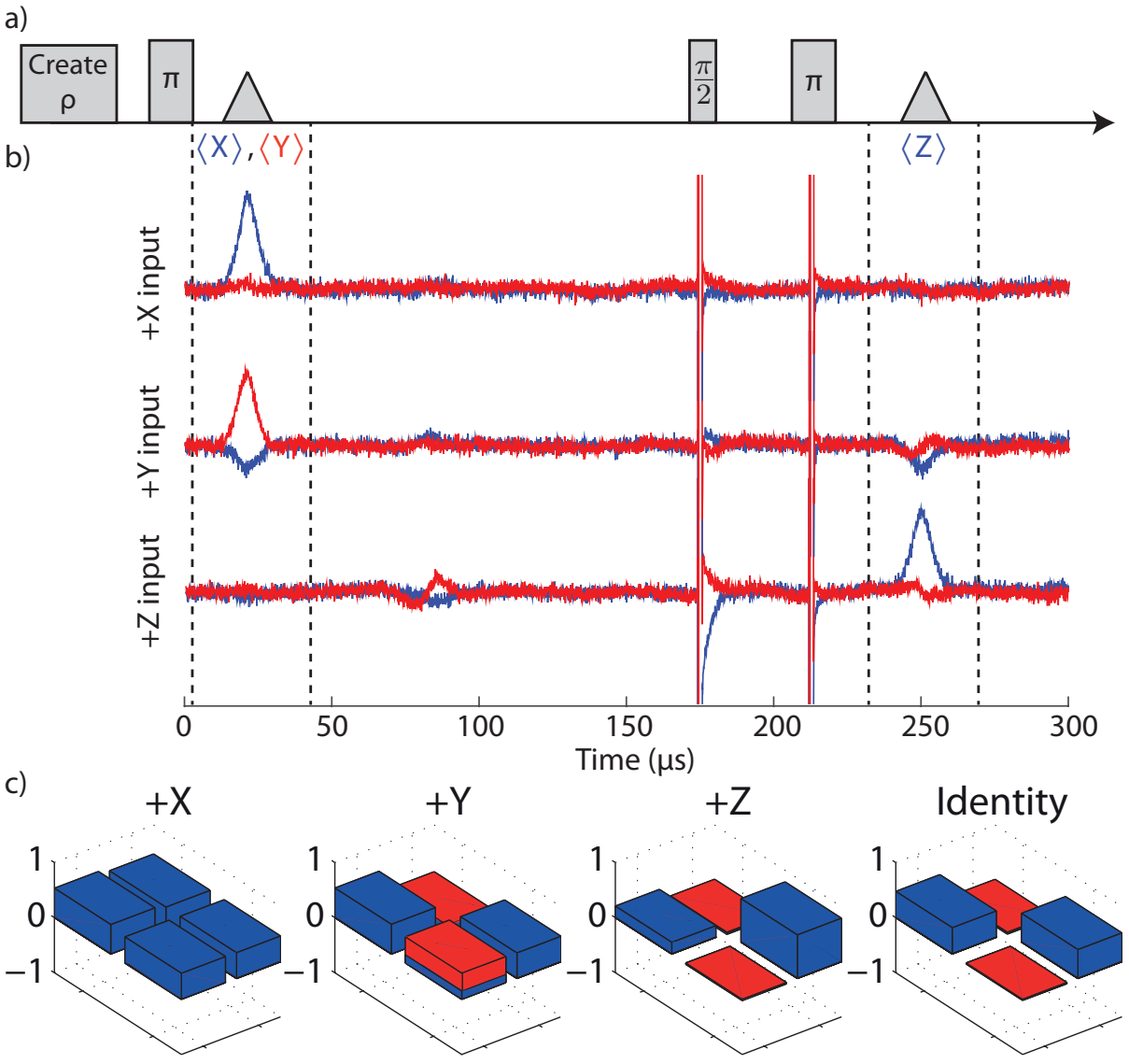


Figure 6.14: **Quantum State Tomography (QST).** (a) Sequence diagram to measure a density matrix ρ in the Pauli basis $[\sigma_x, \sigma_y, \sigma_z]$. (b) Experimental ESR signal with the quadrature X (blue) and Y (red) components. The σ_z measurement is also in blue as it is projected from X using a Hahn echo sequence. (c) Experimental reconstructed density matrices with both RF and voltage pulses. The real part is in blue and the imaginary part in red.

In order to create χ, the 'null' and 'evolved' density matrices $\rho_{\rm i}$ and $\rho_{\rm f} = \varepsilon(\rho_{\rm i})$ are first constructed from the experiments using quantum state tomography, which can be done for mixed (ensemble) states using the method given in the supplementary information of Ref [MTB$^+$08]. The inputs $\{\mathbb{1}, \pm\sigma_{\rm X}, \pm\sigma_{\rm Y}, \pm\sigma_{\rm Z}\}$ are transformed by the combined sequence of RF and voltage pulses and then measured in the $\{\sigma_{\rm X}, \sigma_{\rm Y}, \sigma_{\rm Z}\}$ basis. Each input state is prepared by modifying the first pulse of the sequence in Figure 6.12(e) to rotate from σ_Z to the others. To create an input state equal to the identity $\mathbb{1}$, a non-unitary operation is required to equalize the population, i.e. by using the spin relaxation. After a microwave π pulse and waiting $\ln(2){\rm T}_{1e}$, the electron spin state becomes the identity. For the measurement, $\sigma_{\rm X}, \sigma_{\rm Y}$ are simply taken from the amplitude of the real (A_x) and imaginary (A_y) components of the echo, while $\sigma_{\rm Z}$ requires an additional echo sequence to be measured as $\sigma_{\rm X}$ (A_z) as shown in Figure 6.14(a,b). Assuming the electron spin is pseudo-pure, the reconstructed density matrix is hence given by:

$$\rho = \frac{A_x\sigma_x + A_y\sigma_y + A_z\sigma_z}{2\sqrt{A_x^2 + A_y^2 + A_z^2}} + \frac{\mathbb{1}}{2} \tag{6.25}$$

To minimize the effect of state preparation and measurement errors, the 'null' state is that measured at the end of the sequence (Figure 6.12(e)) in the absence of RF or voltage pulses. The two 'evolved' state density matrices are those obtained in the presence of RF rotation excitation and with/without voltage pulses. In order to obtain pseudo-pure matrices, the norm of the signal (denominator of Eq. 6.25) from the 'null' state is used to normalize all the density matrices. The reconstructed matrices are shown in Figure 6.14(c) for the case where voltage pulses are "ON". In the ideal case with voltage pulses, the nuclear spins should be detuned from the RF pulse and $\rho_{\rm f} = \rho_{\rm i}$. The state fidelity of $\rho_{\rm f}$ onto $\rho_{\rm i}$: $F = {\rm Tr}(\sqrt{\sqrt{\rho_{\rm f}}\rho_{\rm i}\sqrt{\rho_{\rm f}}})^2$ is then computed, giving an average for all input states $\bar{F} = 0.97 \pm 0.1$.

The process matrix χ can be constructed by linear inversion of Eq. 6.24 [CCL01], however the resulting matrix is usually not physical, i.e. not Hermitian positive. The solution is then to find out the closest physical operation via least square fitting of the $\rho_{\rm i}$ and $\rho_{\rm f}$ matrices, as de-

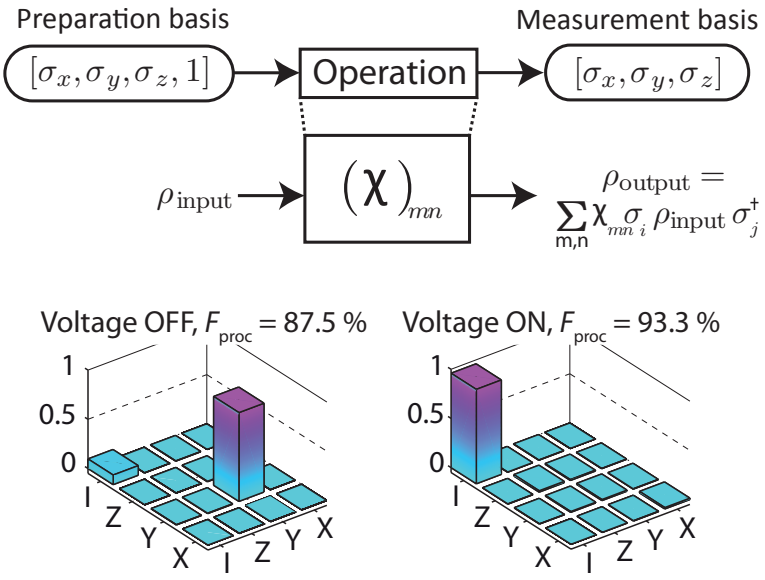


Figure 6.15: **Quantum Process Tomography (QPT).** Top: schematic of a QPT; the aim is to obtain the χ matrix which maps any input states to any output states. Bottom: experimental reconstructed χ matrices of a π RF rotation with and without voltage. The fidelity is calculated by comparison with, respectively, a perfect π RF rotation or the identity, i.e. no evolution occured.

scribed in [OPG+04]. The χ matrices presented in Figure 6.15 are calculated with this method. Finally, the experimental echo intensities are fitted by Gaussian lineshapes, and the standard deviations are then used in a Monte Carlo simulation (Figure 6.16) to obtain the errors on the process fidelities $F_{\text{proc}} = \text{Tr}(\chi_{\text{exp}}\chi_{\text{ideal}})$, where χ_{exp} and χ_{ideal} are the measured and expected process matrices respectively.

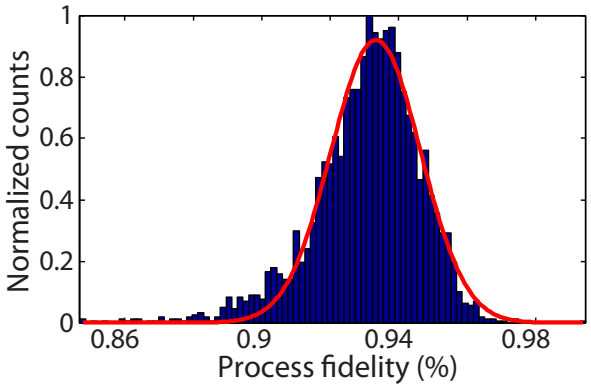


Figure 6.16: **Error analysis for the quantum process tomography.** Histogram of the process fidelities computed by Monte Carlo simulation. Each fidelity is computed from reconstructed χ matrices from echo intensities sampled within their fitted distribution. The total number of counts is 3000.

In the absence of an applied voltage pulse, the conditional nuclear spin gate acts as a π_Y rotation with a process fidelity $F_{\text{proc}} = 87.5 \pm 6.4\%$. The fidelity is strongly reduced here by the inhomogeneous broadening of the nuclear spin ($T_{2\text{n}}^*$) as the slow RF pulse cancels the strong hard π-pulse. Under an applied voltage pulse, the total gate resembles the identity operation with a fidelity $F_{\text{proc}} = 93.3 \pm 2.6\%$. The maximum process fidelity possible is estimated in our setup for the latter case. For this, the hard π pulse in the middle of the operation is assumed to be perfect, while the fidelity of the evolution under the soft RF excitation on either side of this is determined by the finite Rabi frequency (Ω_{R}) and inhomogeneous linewidth ($\delta\omega$). Considering values for $\Omega_{\text{R}}/(2\pi) = 0.54$ kHz and $\delta\omega/(2\pi) = 2.5$ kHz (taken from Rabi oscillations and ENDOR spectra), the expected process fidelity is 95% — this is slightly lowered to 94% by additionally considering the effect of the spin linewidth on $\delta\omega$.

Conclusion

Strategies for further increasing the gate fidelities and overcoming effects such as electric field inhomogeneities includes exploring composite pulses to address systematic errors [Wim94], or using adiabatic sweeps to tune the spins through resonance during the microwave pulse [TG97, WGG$^+$13]. These techniques could be rather insensitive to variations in both electric and magnetic fields (amplitude or frequency), though at the expense of longer gate durations.

In conclusion, I have shown how the nuclear spin of a donor can be effectively controlled through a combination of RF excitation and an external electric field, either through electrically-controlled phase gates or by detuning spins off resonance. The techniques discussed for dealing with electric field inhomogeneities are not limited to ensembles of spins. They could be particularly useful when using electric fields to address a subset of spins in a device, such as tuning out a row of spins in an array. They could also reduce errors from slow temporal variations or crosstalk between nearby qubit gates. Finally, by increasing the electric field closer to the onset of donor ionization, these conditional nuclear spin gates could have timescales of order 10 μs,

which compares favorably to the minutes-long nuclear coherence times.

Until now, I only took advantage of the frequency shift due to the change in the hyperfine interaction, however at high magnetic field the $XX+YY$ component of this interaction is orthogonal to the eigenbasis. Therefore, it can also provide coherent spin control with resonant excitation, very much like a magnetic B_1 field though for different transitions.

6.3 Toward coherent electrical control

The Kane proposal offered to combine a global AC magnetic field with local electric tuning gates. However, one can raise the question of whether full electrical control without any magnetic excitation is also viable. Instead of using static electric fields, pulsed excitations would enable coherent control of the spin, supposing of course that some transitions can be excited by an oscillating hyperfine interaction (similar to [TBB+14]). I therefore consider the suitability of full electrical spin manipulation in donors in silicon.

Considering uniquely the hyperfine Stark shift, the Hamiltonian of the donor system for an oscillating (AC) electric field E at the frequency ω is:

$$H = B_0(\gamma_e S_z - \gamma_n I_z) + (A + \Delta A(E))\,\mathbf{S}.\mathbf{I} \tag{6.26}$$

$$= H_0 + A\eta_A(E_0\cos(\omega t))^2\mathbf{S}.\mathbf{I} \tag{6.27}$$

$$= H_0 + \frac{A\eta_A E_0^2}{2}\mathbf{S}.\mathbf{I} + \frac{A\eta_A E_0^2}{2}\cos(2\omega t)\mathbf{S}.\mathbf{I} \tag{6.28}$$

where H_0 is the natural time-independent Hamiltonian without external electric fields. Because of the quadratic response, the oscillation actually excites at the double frequency. In addition, a static Stark shift is also present. At high magnetic field, the eigenbasis is mainly defined by the Zeeman interaction and the operator $\mathbf{S}.\mathbf{I}$ gives both a parallel ($S_z I_z$) and orthogonal component ($S_x I_x + S_y I_y$). For oscillating electric field, the parallel component is simply averaged out, however the orthogonal one enables transitions between states that are allowed,

i.e. $\langle\psi_1|S_xI_x+S_yI_y|\psi_2\rangle \neq 0$, which occurs when the electron and nuclear spins are simultaneously flipped ($\Delta m = 0$). This is illustrated in Figure 6.17. At low magnetic fields (e.g. below < 0.1 T in ^{209}Bi) where the eigenbasis becomes closer to the hyperfine interaction, there isn't any orthogonal component anymore and no transitions are allowed.

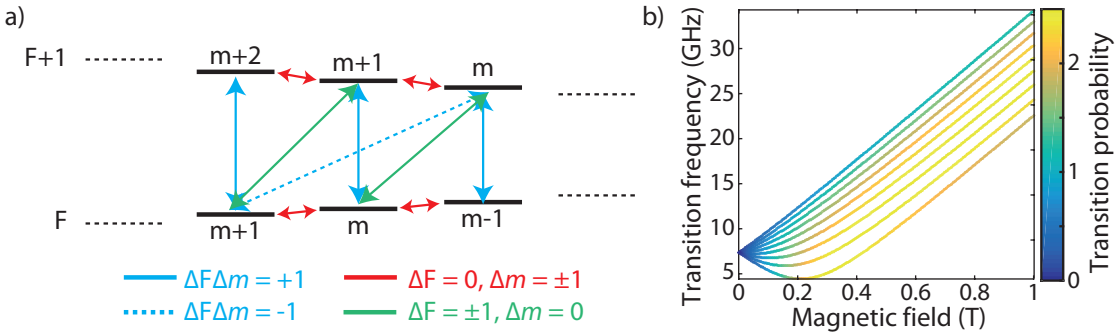


Figure 6.17: **Hyperfine transitions.** a) Schematic of all possible transitions for donors in silicon: allowed and forbidden ESR (blue), NMR (red) and hyperfine (green) according to their high-field nomination. b) Eigen-frequencies in ^{209}Bi as a function of magnetic field for hyperfine-allowed transitions. The colormap gives the transition probability $\langle\psi_1|S_xI_x+S_yI_y|\psi_2\rangle$ between the two states of each transition.

According to Eq. 3.4 (and using the same notations), the transition probability between two states $|-,m\rangle$ and $|+,m\rangle$ is:

$$\langle -,m|\mathbf{S}.\mathbf{I}|+,m\rangle = \frac{\Omega_m}{2}\left(\cos^2\left(\frac{\theta_m}{2}\right)-\sin^2\left(\frac{\theta_m}{2}\right)\right)-m\cos\left(\frac{\theta_m}{2}\right)\sin\left(\frac{\theta_m}{2}\right) \tag{6.29}$$

$$= \frac{\Omega_m}{2R_m}(\Delta_m - m) \tag{6.30}$$

At low field, $\Delta_m \to m$ and therefore the probability is 0, while at high field $\theta_m \to 0$ and the probability is maximum, as expected. The maximum value is $\frac{1}{2}\left(I+\frac{1}{2}\right)$ which happens for $m = 0$. From this, the maximum Rabi frequency under an applied electric excitation is:

$$\Omega_R^{\max} = \frac{I+\frac{1}{2}}{4}A\eta_A E_0^2 \tag{6.31}$$

From the ionization fields estimated in Table 6.2, this gives the following table of values for each of the group V donors:

	^{31}P	^{75}As	^{121}Sb	^{209}Bi
$\Omega_R^{\max}/(2\pi)$ (MHz)	0.2	0.4	1.0	2.7

Table 6.3: **Group V donors in silicon: Maximum Rabi frequencies using AC electric fields.** These frequencies are calculated using the bulk ionization electric fields for each donor, as given in Table 6.2. Higher electric fields might be possible in devices due to interface effects.

^{121}Sb and ^{209}Bi offer a non-negligible Rabi frequency if strong electric fields at high frequency can be applied. In an ensemble this is quite difficult but in a nanoscale device this would be achievable. One comment can be made here: while few MHz manipulation time is quite small compared to what is achievable with an electron spin, the transitions manipulated here are electron-nuclear flip-flops. The typical Rabi frequency for a nuclear spin is only about 0.1–1 MHz and so this now compares well with the electric manipulation.

The linear Stark effect due to local electric fields was one of the main obstacles to obtaining good fidelity in the Stark tuning experiment. Yet, it also presents a way to modify the response of the spins to electric field. Indeed, if a static field E_{DC} is applied in addition to the excitation, the quadratic Stark response gives (Eq. 6.12):

$$(E_{\mathrm{DC}} + E_0\cos(\omega \mathrm{t}))^2 = \left(E_{\mathrm{DC}}^2 + \frac{E_0^2}{2}\right) + \frac{E_0^2}{2}\cos(2\omega \mathrm{t}) + 2\mathrm{E_{DC}E_0}\cos(\omega \mathrm{t}) \tag{6.32}$$

In addition to a constant shift and an oscillation at the double frequency, there is now a linear component in both E_{DC} and E_0 and oscillating at the fundamental frequency. Though very simple, this has the important consequence that a spin response to a microwave electric excitation can be controlled on-demand by the application of a static electric field field. If $E_{\mathrm{DC}} = 0$ and the transition frequency is ω, nothing happens, but if E_{DC} is at a maximum value, coherent control is enabled. Finally, the static electric field acts as an amplifier for the oscillating field, which then requires less power. This behaviour also has consequences with regard to the decoherence from electric fields. If the spins are biased in any way, they immediately become more sensitive to electric noise; it might therefore be necessary to compensate in a device the local electric field of each spin.

It should therefore be possible to achieve coherent electrical control of donor spins, in particular for either ^{121}Sb or ^{209}Bi. This would be quite beneficial to spin device architecture, likely reducing some of the complexity required for controlling single spins.

6.4 Conclusion

Electrical control of donors in silicon is a key requirement for a scalable architecture. Here, I first characterized the spin sensitivity to electric fields for the major dopants in silicon, and concluded that this type of control seems more suited to the nuclear spin. I then demonstrated with relatively high fidelity the electric-induced switching of this spin to magnetic field excitations, paving the way for local control in devices. Finally, I proposed the possibility of full coherent control of the donor using electric fields.

CHAPTER 7

Conclusion

Throughout this study, donor spins in silicon have been investigated, with a focus on going beyond the isolated spin-1/2 picture. Be it due to interactions between spins, intrinsic or extrinsic to the donor, or through the use of adequate pulse sequences, the measured qubit evolution can becomes much more complex. Important information regarding the spin system and its environment are therefore available, improving our understanding of their dynamics and our capability to control them. Without the need to resort to new materials, most of the enhancements obtained or proposed here were mainly realized by making the most of the donor and its surrounding, or more generally, the "known" system.

In Chapter 4, dynamical decoupling was first used in ^{31}P to enhance the electron spin coherence times in ^{nat}Si, eliminating some of the spectral diffusion noise from local ^{29}Si. In addition, the modified electron spin evolution under MW π pulses becomes more sensitive to higher order processes in the bath, in particular possible many-body correlations in the ^{29}Si nuclear spin bath. In a second part, the presence of the ^{29}Si was also acknowledged as potential additional registers for quantum error correction. A scheme was presented with some considerations re-

garding the electron spin-induced dephasing when initializing ancillae. The coherence time of the nuclear spins in ^{nat}Si was furthermore measured to be in the second timescale, which is quite reasonable for a quantum memory. The equivalent pair model was also introduced as the possible decoherence mechanism, which could be damped by the application of large strain or electric field for example as the electron wavefunction would become asymmetric.

In Chapter 5, the spin Hamiltonian of ^{209}Bi was operated in special regimes set by the external magnetic field. The properties of some of the spin transitions become different from their high field values, enabling for example manipulation of forbidden transitions and control over the spin sensitivity to free parameters such as the magnetic field. In the extreme case of "clock transitions", noise from *ZZ*-type fluctuations was considerably turned down in ^{nat}Si and eliminated in ^{28}Si, allowing coherence times of few seconds and manipulation speeds typical of pure electron spins. In ^{nat}Si, the choice of spin Hamiltonian regime has direct consequences on the evolution of the bath, which I modeled using the pseudo-spin picture and confirmed over many different types of transitions, from pure electron or nuclear spin, to various mixed regimes.

Finally, while Chapter 4 and 5 regarded mostly the magnetic part of the system, Chapter 6 considered more in depth the hyperfine interaction as a free parameter controllable with electric fields via the Stark shift. First, I characterized the sensitivity of the donor to this effect, for ^{31}P, ^{121}Sb, ^{75}As and ^{209}Bi. It was concluded that, at least in bulk, electric control was more adequate on the nuclear spin due to its stronger ratio of Stark shift over frequency linewidth compared to the electron spin. I further demonstrated on-demand electric switching of the spin response to magnetic pulses. Efforts were made to take into account pulse errors, eventually obtaining above 90% fidelities. Such a demonstration is a key requirement of the Kane proposal for large scalability of quantum computers in donors in silicon, though of course it was only shown in an ensemble here (a similar work in single-spin devices realized more recently can be found in [LMM$^+$15]).

Following the many previous studies of donor spins in silicon, the interest of this system

as a candidate for quantum information has been further reinforced. Between the results here and those accomplished recently in ionized donor [SSS$^+$13], the coherence times in silicon are some of the best and probably quite sufficient for many quantum protocols. Alternative donors to ^{31}P like ^{209}Bi which had been barely studied before seem now quite appealing as a replacement, especially since ^{31}P cannot have ESR-like clock transitions and is quite insensitive to electric field manipulation via Stark shift. Considering the recent impressive works in single spin devices [PTD$^+$12, PTD$^+$13] with ^{31}P, it would be quite interesting to see the advantage of such donor there. Finally, the large zero-field splitting around 7 GHz in ^{209}Bi makes this donor attractive as memory in hybrid quantum circuits with superconducting resonators, with some initial studies reported in [YBS$^+$15].

APPENDIX A

Phase cycling and unwanted echoes

Phase cycling is a common technique of magnetic resonance to eliminate undesired contributions to the spin echo signal. The basic concept can be understood in the following example: a Hahn echo sequence creates a superposition with a $\pi/2$ pulses which is then refocused with a π pulse. Starting from a density matrix S_z and pulses along X, the evolved state is S_y. If we reverse the sign of the first pulse to $-\pi/2$, the spins end up in the other side of the Bloch sphere to $-S_y$. The difference in the two spin signals therefore adds up, however any contribution that are not due to the resonant spins does not respond to the pulses and hence cancels out (Figure A.1(a)). This is a simple way to eliminate a baseline in experiments without losing any signal averaging.

We now turn toward more complicated sequences such as dynamical decoupling. With CPMG or UDD for example (Section 4.2.1), the first pulse creates the coherence and then only refocusing π pulses are applied. This description is however very ideal: in practice, pulse fidelity is never perfect in particular for spin ensembles that have large inhomogeneous broadening, such as for $^{\text{nat}}$Si. A π pulse is more aptly described by a $\pi + \Delta\theta$ pulse, where $\Delta\theta$ is a shift from the ideal rotation with some distribution across the ensemble. A coherence $\rho_0 = S_y$

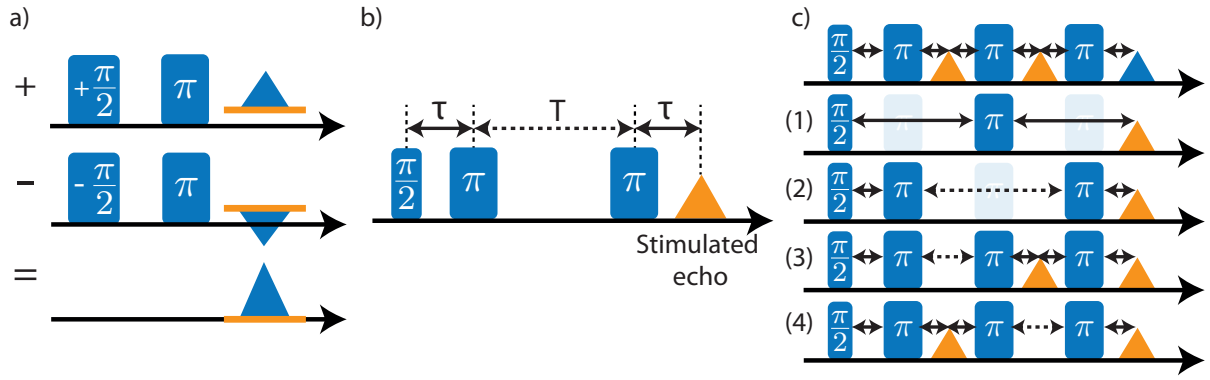


Figure A.1: **Phase cycling.** a) Phase cycling to eliminate non-spin related signals, such as a baseline (orange). b) 2-(π-)pulse stimulated echo. c) CPMG-3 with decomposition to all intermediate and undesired echos (orange) that can appear simultaneously with the final desired echo (blue). Transparent π pulses are unused (from imperfect refocusing). Dashed arrow represent 2-pulse processes for stimulated echos.

that normally becomes $-S_y$ with a π pulse around X is now $\rho_{\text{end}} = -\cos(\Delta\theta)\mathrm{S_y} + \sin(\Delta\theta)\mathrm{S_z}$ according to Eq. 2.12. The signal is the projection on the Y axis $2\mathrm{Tr}\left(S_y, \rho_{\text{end}}\right) = -\cos(\Delta\theta)$, however this can also be written in the following form:

$$\mathrm{Tr}\left(S_y, \rho_{\text{end}}\right) = \cos^2\left(\frac{\Delta\theta}{2}\right)\mathrm{Tr}\left(\mathrm{S_y}, \mathrm{e}^{-\mathrm{i}\pi\mathrm{S_x}}\rho_0\mathrm{e}^{\mathrm{i}\pi\mathrm{S_x}}\right) + \sin^2\left(\frac{\Delta\theta}{2}\right)\mathrm{Tr}\left(\mathrm{S_y}, \rho_0\right) \tag{A.1}$$

Here, the signal is decomposed into two parts: one sub-ensemble of the spins with weight $\cos^2\left(\frac{\Delta\theta}{2}\right)$ received a perfect π pulse ($e^{i\pi S_x}$), and the rest did not respond at all. Intuitively, an imperfect π pulse is therefore equivalent to a perfect pulse but applied only on a fraction of the ensemble. This picture explained for example why a smaller refocusing angle can cancel the effect of instantaneous diffusion as it is equivalent to a lower effective spin concentration. In the case of DD, this is quite an issue: if the pulses are imperfect, some small component of the signal may be from spins that have not undergone all the refocusing pulses, yet are still refocused at the same point in time as those spins which have undergone the full, desired, evolution.

In addition to this problem of "unresponsive" pulses, more than one pulse with angles lower than π can combine together to form a refocusing pulse, even if they are separated from one another. These are called "stimulated echoes" and in general can be limited to pairs of pulses.

If the first pulse is placed τ after the last refocused echo (or just after the coherence was created), the stimulated echo will appear τ after the second pulse, independent of the inter-pulse distance T (Figure A.1(b)). Considering for example an initial state $\rho_0 = S_y$, two imperfect π pulses around X and a dephasing $\delta\omega \times t$ during free precession due to spin inhomogeneity, the projection of the final density matrix is:

$$2\mathrm{Tr}\left(S_x, \rho_{\mathrm{end}}\right) = -\sin(2\delta\omega\tau)\left[\cos^2(\delta\omega \mathrm{T}/2)\cos^2(\Delta\theta) - \sin^2(\delta\omega \mathrm{T}/2)\right] \tag{A.2}$$

$$+\cos(2\delta\omega\tau)\sin(\delta\omega \mathrm{T})\cos(\Delta\theta) \tag{A.3}$$

$$2\mathrm{Tr}\left(S_y, \rho_{\mathrm{end}}\right) = +\cos(2\delta\omega\tau)\left[\cos^2(\delta\omega \mathrm{T}/2)\cos^2(\Delta\theta) - \sin^2(\delta\omega \mathrm{T}/2)\right] \tag{A.4}$$

$$+\sin(2\delta\omega\tau)\sin(\delta\omega \mathrm{T})\cos(\Delta\theta) \tag{A.5}$$

$$-\cos^2(\delta\omega \mathrm{T}/2)\sin^2(\Delta\theta) \tag{A.6}$$

If pulses are perfect, i.e. $\Delta\theta = 0$, and after averaging over $\delta\omega$ for an ensemble, the signal is along S_y if $T = 2\tau$, otherwise it is zero; this is the normal echo case. If pulses are not perfect, i.e. $\Delta\theta \neq 0$, there is an additional component along S_y at any time T, independent of τ, but with amplitude $2\mathrm{Tr}\left(S_y, \rho_{\mathrm{end}}\right) = -\frac{1}{2}\sin^2(\Delta\theta)$; this is the stimulated echo. One interesting point here is that the sign of this projection is inversed if the phases of the two pulses are opposite (e.g. $+X, -X$). This is not the case however for the normal echo, hence by playing with the phases we can obtain independent control on the various echo contributions.

In Figure A.1(c), the 3-pulse CPMG sequence is given with all possible echoes that can appear at the same time as the desired one. Considering the previous explanations, we can now apply the phase cycling sequence presented in Table A.1 to remove most of the echoes. By summing the signal after each phase cycle, echo (2-4) are all canceled. Echo (1) cannot be canceled here because it is not from any stimulated echo. Canceling this term would involve also changing the rotation axis of the pulses to $\pm X, \pm Y$. In general, many echoes (including echo (1) here) can simply be neglected as each "unresponsive" π pulse or stimulated echo gives a smaller signal contribution. In addition, the less pulses are involved the less effective the

Phases	$+++$	$-++$	$+-+$	$++-$
Real echo	$+$	$+$	$+$	$+$
Echo (1)	$+$	$+$	$+$	$+$
Echo (2)	$+$	$-$	$+$	$-$
Echo (3)	$+$	$-$	$-$	$+$
Echo (4)	$+$	$+$	$-$	$-$

Table A.1: Phases for the three π pulses in Figure A.1(c)
and corresponding signal sign for the final echo of each sub-sequence.

dynamical decoupling is and these terms simply disappear for longer τ. Finally, in a sequence like UDD, the non-equal spacing between pulses pushes apart most of the echoes from the intended one.

APPENDIX B

Interactions and df/dB_0

In ESR, the entire Hilbert space is never measured entirely but always as a restricted subspace spanned by the two states whose transition is allowed and probed. After diagonalization of the donor Hamiltonian (Section 3.1.1), this subspace is similar to a pseudo-spin:

$$H_D = \begin{pmatrix} E_+ & 0 \\ 0 & E_- \end{pmatrix} \tag{B.1}$$

where E_+ and E_- are the energies of the upper $(+)$ and lower $(-)$ states of the transition. This matrix can be rewritten as $H = \frac{E_+ + E_-}{2}\mathbb{1} + (E_+ - E_-)M_z \approx \omega M_z$ with $\omega = E_+ - E_-$ and M the operator for this pseudo-spin. The identity component is neglected as it only gives a global phase to the evolution.

What happens to interactions here? In the same way the diagonalization is a change in basis, any interaction must be rotated too. To start with, the easiest coupling to consider is a pure Z term such as given by magnetic fluctuations: $H_I = B_I(t)(\gamma_e S_z + \gamma_n I_z)$ where S and I are the electron and nuclear spin operators of the donor, and $B_I(t)$ is a small magnetic fluctuation from

the static B_0 field. After rotation, the Z components are also partially transfered to off-diagonal elements, however ω is usually much larger and they can be disregarded. This approximation also means that the interactions are weak enough that there is no change in the eigenbasis. The interaction becomes:

$$H_I' = \begin{pmatrix} \langle +|H_I|+\rangle & 0 \\ 0 & \langle -|H_I|-\rangle \end{pmatrix} = \begin{pmatrix} B_I(t)P_+ & 0 \\ 0 & B_I(t)P_- \end{pmatrix} \approx \gamma_e B_I(t)(P_+ - P_-)M_z \quad \text{(B.2)}$$

where $P_\pm = \langle \pm| S_z + \frac{\gamma_n}{\gamma_e} I_z |\pm\rangle$ is the expected change in energy for each state, normalized to γ_e. It can be shown that for any two states $|\pm\rangle$, the difference $\gamma_e(P_+ - P_-)$ is equal to the gradient $\frac{d\omega}{dB_0}$, or $\frac{df}{dB_0}$ in frequency unit. The interaction Hamiltonian above is then simply $H_I' = B_I(t)\frac{df}{dB_0}M_z$.

We now turn toward dipole-dipole couplings between two donors: $H_I = C_{12}(S_{1z} + \frac{\gamma_n}{\gamma_e} I_{1z})(S_{2z} + \frac{\gamma_n}{\gamma_e} I_{2z})$ with $S_{1,2}$ and $I_{1,2}$ the electron and nuclear spin operators for each donors and C_{12} the constant for the coupling strength. H_I is then rotated in the diagonalized basis for each donor and reduced to four states $|1+,2+\rangle, |1+,2-\rangle, |1-,2+\rangle, |1-,2-\rangle$ such that:

$$H_I' = \begin{pmatrix} \langle 1+,2+|H_I|1+,2+\rangle & 0 & 0 & 0 \\ 0 & \langle 2+,2-|H_I|1+,2-\rangle & 0 & 0 \\ 0 & 0 & \langle 1-,2+|H_I|1-,2+\rangle & 0 \\ 0 & 0 & 0 & \langle 1-,2-|H_I|1-,2-\rangle \end{pmatrix} \quad \text{(B.3)}$$

Using $P_{1,2\Sigma} = \frac{P_{1,2+} + P_{1,2-}}{2}$ and $P_{1,2\Delta} = \frac{P_{1,2+} - P_{1,2-}}{2}$ and defining $M_{1,2}$ as operator for each donor pseudo-spin, we get:

$$H_I' = C_{12}(P_{1\Sigma}P_{2\Sigma}\mathbb{1} + 4P_{1\Delta}P_{2\Delta}M_{1z}M_{2z} + 2P_{1\Delta}P_{2\Sigma}M_{1z} + 2P_{1\Sigma}P_{2\Delta}M_{2z}) \quad \text{(B.4)}$$

Neglecting all but the ZZ component:

$$H_I' \equiv 4C_{12}P_{1\Delta}P_{2\Delta}M_{1z}M_{2z} = C_{12}(P_{1+}-P_{1-})(P_{2+}-P_{2-})M_{1z}M_{2z} = C_{12}\frac{df_1}{\gamma_e dB_0}\frac{df_2}{\gamma_e dB_0}M_{1z}M_{2z} \tag{B.5}$$

Again, the interaction has a similar form before rotation to the eigenbasis, with a sensitivity renormalized to $\frac{df_{1,2}}{dB_0}$ for each transition of each donor.

APPENDIX C

^{29}Si spin decoherence models

In Section 4.3.2, the coherence time of ^{29}Si spins with various hyperfine couplings to the donor was measured. Here, we summarize typical models that may be responsible for the observed decay timescales. We start from the pseudo-spin picture of Section 4.1.2, with the difference that the central spin is a nuclear spin (0) now. In addition, the effect of the electron spin-induced detuning $\Delta A = A_{e1} - A_{e2}$ cannot completely be excluded. Considering a particular but fixed electron spin state, the Hamiltonian is therefore $\delta\omega_{\pm} I_z + \Omega_{\pm} I_x$ with:

$$\delta\omega_{\pm} = +\frac{\Delta A}{2} \pm (C_{01} - C_{02}) = +\frac{\Delta A}{2} \pm \Delta C_0 \tag{C.1}$$

$$\Omega_{\pm} = C_{12} + \frac{A_{e1}A_{e2}}{2\omega_e} \tag{C.2}$$

where $C_{01,02}$ are the dipolar interactions between the central spin 0 and the bath spin pair, and ΔC_0 is the difference.

The α parameter in Eq. 4.17 required to estimate T_2 does not simplify easily with such interactions. To understand the coherence time of the ^{29}Si, various possible regimes and ap-

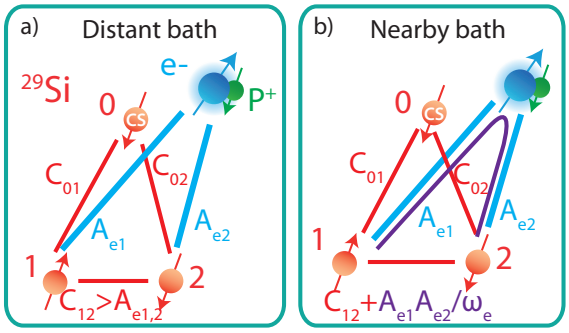


Figure C.1: **Test models for ^{29}Si spin decoherence.** a) Decoherence from ^{29}Si spins far enough ($>$ 8 nm) from the donor to flip-flop easily. b) Decoherence from ^{29}Si spins closer to the donor. Hyperfine interactions are more important.

proximations must be considered as pictured in Figure C.1:

- *(a) Far bath:* Far from the donor ($\approx 8-10$ nm), the bath is free to flip-flop without much hyperfine interaction ($A_{e1,e2} < C_{12}$). In addition, because the measured ^{29}Si is always close to the donor, the hyperfine couplings $A_{e1,e2} \approx 100$ Hz are larger than the dipolar interactions $C_{01,02} \approx 0.01$ Hz at such distance. In this regime with $C_{12} > A_{e1,e2} > C_{01,02}$, α simplifies to:

$$\alpha \approx \frac{2\Delta C_0}{C_{12}}\left[\sin^2\left(\frac{C_{12}}{2}t\right) - \sin^2\left(\frac{\Delta C_0 \Delta A}{4C_{12}}t\right)\right] \tag{C.3}$$

  The oscillation amplitude is below 10^{-4} and the oscillation frequency is either slightly too fast (ω_Σ) or too slow (ω_Δ) compared to the measured T_{2n}, which results after averaging of C_{12} in no significant time-dependence. Also, even if the pair was far enough from the donor to have $A_{e1,e2} \to 0$, C_{12} cannot be arbitrarily small to increase the amplitude of α: indeed the ^{29}Si themselves detune each other in the bath (this gives a linewidth of 127 Hz in NMR [HIV08]), similar to an increase of the ΔA term above.

- *(b) Intermediate/Close bath:* As the nuclear spin pair approaches the donor, the hyperfine interaction starts to dominate all the dipolar interactions and the spins are strongly detuned. The hyperfine mediated term also becomes non-negligible and slightly intensifies

the pair flip-flop. This gives:

$$\alpha \approx \frac{8\Delta C_0\left(C_{12}+\frac{A_{e1}A_{e2}}{2\omega_e}\right)}{\Delta A^2}\left[\sin^2\left(\frac{\Delta A}{4}t\right)-\sin^2\left(\frac{\Delta C_0}{2}t\right)\right] \tag{C.4}$$

For the same reason, this is even less probable as the previous model. The detuning ΔA is too large to allow any pair from affecting the central spin evolution.

The far bath model could be possible due to the large number ($\approx 10^8$) of pairs existing at long distances from the donor (frequency crowding below 0.1-1 MHz in Figure 4.1(b)). However, there is one last possible mechanism we need to consider: in the silicon lattice, there are sites where ^{29}Si spins have equal hyperfine coupling values with the donor due to tetrahedral symmetry. Pairs of ^{29}Si spins sitting on such sites are called "equivalent pairs" (EPs), they have no detuning and can thus FF [GBW+14].

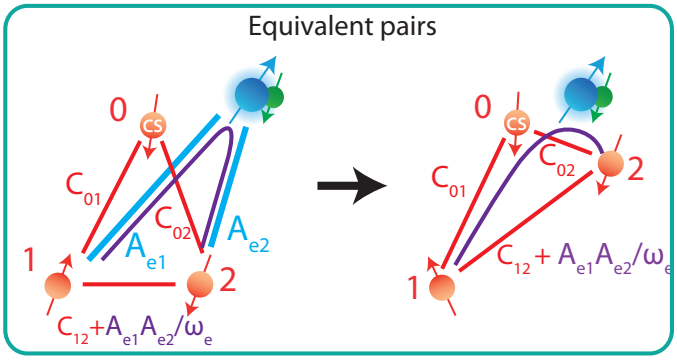


Figure C.2: **Equivalent pair model.** Left: all interactions. Right: dominant interactions only. Spins 1 and 2 are equivalent pairs to allow free flip-flopping. In addition, ΔC_0 must be strong to allow for fast entanglement with the central spin, i.e. one of the two spins of the pair should be close to the donor.

As the EPs have no detuning from the hyperfine interaction, they can be very close to the donor and the measured ^{29}Si. All the nuclear-nuclear dipole couplings can be quite strong in this case with $\Delta A \ll C_{12}+\frac{A_{e1}A_{e2}}{2\omega_e}, \Delta C_0$. In addition, the hyperfine-mediated interaction is very important, as large as 10-100 Hz, and the spins of the EP do not have to be close to one another (weak C_{12}) to be strongly coupled. The bath entanglement in the pseudo-spin picture therefore

becomes:

$$\alpha \approx \frac{2\Delta C_0 \left(C_{12} + \frac{A_{e1}A_{e2}}{2\omega_e}\right)}{\left(C_{12} + \frac{A_{e1}A_{e2}}{2\omega_e}\right)^2 + \Delta C_0^2} \sin^2\left(\frac{t}{2}\sqrt{\left(C_{12} + \frac{A_{e1}A_{e2}}{2\omega_e}\right)^2 + \Delta C_0^2}\right) \tag{C.5}$$

The first comment that can be made is that, for the first time, the amplitude can be quite large as $C_{12} + \frac{A_{e1}A_{e2}}{2\omega_e}$ and ΔC_0 may have similar values. If they are equal, the amplitude is 1. In order to obtain ΔC_0 large enough, the spins of the EP cannot be too close to one another, limiting C_{12}, which is however always boosted by the hyperfine-mediated term. For nuclear-nuclear dipolar couplings varying by about one order of magnitude around 1 Hz, the oscillating frequency is close to that of the measured T_{2n} (Figure 4.10(c)), and so this process is a strong candidate for the measured decoherence. The positions and couplings for the involved spins are illustrated in Figure C.2.

As the central ^{29}Si is slowly taken away from the donor, the measured T_{2n} diminishes. This can be explained for two reasons: first, the number of EPs increases further from the donor, though it saturates at around 5 lattice constants [GBW$^+$14]. Second, when the central spin is far from the donor and closer to the ^{29}Si bulk, the condition $\Delta A \ll C_{12} + \frac{A_{e1}A_{e2}}{2\omega_e}$ can be possible simply because ΔC_0 becomes larger and ΔA can be small due to the large number of ^{29}Si. Eventually, the decoherence is expected to reach the NMR bulk value of 4 ms [LMY$^+$05], at least for low donor concentration.

Bibliography

[AAPS10] G. A. Álvarez, A. Ajoy, X. Peng, and D. Suter. Performance comparison of dynamical decoupling sequences for a qubit in a rapidly fluctuating spin bath. *Physical Review A*, 82(4):042306, October 2010. (Cited on page 71.)

[ABG+05] K. Aydin, I. Bulu, K. Guven, M. Kafesaki, C. M. Soukoulis, and E. Ozbay. Investigation of magnetic resonances for different split-ring resonator parameters and designs. *New Journal of Physics*, 7:168–168, August 2005. (Cited on page 101.)

[AIIY04] E. Abe, K. M. Itoh, J. Isoya, and S. Yamasaki. Electron-spin phase relaxation of phosphorus donors in nuclear-spin- enriched silicon. *Physical Review B*, 70(3):033204, July 2004. (Cited on pages 55 and 107.)

[ATT+10] E. Abe, A. M. Tyryshkin, S. Tojo, J. J. L. Morton, W. M. Witzel, A. Fujimoto, J. W. Ager, E. E. Haller, J. Isoya, S. A. Lyon, M. L. W. Thewalt, and K. M. Itoh. Electron spin coherence of phosphorus donors in silicon: Effect of environmental nuclei. *Physical Review B*, 82(12):121201, September 2010. (Cited on page 55.)

[BCOR09] S. Blanes, F. Casas, J. Oteo, and J. Ros. The Magnus expansion and some of

its applications. *Physics Reports*, 470(5-6):151–238, January 2009. (Cited on page 73.)

[BdGS02] S. D. Bartlett, H. de Guise, and B. C. Sanders. Quantum encodings in spin systems and harmonic oscillators. *Physical Review A*, 65(5):052316, May 2002. (Cited on page 44.)

[BFF+09] P. Becker, H. Friedrich, K. Fujii, W. Giardini, G. Mana, A. Picard, H.-J. Pohl, H. Riemann, and S. Valkiers. The Avogadro constant determination via enriched silicon-28. *Measurement Science and Technology*, 20(9):092002, September 2009. (Cited on page 51.)

[BFN+11] H. Bluhm, S. Foletti, I. Neder, M. Rudner, D. Mahalu, V. Umansky, and A. Yacoby. Dephasing time of GaAs electron-spin qubits coupled to a nuclear bath exceeding 200 μs. *Nature Physics*, 7(2):109–113, February 2011. (Cited on pages 49 and 71.)

[BGPJ+13] N. Bar-Gill, L. M. Pham, A. Jarmola, D. Budker, and R. L. Walsworth. Solid-state electronic spin coherence time approaching one second. *Nature Communications*, 4:1743, April 2013. (Cited on page 17.)

[BGY+11] J. Bylander, S. Gustavsson, F. Yan, F. Yoshihara, K. Harrabi, G. Fitch, D. G. Cory, Y. Nakamura, J.-S. Tsai, and W. D. Oliver. Noise spectroscopy through dynamical decoupling with a superconducting flux qubit. *Nature Physics*, 7(7):565–570, May 2011. (Cited on pages 49, 71 and 72.)

[BKM+12] S. J. Balian, M. B. A. Kunze, M. H. Mohammady, G. W. Morley, W. M. Witzel, C. W. M. Kay, and T. S. Monteiro. Measuring central-spin interaction with a spin bath by pulsed ENDOR: Towards suppression of spin diffusion decoherence. *Physical Review B*, 86(10):104428, September 2012. (Cited on pages 62, 95 and 107.)

[BTS+06] F. R. Bradbury, A. M. Tyryshkin, G. Sabouret, J. Bokor, T. Schenkel, and S. A. Lyon. Stark Tuning of Donor Electron Spins in Silicon. *Physical Review Letters*, 97(17):176404, October 2006. (Cited on pages 18, 117, 123, 124, 126, 127 and 128.)

[BUV+09] M. J. Biercuk, H. Uys, A. P. VanDevender, N. Shiga, W. M. Itano, and J. J. Bollinger. Experimental Uhrig dynamical decoupling using trapped ions. *Physical Review A*, 79(6):062324, June 2009. (Cited on pages 17, 71 and 72.)

[BWMM14] S. J. Balian, G. Wolfowicz, J. J. L. Morton, and T. S. Monteiro. Quantum-bath-driven decoherence of mixed spin systems. *Physical Review B*, 89(4):045403, January 2014. (Cited on pages 109 and 111.)

[Cas63] T. G. Castner. Raman Spin-Lattice Relaxation of Shallow Donors in Silicon. *Physical Review*, 130(1):58–75, April 1963. (Cited on pages 51, 52 and 53.)

[Cas67] T. G. Castner. Orbach Spin-Lattice Relaxation of Shallow Donors in Silicon. *Physical Review*, 155(3):816–825, March 1967. (Cited on page 51.)

[CCL01] A. M. Childs, I. L. Chuang, and D. W. Leung. Realization of quantum process tomography in NMR. *Physical Review A*, 64(1):012314, June 2001. (Cited on page 141.)

[CKHD06] M. J. Calderón, B. Koiller, X. Hu, and S. Das Sarma. Quantum Control of Donor Electrons at the SiSiO2 Interface. *Physical Review Letters*, 96(9):096802, March 2006. (Cited on page 13.)

[CLS+04] J. Chiaverini, D. Leibfried, T. Schaetz, M. D. Barrett, R. B. Blakestad, J. Britton, W. M. Itano, J. D. Jost, E. Knill, C. Langer, R. Ozeri, and D. J. Wineland. Realization of quantum error correction. *Nature*, 432(7017):602–605, December 2004. (Cited on page 80.)

[CMYC14] A. Cooper, E. Magesan, H. N. Yum, and P. Cappellaro. Time-resolved magnetic sensing with electronic spins in diamond. *Nature Communications*, 5:3141, May 2014. (Cited on page 71.)

[CN00] I. L. Chuang and M. A. Nielsen. *Quantum Computation and Quantum Information*. Cambridge University Press, 2000. (Cited on pages 12 and 21.)

[CP54] H. Y. Carr and E. M. Purcell. Effects of Diffusion on Free Precession in Nuclear Magnetic Resonance Experiments. *Physical Review*, 94(3):630–638, May 1954. (Cited on page 74.)

[CPM+98] D. G. Cory, M. D. Price, W. Maas, E. Knill, R. Laflamme, W. H. Zurek, T. F. Havel, and S. S. Somaroo. Experimental Quantum Error Correction. *Physical Review Letters*, 81(10):2152–2155, September 1998. (Cited on page 80.)

[Dav74] E. Davies. A new pulse endor technique. *Physics Letters A*, 47(1):1–2, February 1974. (Cited on page 39.)

[DCJ+07] M. V. G. Dutt, L. Childress, L. Jiang, E. Togan, J. Maze, F. Jelezko, a. S. Zibrov, P. R. Hemmer, and M. D. Lukin. Quantum Register Based on Individual Electronic and Nuclear Spin Qubits in Diamond. *Science*, 316(5829):1312–1316, June 2007. (Cited on page 79.)

[DHB+11] L. Dreher, T. A. Hilker, A. Brandlmaier, S. T. B. Goennenwein, H. Huebl, M. Stutzmann, and M. S. Brandt. Electroelastic Hyperfine Tuning of Phosphorus Donors in Silicon. *Physical Review Letters*, 106(3):037601, January 2011. (Cited on page 116.)

[DiV96] D. P. DiVincenzo. Topics in Quantum Computers. *arXiv:cond-mat*, 9612126, December 1996. (Cited on page 13.)

[dLWR+10] G. de Lange, Z. H. Wang, D. Riste, V. V. Dobrovitski, and R. Hanson. Universal

Dynamical Decoupling of a Single Solid-State Spin from a Spin Bath. *Science*, 330(6000):60–63, October 2010. (Cited on pages 17 and 71.)

[dSD03] R. de Sousa and S. Das Sarma. Theory of nuclear-induced spectral diffusion: Spin decoherence of phosphorus donors in Si and GaAs quantum dots. *Physical Review B*, 68(11):115322, September 2003. (Cited on page 63.)

[DWM04] M. H. Devoret, A. Wallraff, and J. M. Martinis. Superconducting Qubits: A Short Review. *arXiv:cond-mat*, 0411174, November 2004. (Cited on page 13.)

[FCHC06] A. J. Ferguson, V. C. Chan, A. R. Hamilton, and R. G. Clark. Electric-field-induced charge noise in doped silicon: Ionization of phosphorus donors. *Applied Physics Letters*, 88(16):2004–2007, 2006. (Cited on page 128.)

[Feh59a] G. Feher. Electron Spin Resonance Experiments on Donors in Silicon. I. Electronic Structure of Donors by the Electron Nuclear Double Resonance Technique. *Physical Review*, 114(5):1219–1244, June 1959. (Cited on pages 43, 44, 63 and 103.)

[Feh59b] G. Feher. Nuclear Polarization via "Hot" Conduction Electrons. *Physical Review Letters*, 3(3):135–137, August 1959. (Cited on page 54.)

[FG59] G. Feher and E. A. Gere. Electron Spin Resonance Experiments on Donors in Silicon. II. Electron Spin Relaxation Effects. *Physical Review*, 114(5):1245–1256, June 1959. (Cited on pages 43, 50 and 53.)

[Fri05] M. Friesen. Theory of the Stark Effect for P Donors in Si. *Physical Review Letters*, 94(18):186403, May 2005. (Cited on pages 117 and 118.)

[FYP+54] R. C. Fletcher, W. A. Yager, G. L. Pearson, a. N. Holden, W. T. Read, and F. R. Merritt. Spin Resonance of Donors in Silicon. *Physical Review*, 94(5):1392–1393, June 1954. (Cited on page 43.)

[FYPM54] R. C. Fletcher, W. A. Yager, G. L. Pearson, and F. R. Merritt. Hyperfine Splitting in Spin Resonance of Group V Donors in Silicon. *Physical Review*, 95(3):844–845, August 1954. (Cited on page 43.)

[GB58] J. P. Gordon and K. D. Bowers. Microwave Spin Echoes from Donor Electrons in Silicon. *Physical Review Letters*, 1(10):368–370, November 1958. (Cited on pages 15, 16, 49, 54, 55 and 70.)

[GBM02] P. Gay-Balmaz and O. J. F. Martin. Electromagnetic resonances in individual and coupled split-ring resonators. *Journal of Applied Physics*, 92(5):2929–2936, 2002. (Cited on page 101.)

[GBW+14] R. Guichard, S. J. Balian, G. Wolfowicz, P. A. Mortemousque, and T. S. Monteiro. Decoherence of proximate nuclear spin qubits in natural silicon. *arXiv:quant-ph*, 1409.8655, September 2014. (Cited on pages 163 and 164.)

[Got00] D. Gottesman. An Introduction to Quantum Error Correction. *arXiv:quant-ph*, page 0004072, April 2000. (Cited on page 80.)

[GWR+10] R. E. George, W. Witzel, H. Riemann, N. V. Abrosimov, N. Nötzel, M. L. W. Thewalt, and J. J. L. Morton. Electron Spin Coherence and Electron Nuclear Double Resonance of Bi Donors in Natural Si. *Physical Review Letters*, 105(6):067601, August 2010. (Cited on pages 17, 55 and 95.)

[Hah50] E. L. Hahn. Spin Echoes. *Physical Review*, 80(4):580–594, November 1950. (Cited on pages 17 and 36.)

[HHF+05] C. D. Hill, L. C. L. Hollenberg, A. G. Fowler, C. J. Wellard, A. D. Greentree, and H.-S. Goan. Global control and fast solid-state donor electron spin quantum computing. *Physical Review B*, 72(4):045350, July 2005. (Cited on page 117.)

[HIV08] H. Hayashi, K. M. Itoh, and L. S. Vlasenko. Nuclear magnetic resonance

linewidth and spin diffusion in 29Si isotopically controlled silicon. *Physical Review B*, 78(15):153201, October 2008. (Cited on page 162.)

[HM69] E. B. Hale and R. L. Mieher. Shallow Donor Electrons in Silicon. I. Hyperfine Interactions from ENDOR Measurements. *Physical Review*, 184(3):739–750, August 1969. (Cited on pages 62 and 88.)

[HS05] N. Hatano and M. Suzuki. Quantum Annealing and Other Optimization Methods. In A. Das and B. K. Chakrabarti, editors, *Quantum Annealing and Other Optimization ...*, volume 679 of *Lecture Notes in Physics*, page 22. Springer Berlin Heidelberg, Berlin, Heidelberg, 2005. (Cited on pages 73 and 77.)

[HW68] U. Haeberlen and J. S. Waugh. Coherent Averaging Effects in Magnetic Resonance. *Physical Review*, 175(2):453–467, November 1968. (Cited on pages 17 and 89.)

[IKU+03] K. M. Itoh, J. Kato, M. Uemura, A. K. Kaliteevskii, O. N. Godisov, G. G. Devyatych, A. D. Bulanov, A. V. Gusev, I. D. Kovalev, P. G. Sennikov, H.-J. Pohl, N. V. Abrosimov, and H. Riemann. High purity isotopically enriched 29Si and 30Si single crystals: isotope separation, purification, and growth. *Japanese Journal of Applied Physics*, 42(Part 1, No. 10):6248–6251, October 2003. (Cited on page 51.)

[Jon11] J. A. Jones. Quantum computing with NMR. *Progress in Nuclear Magnetic Resonance Spectroscopy*, 59(2):91–120, August 2011. (Cited on page 28.)

[KA62] J. R. Klauder and P. W. Anderson. Spectral Diffusion Decay in Spin Resonance Experiments. *Physical Review*, 125(3):912–932, February 1962. (Cited on page 55.)

[KAG+11] S. Kotler, N. Akerman, Y. Glickman, A. Keselman, and R. Ozeri. Single-ion

quantum lock-in amplifier. *Nature*, 473(7345):61–65, May 2011. (Cited on page 71.)

[Kan98] B. E. Kane. A silicon-based nuclear spin quantum computer. *Nature*, 393(6681):133–137, May 1998. (Cited on pages 13, 14 and 15.)

[KI92] V. V. Kurshev and T. Ichikawa. Effect of spin flip-flop on electron-spin-echo decay due to instantaneous diffusion. *Journal of Magnetic Resonance (1969)*, 96(3):563–573, February 1992. (Cited on page 56.)

[Kie01] D. Kielpinski. A Decoherence-Free Quantum Memory Using Trapped Ions. *Science*, 291(5506):1013–1015, February 2001. (Cited on page 93.)

[KLA+02] E. Knill, R. Laflamme, A. Ashikhmin, H. Barnum, L. Viola, and W. H. Zurek. Introduction to Quantum Error Correction. *arXiv:quant-ph*, 0207170, July 2002. (Cited on page 80.)

[Koh57] W. Kohn. Shallow Impurity States in Silicon and Germanium. In *Solid State Physics - Advances in Research and Applications*, volume 5, pages 257–320. 1957. (Cited on page 63.)

[KW59] W. Kaiser and G. H. Wheatley. Hot Electrons and Carrier Multiplication in Silicon at Low Temperature. *Physical Review Letters*, 3(7):334–336, October 1959. (Cited on page 126.)

[KYG+07] J. Koch, T. M. Yu, J. Gambetta, A. A. Houck, D. I. Schuster, J. Majer, A. Blais, M. H. Devoret, S. M. Girvin, and R. J. Schoelkopf. Charge-insensitive qubit design derived from the Cooper pair box. *Physical Review A*, 76(4):042319, October 2007. (Cited on pages 18 and 93.)

[LAS06] J. J. Longdell, A. L. Alexander, and M. J. Sellars. Characterization of the hyperfine interaction in europium-doped yttrium orthosilicate and europium chloride

hexahydrate. *Physical Review B*, 74(19):195101, November 2006. (Cited on page 93.)

[Lev09] M. H. Levitt. *Spin dynamics. Basics of nuclear magnetic resonance*. 2009. (Cited on page 21.)

[LJL+10] T. D. Ladd, F. Jelezko, R. Laflamme, Y. Nakamura, C. Monroe, and J. L. O'Brien. Quantum computers. *Nature*, 464(7285):45–53, March 2010. (Cited on page 13.)

[LMM+15] A. Laucht, J. T. Muhonen, F. A. Mohiyaddin, R. Kalra, J. P. Dehollain, S. Freer, F. E. Hudson, M. Veldhorst, R. Rahman, G. Klimeck, K. M. Itoh, D. N. Jamieson, J. C. McCallum, A. S. Dzurak, and A. Morello. Electrically controlling single-spin qubits in a continuous microwave field. *Science Advances*, 1(3):e1500022, April 2015. (Cited on page 150.)

[LMY+05] T. D. Ladd, D. Maryenko, Y. Yamamoto, E. Abe, and K. M. Itoh. Coherence time of decoupled nuclear spins in silicon. *Physical Review B*, 71(1):014401, January 2005. (Cited on pages 71, 86, 90 and 164.)

[LOJ+05] C. Langer, R. Ozeri, J. Jost, J. Chiaverini, B. DeMarco, A. Ben-Kish, R. Blakestad, J. Britton, D. Hume, W. Itano, D. Leibfried, R. Reichle, T. Rosenband, T. Schaetz, P. Schmidt, and D. Wineland. Long-Lived Qubit Memory Using Atomic Ions. *Physical Review Letters*, 95(6):060502, August 2005. (Cited on pages 13 and 93.)

[LSL+14] C. C. Lo, S. Simmons, R. Lo Nardo, C. D. Weis, A. M. Tyryshkin, J. Meijer, D. Rogalla, S. A. Lyon, J. Bokor, T. Schenkel, and J. J. L. Morton. Stark shift and field ionization of arsenic donors in 28Si- silicon-on-insulator structures. *Applied Physics Letters*, 104(19):193502, May 2014. (Cited on pages 18, 59, 117 and 127.)

[LUR+15] C. C. Lo, M. Urdampilleta, P. Ross, M. F. Gonzalez-Zalba, J. Mansir, S. A. Lyon, M. L. W. Thewalt, and J. J. L. Morton. Hybrid optical-electrical detection of donor electron spins with bound excitons in silicon. *Nature Materials*, 14(5):490–494, March 2015. (Cited on page 54.)

[MBSL12] D. L. McAuslan, J. G. Bartholomew, M. J. Sellars, and J. J. Longdell. Reducing decoherence in optical and spin transitions in rare-earth-metal-ion-doped materials. *Physical Review A*, 85(3):032339, March 2012. (Cited on page 93.)

[MDL+14] J. T. Muhonen, J. P. Dehollain, A. Laucht, F. E. Hudson, T. Sekiguchi, K. M. Itoh, D. N. Jamieson, J. C. McCallum, A. S. Dzurak, and A. Morello. Storing quantum information for 30 seconds in a nanoelectronic device. *Nature Nanotechnology*, 9(12):986–991, October 2014. (Cited on pages 71 and 128.)

[MG58] S. Meiboom and D. Gill. Modified Spin-Echo Method for Measuring Nuclear Relaxation Times. *Review of Scientific Instruments*, 29(8):688, 1958. (Cited on page 74.)

[Mim65] W. B. Mims. Pulsed Endor Experiments. *Proceedings of the Royal Society A: Mathematical, Physical and Engineering Sciences*, 283(1395):452–457, January 1965. (Cited on page 38.)

[ML11] J. J. Morton and B. W. Lovett. Hybrid Solid-State Qubits: The Powerful Role of Electron Spins. *Annual Review of Condensed Matter Physics*, 2(1):189–212, March 2011. (Cited on page 16.)

[MLH+12] G. W. Morley, P. Lueders, M. Hamed Mohammady, S. J. Balian, G. Aeppli, C. W. M. Kay, W. M. Witzel, G. Jeschke, and T. S. Monteiro. Quantum control of hybrid nuclearelectronic qubits. *Nature Materials*, 12(2):103–107, December 2012. (Cited on page 101.)

[MMEL11] J. J. L. Morton, D. R. McCamey, M. A. Eriksson, and S. A. Lyon. Embracing the quantum limit in silicon computing. *Nature*, 479(7373):345–353, November 2011. (Cited on page 15.)

[MMNM12] M. H. Mohammady, G. W. Morley, A. Nazir, and T. S. Monteiro. Analysis of quantum coherence in bismuth-doped silicon: A system of strongly coupled spin qubits. *Physical Review B*, 85(9):094404, March 2012. (Cited on pages 46, 64, 95 and 98.)

[MPZ+10] A. Morello, J. J. Pla, F. A. Zwanenburg, K. W. Chan, K. Y. Tan, H. Huebl, M. Möttönen, C. D. Nugroho, C. Yang, J. A. van Donkelaar, A. D. C. Alves, D. N. Jamieson, C. C. Escott, L. C. L. Hollenberg, R. G. Clark, and A. S. Dzurak. Single-shot readout of an electron spin in silicon. *Nature*, 467(7316):687–691, October 2010. (Cited on page 16.)

[MSZ00] F. Momo, A. Sotgiu, and R. Zonta. On the design of a split ring resonator for ESR spectroscopy between 1 and 4 GHz. *Journal of Physics E: Scientific Instruments*, 16(1):43–46, January 2000. (Cited on page 101.)

[MTB+08] J. J. L. Morton, A. M. Tyryshkin, R. M. Brown, S. Shankar, B. W. Lovett, A. Ardavan, T. Schenkel, E. E. Haller, J. W. Ager, and S. A. Lyon. Solid state quantum memory using the 31P nuclear spin. *Nature*, 455(7216):1085–1088, October 2008. (Cited on pages 17, 40, 41, 50, 59, 86 and 141.)

[MWS+10] G. W. Morley, M. Warner, A. M. Stoneham, P. T. Greenland, J. van Tol, C. W. M. Kay, and G. Aeppli. The initialization and manipulation of quantum information stored in silicon by bismuth dopants. *Nature Materials*, 9(9):725–729, September 2010. (Cited on pages 17 and 53.)

[NDH+11] B. Naydenov, F. Dolde, L. T. Hall, C. Shin, H. Fedder, L. C. L. Hollenberg, F. Jelezko, and J. Wrachtrup. Dynamical decoupling of a single-electron spin at

room temperature. *Physical Review B*, 83(8):081201, February 2011. (Cited on page 74.)

[OPG+04] J. L. O'Brien, G. J. Pryde, A. Gilchrist, D. F. V. James, N. K. Langford, T. C. Ralph, and A. G. White. Quantum Process Tomography of a Controlled-NOT Gate. *Physical Review Letters*, 93(8):080502, August 2004. (Cited on pages 139 and 142.)

[PMBV08] S. Pirandola, S. Mancini, S. L. Braunstein, and D. Vitali. Minimal qudit code for a qubit in the phase-damping channel. *Physical Review A*, 77(3):032309, March 2008. (Cited on page 44.)

[PS00] N. V. Prokof'ev and P. C. E. Stamp. Theory of the spin bath. *Reports on Progress in Physics*, 63(4):669–726, April 2000. (Cited on page 61.)

[PTD+12] J. J. Pla, K. Y. Tan, J. P. Dehollain, W. H. Lim, J. J. L. Morton, D. N. Jamieson, A. S. Dzurak, and A. Morello. A single-atom electron spin qubit in silicon. *Nature*, 489(7417):541–545, September 2012. (Cited on pages 16, 117 and 151.)

[PTD+13] J. J. Pla, K. Y. Tan, J. P. Dehollain, W. H. Lim, J. J. L. Morton, F. A. Zwanenburg, D. N. Jamieson, A. S. Dzurak, and A. Morello. High-fidelity readout and control of a nuclear spin qubit in silicon. *Nature*, 496(7445):334–8, April 2013. (Cited on pages 16, 82, 117 and 151.)

[PWU+14] G. Pica, G. Wolfowicz, M. Urdampilleta, M. L. W. Thewalt, H. Riemann, N. V. Abrosimov, P. Becker, H.-j. Pohl, J. J. L. Morton, R. N. Bhatt, S. A. Lyon, and B. W. Lovett. Hyperfine Stark effect of shallow donors in silicon. *Physical Review B*, 90(19):195204, November 2014. (Cited on pages 117, 118, 119 and 129.)

[RAN06] H. Riemann, N. Abrosimov, and N. Noetzel. Doping of silicon crystals with Bi and other volatile elements by the pedestal growth technique. *ECS Transactions*, 84(10126728):10126728, 2006. (Cited on page 96.)

[RDN+12] M. D. Reed, L. DiCarlo, S. E. Nigg, L. Sun, L. Frunzio, S. M. Girvin, and R. J. Schoelkopf. Realization of three-qubit quantum error correction with superconducting circuits. *Nature*, 482(7385):382–385, February 2012. (Cited on page 80.)

[RPB+09] R. Rahman, S. H. Park, T. B. Boykin, G. Klimeck, S. Rogge, and L. C. L. Hollenberg. Gate-induced g-factor control and dimensional transition for donors in multivalley semiconductors. *Physical Review B*, 80(15):155301, October 2009. (Cited on pages 117, 118, 120, 128 and 130.)

[RWB+07] R. Rahman, C. J. Wellard, F. R. Bradbury, M. Prada, J. H. Cole, G. Klimeck, and L. C. L. Hollenberg. High Precision Quantum Control of Single Donor Spins in Silicon. *Physical Review Letters*, 99(3):036403, July 2007. (Cited on page 117.)

[SBR+11] S. Simmons, R. M. Brown, H. Riemann, N. V. Abrosimov, P. Becker, H.-J. Pohl, M. L. W. Thewalt, K. M. Itoh, and J. J. L. Morton. Entanglement in a solid-state spin ensemble. *Nature*, 470(7332):69–72, February 2011. (Cited on page 16.)

[SDK03] A. J. Skinner, M. E. Davenport, and B. E. Kane. Hydrogenic Spin Quantum Computing in Silicon: A Digital Approach. *Physical Review Letters*, 90(8):087901, February 2003. (Cited on page 13.)

[SDR81] K. Salikhov, S. Dzuba, and A. Raitsimring. The theory of electron spin-echo signal decay resulting from dipole-dipole interactions between paramagnetic centers in solids. *Journal of Magnetic Resonance (1969)*, 42(2):255–276, February 1981. (Cited on page 56.)

[Sho95] P. W. Shor. Scheme for reducing decoherence in quantum computer memory. *Physical Review A*, 52(4):R2493–R2496, October 1995. (Cited on page 80.)

[SHO+06] D. Stick, W. K. Hensinger, S. Olmschenk, M. J. Madsen, K. Schwab, and C. Monroe. Ion trap in a semiconductor chip. *Nature Physics*, 2(1):36–39, January 2006. (Cited on page 13.)

[Shr83] K. N. Shrivastava. Theory of SpinLattice Relaxation. *physica status solidi (b)*, 117(2):437–458, June 1983. (Cited on page 51.)

[SJ01] A. Schweiger and G. Jeschke. *Principles of Pulse Electron Paramagnetic Resonance*. Oxford University Press, 2001. (Cited on pages 21, 33 and 56.)

[Soh61] J.-C. Sohm. Ionisation par choc des impuretes dans le silicium. *Journal of Physics and Chemistry of Solids*, 18(2-3):181–192, February 1961. (Cited on page 126.)

[SRCK04] G. D. J. Smit, S. Rogge, J. Caro, and T. M. Klapwijk. Stark effect in shallow impurities in Si. *Physical Review B*, 70(3):035206, July 2004. (Cited on pages 118 and 119.)

[SSP+13] T. Staudacher, F. Shi, S. Pezzagna, J. Meijer, J. Du, C. A. Meriles, F. Reinhard, and J. Wrachtrup. Nuclear Magnetic Resonance Spectroscopy on a (5-Nanometer)3 Sample Volume. *Science*, 339(6119):561–563, February 2013. (Cited on page 71.)

[SSS+10] T. Sekiguchi, M. Steger, K. Saeedi, M. L. W. Thewalt, H. Riemann, N. V. Abrosimov, and N. Nötzel. Hyperfine Structure and Nuclear Hyperpolarization Observed in the Bound Exciton Luminescence of Bi Donors in Natural Si. *Physical Review Letters*, 104(13):137402, April 2010. (Cited on pages 54 and 83.)

[SSS+13] K. Saeedi, S. Simmons, J. Z. Salvail, P. Dluhy, H. Riemann, N. V. Abrosimov, P. Becker, H.-J. Pohl, J. J. L. Morton, and M. L. W. Thewalt. Room-Temperature Quantum Bit Storage Exceeding 39 Minutes Using Ionized Donors in Silicon-28. *Science*, 342(6160):830–833, November 2013. (Cited on pages 17, 59 and 151.)

[SST+12] M. Steger, K. Saeedi, M. L. W. Thewalt, J. J. L. Morton, H. Riemann, N. V. Abrosimov, P. Becker, and H.-J. Pohl. Quantum Information Storage for over 180 s Using Donor Spins in a 28Si "Semiconductor Vacuum". *Science*, 336(6086):1280–1283, June 2012. (Cited on pages 17, 59, 83 and 86.)

[SSY+11] M. Steger, T. Sekiguchi, A. Yang, K. Saeedi, M. E. Hayden, M. L. W. Thewalt, K. M. Itoh, H. Riemann, N. V. Abrosimov, P. Becker, and H. J. Pohl. Optically-detected NMR of optically-hyperpolarized 31P neutral donors in 28Si. *Journal of Applied Physics*, 109(10):102411, 2011. (Cited on pages 54 and 83.)

[Ste96a] A. M. Steane. Error Correcting Codes in Quantum Theory. *Physical Review Letters*, 77(5):793–797, July 1996. (Cited on page 80.)

[Ste96b] A. Steane. Multiple-Particle Interference and Quantum Error Correction. *Proceedings of the Royal Society A: Mathematical, Physical and Engineering Sciences*, 452(1954):2551–2577, November 1996. (Cited on page 80.)

[STL14] A. J. Sigillito, A. M. Tyryshkin, and S. A. Lyon. Anisotropic Stark effect and electric-field noise suppression for phosphorus donor qubits in silicon. *arXiv:cond-mat*, 1409.3295, 2014. (Cited on pages 120 and 128.)

[Sto05] N. J. Stone. Table of nuclear magnetic dipole and electric quadrupole moments. *Atomic Data and Nuclear Data Tables*, 90:75–176, 2005. (Cited on page 44.)

[SYS07] S. K. Saikin, W. Yao, and L. J. Sham. Single-electron spin decoherence by nuclear spin bath: Linked-cluster expansion approach. *Physical Review B*, 75(12):125314, March 2007. (Cited on pages 65 and 78.)

[TBB+14] S. Thiele, F. Balestro, R. Ballou, S. Klyatskaya, M. Ruben, and W. Wernsdorfer. Electrically driven nuclear spin resonance in single-molecule magnets. *Science*, 344(6188):1135–1138, June 2014. (Cited on page 144.)

[TCvdS+14] T. H. Taminiau, J. Cramer, T. van der Sar, V. V. Dobrovitski, and R. Hanson. Universal control and error correction in multi-qubit spin registers in diamond. *Nature Nanotechnology*, 9(3):171–6, March 2014. (Cited on pages 18, 59, 79, 80 and 83.)

[TG97] A. Tannús and M. Garwood. Adiabatic pulses. *NMR in Biomedicine*, 10:423–434, 1997. (Cited on pages 85 and 143.)

[TLAR03] A. M. Tyryshkin, S. A. Lyon, A. V. Astashkin, and A. M. Raitsimring. Electron spin relaxation times of phosphorus donors in silicon. *Physical Review B*, 68(19):193207, November 2003. (Cited on pages 50, 56 and 57.)

[TMAL06] A. M. Tyryshkin, J. J. L. Morton, A. Ardavan, and S. A. Lyon. Davies electron-nuclear double resonance revisited: Enhanced sensitivity and nuclear spin relaxation. *Journal of Chemical Physics*, 124(23):234508, June 2006. (Cited on page 64.)

[TTM+11] A. M. Tyryshkin, S. Tojo, J. J. L. Morton, H. Riemann, N. V. Abrosimov, P. Becker, H.-J. Pohl, T. Schenkel, M. L. W. Thewalt, K. M. Itoh, and S. a. Lyon. Electron spin coherence exceeding seconds in high-purity silicon. *Nature Materials*, 11(2):143–147, December 2011. (Cited on pages 17, 56, 57, 79 and 105.)

[Uhr07] G. S. Uhrig. Keeping a Quantum Bit Alive by Optimized π-Pulse Sequences. *Physical Review Letters*, 98(10):100504, March 2007. (Cited on pages 70 and 74.)

[vD84] S. Žurauskas and A. Dargys. Field Ionization of Phosphorus Atoms in Silicon. *physica status solidi (b)*, 121(1):385–391, January 1984. (Cited on page 126.)

[Vio02] D. Vion. Manipulating the Quantum State of an Electrical Circuit. *Science*, 296(5569):886–889, May 2002. (Cited on pages 13 and 93.)

[VKL99] L. Viola, E. Knill, and S. Lloyd. Dynamical Decoupling of Open Quantum Systems. *Physical Review Letters*, 82(12):2417–2421, March 1999. (Cited on page 70.)

[VL98] L. Viola and S. Lloyd. Dynamical suppression of decoherence in two-state quantum systems. *Physical Review A*, 58(4):2733–2744, October 1998. (Cited on page 70.)

[VYW+00] R. Vrijen, E. Yablonovitch, K. Wang, H. W. Jiang, A. Balandin, V. Roychowdhury, T. Mor, and D. DiVincenzo. Electron-spin-resonance transistors for quantum computing in silicon-germanium heterostructures. *Physical Review A*, 62(1):012306, June 2000. (Cited on page 13.)

[WAB+09] J. H. Wesenberg, A. Ardavan, G. A. D. Briggs, J. J. L. Morton, R. J. Schoelkopf, D. I. Schuster, and K. Mø lmer. Quantum Computing with an Electron Spin Ensemble. *Physical Review Letters*, 103(7):070502, August 2009. (Cited on page 16.)

[WCCD12] W. M. Witzel, M. S. Carroll, u. Cywiski, and S. Das Sarma. Quantum decoherence of the central spin in a sparse system of dipolar coupled spins. *Physical Review B*, 86(3):035452, July 2012. (Cited on page 62.)

[WCM+10] W. M. Witzel, M. S. Carroll, A. Morello, u. Cywiski, and S. Das Sarma. Electron Spin Decoherence in Isotope-Enriched Silicon. *Physical Review Letters*, 105(18):187602, October 2010. (Cited on pages 58 and 65.)

[WD06] W. M. Witzel and S. Das Sarma. Quantum theory for electron spin decoherence induced by nuclear spin dynamics in semiconductor quantum computer architectures: Spectral diffusion of localized electron spins in the nuclear solid-state environment. *Physical Review B*, 74(3):035322, July 2006. (Cited on pages 62, 65, 69 and 107.)

[WF61] D. K. Wilson and G. Feher. Electron Spin Resonance Experiments on Donors in Silicon. III. Investigation of Excited States by the Application of Uniaxial Stress

and Their Importance in Relaxation Processes. *Physical Review*, 124(4):1068–1083, November 1961. (Cited on pages 43, 51, 116, 120 and 121.)

[WFL10] J. R. West, B. H. Fong, and D. a. Lidar. Near-Optimal Dynamical Decoupling of a Qubit. *Physical Review Letters*, 104(13):130501, April 2010. (Cited on page 70.)

[WGG+13] H. Wu, E. M. Gauger, R. E. George, M. Möttönen, H. Riemann, N. V. Abrosimov, P. Becker, H.-J. Pohl, K. M. Itoh, M. L. W. Thewalt, and J. J. L. Morton. Geometric phase gates with adiabatic control in electron spin resonance. *Physical Review A*, 87(3):032326, March 2013. (Cited on page 143.)

[WGW+10] H. Wu, R. E. George, J. H. Wesenberg, K. Mø lmer, D. I. Schuster, R. J. Schoelkopf, K. M. Itoh, A. Ardavan, J. J. L. Morton, and G. A. D. Briggs. Storage of Multiple Coherent Microwave Excitations in an Electron Spin Ensemble. *Physical Review Letters*, 105(14):140503, September 2010. (Cited on page 16.)

[WHH68] J. S. Waugh, L. M. Huber, and U. Haeberlen. Approach to High-Resolution nmr in Solids. *Physical Review Letters*, 20(5):180–182, January 1968. (Cited on page 89.)

[Wim94] S. Wimperis. Broadband, narrowband, and passband composite pulses for use in advanced NMR experiments. *Journal of Magnetic Resonance, Series A*, 109(2):221–231, August 1994. (Cited on pages 85 and 143.)

[WST+12] G. Wolfowicz, S. Simmons, A. M. Tyryshkin, R. E. George, H. Riemann, N. V. Abrosimov, P. Becker, H.-J. Pohl, S. A. Lyon, M. L. W. Thewalt, and J. J. L. Morton. Decoherence mechanisms of 209Bi donor electron spins in isotopically pure 28Si. *Physical Review B*, 86(24):245301, December 2012. (Cited on pages 49, 52, 53, 56, 57, 95 and 96.)

[WTG+13] G. Wolfowicz, A. M. Tyryshkin, R. E. George, H. Riemann, N. V. Abrosimov, P. Becker, H.-j. Pohl, M. L. W. Thewalt, S. A. Lyon, and J. J. L. Morton. Atomic

clock transitions in silicon-based spin qubits. *Nature Nanotechnology*, 8(8):561–4, August 2013. (Cited on pages 44 and 103.)

[WWZ+14] G. Waldherr, Y. Wang, S. Zaiser, M. Jamali, T. Schulte-Herbrüggen, H. Abe, T. Ohshima, J. Isoya, J. F. Du, P. Neumann, and J. Wrachtrup. Quantum error correction in a solid-state hybrid spin register. *Nature*, 506(7487):204–7, February 2014. (Cited on pages 18, 59, 79 and 80.)

[YBS+15] K. Yuimaru, A. Bienfait, M. Stern, D. Vion, D. Esteve, P. Bertet, J. J. Pla, C. C. Lo, J. J. L. Morton, C. D. Weis, T. Schenkel, and M. Thewalt. Electron Spin Resonance Spectroscopy of Bismuth donors in Silicon using a Parametric Amplifier. In *APS March Meeting Abstracts*, 2015. (Cited on page 151.)

[YL08] W. Yang and R.-B. Liu. Universality of Uhrig Dynamical Decoupling for Suppressing Qubit Pure Dephasing and Relaxation. *Physical Review Letters*, 101(18):180403, October 2008. (Cited on page 75.)

[YL09a] W. Yang and R.-B. Liu. Quantum many-body theory of qubit decoherence in a finite-size spin bath. II. Ensemble dynamics. *Physical Review B*, 79(11):115320, March 2009. (Cited on page 69.)

[YL09b] W. Yang and R.-B. Liu. Quantum many-body theory of qubit decoherence in a finite-size spin bath. II. Ensemble dynamics. *Physical Review B*, 79(11):115320, March 2009. (Cited on page 69.)

[YLS06] W. Yao, R.-B. Liu, and L. J. Sham. Theory of electron spin decoherence by interacting nuclear spins in a quantum dot. *Physical Review B*, 74(19):195301, November 2006. (Cited on pages 65 and 67.)

[YN11] J. Q. You and F. Nori. Atomic physics and quantum optics using superconducting circuits. *Nature*, 474(7353):589–597, June 2011. (Cited on page 13.)

[YSK+06] A. Yang, M. Steger, D. Karaiskaj, M. L. W. Thewalt, M. Cardona, K. M. Itoh, H. Riemann, N. V. Abrosimov, M. F. Churbanov, A. V. Gusev, A. D. Bulanov, A. K. Kaliteevskii, O. N. Godisov, P. Becker, H.-J. Pohl, J. W. Ager, and E. E. Haller. Optical Detection and Ionization of Donors in Specific Electronic and Nuclear Spin States. *Physical Review Letters*, 97(22):227401, November 2006. (Cited on pages 54 and 59.)

[ZHH+11] N. Zhao, J.-L. Hu, S.-W. Ho, J. T. K. Wan, and R. B. Liu. Atomic-scale magnetometry of distant nuclear spin clusters via nitrogen-vacancy spin in diamond. *Nature Nanotechnology*, 6(4):242–246, April 2011. (Cited on page 71.)

[Zur03] W. H. Zurek. Decoherence, einselection, and the quantum origins of the classical. *Reviews of Modern Physics*, 75(3):715–775, May 2003. (Cited on page 61.)

[ZWL11] N. Zhao, Z.-Y. Wang, and R.-B. Liu. Anomalous Decoherence Effect in a Quantum Bath. *Physical Review Letters*, 106(21):217205, May 2011. (Cited on pages 67 and 74.)

[ZWL+14] N. Zhao, G. Wolfowicz, S.-s. Li, J. J. L. Morton, and B. Liu. Uncovering many-body correlations in nanoscale nuclear spin baths by central spin decoherence. *Nature Communications*, 5:4822, January 2014. (Cited on pages 76 and 78.)